

# Design and Evaluation of Robust Control Methods for Robotic Transfemoral Prostheses

Nitish Thatte

March 17, 2019

The Robotics Institute  
Carnegie Mellon University  
Pittsburgh, PA 15213

*Thesis Committee:*

Hartmut Geyer (Chair)

Chris Atkeson

Aaron Johnson

Steven Collins, Stanford University

Elliott Rouse, University of Michigan

*Submitted in partial fulfillment of the requirements  
for the degree of Doctor of Philosophy*

Copyright ©2019 Nitish Thatte.



# *Contents*

<b>1</b>	<i>Introduction</i>	<b>17</b>	
	<b>1.1</b>	<i>Motivation</i>	<b>17</b>
<b>2</b>	<i>Transfemoral Prosthesis Development</i>	<b>21</b>	
	<b>2.1</b>	<i>Mechanical Design</i>	<b>21</b>
	<b>2.2</b>	<i>Series Elastic Actuator Control</i>	<b>27</b>
	<b>2.3</b>	<i>Performance Evaluation</i>	<b>27</b>
<b>3</b>	<i>Neuromuscular Model</i>	<b>29</b>	
	<b>3.1</b>	<i>Mechanical Model</i>	<b>29</b>
	<b>3.2</b>	<i>Hill Muscle Models</i>	<b>31</b>
	<b>3.3</b>	<i>Stance Reflexes</i>	<b>33</b>
	<b>3.4</b>	<i>Swing Leg Control</i>	<b>35</b>
	<b>3.5</b>	<i>Control for Simulation Experiments</i>	<b>37</b>
	<b>3.6</b>	<i>Control for Prosthesis Experiments</i>	<b>37</b>
<b>4</b>	<i>Simultated Comparison of Neuromuscular and Impedance Controllers</i>	<b>41</b>	
	<b>4.1</b>	<i>Methods</i>	<b>41</b>
	<b>4.2</b>	<i>Results</i>	<b>44</b>
<b>5</b>	<i>Preference Based Optimization</i>	<b>47</b>	
	<b>5.1</b>	<i>Bayesian Approach Preliminaries</i>	<b>48</b>

5.2	<i>Bayesian Approach Methods</i>	49
5.3	<i>Bayesian Approach Results</i>	53
5.4	<i>Bayesian Approach Discussion</i>	55
5.5	<i>Bandit Approach - Introduction</i>	56
5.6	<i>Bandit Approach Methods</i>	58
5.7	<i>Bandit Approach Results</i>	62
5.8	<i>Bandit Approach Discussion</i>	64
6	<i>Experimental Comparison of Neuromuscular and Impedance Controllers</i>	69
6.1	<i>Introduction</i>	69
6.2	<i>Methods</i>	69
6.3	<i>Results</i>	74
6.4	<i>Discussion</i>	78
7	<i>Reactive Swing Control for Trip Avoidance</i>	81
7.1	<i>Classification Approach Introduction</i>	81
7.2	<i>Classification Approach Methods</i>	83
7.3	<i>Classification Approach Results</i>	87
7.4	<i>Classification Approach Discussion</i>	89
7.5	<i>Planning Approach Introduction</i>	91
7.6	<i>Planning Approach Methods</i>	92
7.7	<i>Planning Approach Results</i>	101
7.8	<i>Planning Approach Discussion</i>	103
8	<i>Robust and Adaptive Stance Control via Extended Kalman Filter-based Phase Estimation</i>	107
8.1	<i>Introduction</i>	107
8.2	<i>Methods</i>	108
8.3	<i>Results</i>	114
8.4	<i>Discussion</i>	117

9     *Future Work*        121

*Bibliography*        123



## *List of Figures*

- 1.1 Examples of microprocessor-controlled mechanically-passive knee prostheses (a,b) and a energy storage and return ankle-foot prosthesis (c). 17
- 1.2 Vanderbilt University's Robotic Transfemoral Prostheses. Images courtesy of Michael Goldfarb. 18
- 1.3 Biom Robotic Ankle Prosthesis. Photo by Steve Jurvetson, CC BY 2.0, Link (cropped from original). 19
- 2.1 Render of proposed powered knee and ankle prosthesis design. The prosthesis includes series elastic actuators to enable accurate torque control and a unidirectional parallel ankle spring to offset the required angle torque. 21
- 2.2 Knee motor torque required for running 22
- 2.3 Internal and external design of the knee joint. 23
- 2.4 Impact simulation we used to determine appropriate series spring stiffness. 23
- 2.5 Ankle torque vs angle curve during steady, level-ground walking (blue) (Winter [2009] scaled to 80 kg person). A unidirectional parallel spring can provide a portion of this torque (green) and reduces the required actuator torque (purple) to lie under repeated torque limit of the Harmonic Drive Gear set (orange). 25
- 2.6 Ankle motor torque required to take the trip recovery action observed by Pijnappels et al. [2005] (blue, trajectory obtained by scaling walking data from Winter [2009] to a peak torque of 202 N · m, 75% gear efficiency assumed). Using a parallel spring allows the motor to produce the required torque (green) while remaining within its torque limit (purple). 25
- 2.7 Ankle motor torque required to reproduce the running trajectory recorded by Novacheck [1998] assuming a parallel spring stiffness of 267 N·m/rad and a gear efficiency of 75%. 26
- 2.8 Internal and external design of the ankle joint. 26
- 2.9 Impact simulation we used to determine appropriate series spring stiffness. 27

- 2.10 Experimentally obtained bode plots of knee and ankle actuator torque.  
Knee is phase limited at 24 Hz while the ankle is gain limited at 7 Hz. 27
- 2.11 Zero torque tracking of knee and ankle joints. The prosthesis was fixed to a rigid mount and commanded to maintain zero net joint torque while the knee and ankle joints were manually oscillated (blue) by hand at increasingly fast rate (purple). The resulting measured torque is shown in the second row of axes in black. 28
- 3.1 The skeletal model we use to simulate neuromuscular reflex control.  
The model consists of seven segments: left and right feet, shanks, and thighs, as well as a lumped head-arms-trunk (HAT) segment. Flexion joint angles are positive, extension joint angles are negative, and the zero angle configuration represents standing. 29
- 3.2 Hill-type muscle tendon unit with contractile element (CE), parallel elasticity (PE), and series elasticity (SE). 31
- 3.3 Force-length relationship of the CE. 31
- 3.4 Force-velocity relationship of the CE. 31
- 3.5 PE and SE force length relationship. For the PE,  $l_{\text{ref}} = l_{\text{opt}}$  and  $\epsilon_{\text{ref}} = \epsilon_{\text{PE}}$ . Likewise, for the SE,  $l_{\text{ref}} = l_{\text{slack}}$  and  $\epsilon_{\text{ref}} = \epsilon_{\text{SE}}$ . 32
- 3.6 Biped walking model with labeled muscles. 32
- 3.7 The idealized swing leg control guides the leg towards a desired landing leg angle  $\alpha_{\text{tgt}}$  through three phases 35
- 3.8 (a) Custom transfemoral prosthesis with series elastic actuators. In experiments in this thesis, we use an adaptor to test the prosthesis with able-bodied subjects. (b) During stance, we propose a control based on a neuromuscular model of human physiology that generates joint torques through virtual muscles that are stimulated by hypothesized local reflex pathways. 38
- 3.9 Universal stance/swing state machine utilized for all hardware experiments. 39
- 4.1 Control performance of simulated prosthesis on rough terrain. The distances walked over terrains with different ground roughness are compared between the amputee model using a powered knee-ankle prosthesis with impedance control (green) and hybrid neuromuscular control (blue) as well as with the unimpaired human model (red). Shown are the median and range (25<sup>th</sup> and 75<sup>th</sup> percentiles) of the covered distances for 50 terrains sampled at each roughness level. 43

- 4.2 Tripping response of the amputee model with neuromuscular (A) and impedance control (B) of the prosthesis. Shown are the prosthetic toe trajectories during undisturbed gait (dashed line) and when disturbed by a  $15\text{ N}\cdot\text{s}$  impulse (solid line). The neuromuscular controller effectively responds to the disturbance and maintains a qualitatively similar toe trajectory. The impedance controller leads to foot scuffing and an eventual fall. 45
- 5.1 Learning from preferences. (a) Mean and standard deviation of  $P(f_t|D_n)$  (blue) after two preferences queries (orange) from the true objective function (purple). (b) Mean of  $P(f_t|D_n)$  (blue) and means of  $P(f_t|D_n, x_m^*)$  (green) for two samples of  $x_m^*$ . PES-P queries a new comparison (orange) for which the preference is currently uncertain, but on average is certain after conditioning on all  $x_m^*$ . 49
- 5.2 Performance of predictive entropy search with preferences (PES-P), expected improvement (EI), and Latin hypercube random sampling (LH) for optimizing random objective functions sampled from a GP (a-d), and tuning feedback control parameters of random linear systems (e-f) and a biped walking model (g-h). Shown are the median and interquartile range over 20 trials of the immediate regret (IR) against the number of preference queries. Black stars indicate iterations for which PES-P achieves statistically significant stochastic reductions in IR compared to both EI and LH according to two-sided Mann-Whitney  $U$  tests ( $p < 0.05$ ). 53
- 5.3 Results of the offline optimization that fits the neuromuscular model to intact-subject gait data. Shown are the knee and ankle torques for two different subjects. These plots show there can be significant inter-subject gait variability. 61
- 5.4 Total Copeland score achieved by each parameter set across all five subjects. 63
- 5.5 Median angles and moments at  $0.8\text{ m/s}$  for all parameter sets for all subjects. Thicker weight solid lines indicate each subject's gait with their preferred parameters. Dashed lines indicate gait with hand-tuned parameters. The grey shaded regions show the mean and three sigma intact subject gait data (from the extra slow walking data in [Bovi et al., 2011]). 64
- 5.6 Average net ankle work for each subject at each speed. Red bars indicate trials where speed-adaptive gains were used whereas green bars indicate trials performed with the gains for  $0.8\text{ m/s}$ . Stars indicate statistically significant differences between the work produced by the speed adaptive gains and that produced by the  $0.8\text{ m/s}$  gains ( $p < 0.05$ ). 65
- 6.1 Example of fit to subject data achieved by neuromuscular model. 70

- 6.2 Example of fit to subject data achieved by impedance control model 72
- 6.3 Average user ratings across all trials in both the undisturbed and disturbed walking conditions when walking without the prosthesis (No Pros) and with the Neuromuscular (NM) prosthesis control and impedance (IMP) prosthesis control. Grey bars show the mean across subjects. Statistical significance assessed by Welch's *t*-test. \*:  $p < 0.05$ , \*\*:  $p < 0.01$ , \*\*\*:  $p < 0.001$ . 74
- 6.4 Total number of falls across all trials in both the undisturbed and disturbed walking conditions when walking without the prosthesis (No Pros) and with the Neuromuscular (NM) prosthesis control and impedance (IMP) prosthesis control. Grey bars show the median number of falls across all subjects. Statistical significance assessed by Wilcoxon signed-rank test. \*:  $p < 0.05$ , \*\*:  $p < 0.01$ . 75
- 6.5 Torso pitch angle variation. Angle variation calculated as the interquartile range of torso angles after the median torso angle trajectory over the strides in a trial is subtracted out. For the prosthesis trials, we report the average variation across the five trials for each condition. Grey bars show the mean across subjects. Statistical significance assessed by Welch's *t*-test. \*:  $p < 0.05$ , \*\*\*:  $p < 0.001$ . 75
- 6.6 Torso roll angle variation. Angle variation calculated as the inter quartile range of torso angles after the median torso angle trajectory over the strides in a trial is subtracted out. For the prosthesis trials, we report the average variation across the five trials for each condition. Grey bars show the mean across subjects. Statistical significance assessed by Welch's *t*-test.\* \* \*:  $p < 0.001$ . 76
- 6.7 Fraction of steps for which impedance control successfully transitions through all three stance phases. Introduction of gait disturbances significantly decreases the transition success rate. Grey bars show the mean success rate across all users. Statistical significance assessed by Welch's *t*-test. \*\*\*:  $p < 0.001$ . 77
- 6.8 Comparison of user scores of optimal versus suboptimal parameters for the neuromuscular and impedance control strategies. Grey bars show the mean user rating across subjects. Statistical significance assessed by Welch's *t*-test. \*\*:  $p < 0.01$ . 77
- 6.9 Comparison of number of falls of optimal versus suboptimal parameters for the neuromuscular and impedance control strategies. Grey bars show the median number of falls across subjects. Statistical significance assessed by Wilcoxon signed-rank test. 78
- 6.10 Normal Walking, impedance and neuromuscular control ankle work. 79

- 7.1 a) Utilizing minimum jerk trajectories during swing does not allow for appropriate adaptation of swing trajectories to enable obstacle avoidance. b) Our adaptive system learns online to detect the presence of an obstacle from the amputee's late stance/early swing movements. Once detected, the controller modifies the trajectories of the knee and ankle to achieve improved obstacle clearance. 82
- 7.2 Forward-Backward Classifier Overview. The backwards classifier uses features from the entire swing to provide training class labels to a forwards classifier. The forwards classifier uses features from late stance and early swing in order to predict if an upcoming swing will be an obstacle avoidance attempt. 84
- 7.3 Knee Angle Regression Feedback. In order to enable volitional control of the knee and ankle flexion angles to allow users to achieve greater flexion angles for larger obstacles, we implement a feedback system that uses the backwards classifier class score to quantify obstacle difficulty. After each step, the system increases the desired target angle for that step's forward features proportionally to the normalized back classifier score. We also decay the current desired target angle for those features to prevent continual growth of the target angle. The regression is retrained every ten avoidance attempts. 85
- 7.4 Bang-bang obstacle avoidance trajectories (yellow) vs normal minimum jerk trajectories (blue) for the knee and ankle. 86
- 7.5 Our powered transfemoral prosthesis prototype features series elastic actuators at both the knee and ankle joints for accurate torque control. We mount an IMU (3-Space Sensor, Yost Labs) to the thigh in order to measure hip angle and angular velocity and thigh linear accelerations. Able-bodied subjects wear the prosthesis via an L-shaped adapter (shown), whereas amputee subjects can attach the prosthesis to their personal socket via a standard pyramid adapter. 87
- 7.6 Obstacle height vs backwards classifier score for (a) the able-bodied and (b) amputee subjects. The system uses the backwards classifier score as a metric for obstacle avoidance difficulty. This score is used in a feedback loop that forms the training set for the flexion target angle regression (c-d). With this feedback system, the able bodied user (e) is able to achieve a degree of volitional control over flexion angle as evidenced by the linear relationship between knee flexion angle and obstacle height ( $R^2 = 0.31$ ). However, the amputee (f) was not able to achieve meaningful control over the flexion of the prosthesis ( $R^2 = 0.10$ ), possibly due to the decreased experience level of this subject. 89

- 7.7 Kinematic model of the user and prosthesis used for state estimation and motion planning. The model includes the hip (H), knee (K), ankle (A), heel (L) and toe points (T). Additionally, the start ( $Lid_0$ ) and end ( $Lid_f$ ) points of the LIDAR beam (with length  $\ell$ ) are indicated. The IMU is located at point  $I$ . Both the LIDAR and IMU are mounted to the thigh portion of the powered knee-and-ankle prosthesis. 93
- 7.8 Trajectories of extended Kalman Filter (EKF) estimate of the position of the leg during swing (blue). Ground truth positions given by motion capture (yellow). EKF estimate without LIDAR information shown in red. Thick lines show the leg configuration at peak toe height during swing. Dotted lines indicate heel trajectories while dashed lines show the toe trajectories. Knee and ankle trajectories given by solid lines. 95
- 7.9 Example of hip angle and height trajectory predictions 0.15 s into swing. The prediction algorithm uses the previous 10 measured hip angles and heights (sampled at 100 Hz, black dots) along with the learned joint distributions of hip angles/heights versus time (red) to obtain the conditional distributions of future hip angles/heights (blue). The planning algorithm uses the means of the conditional distributions to generate knee and ankle trajectories. The actual hip height and angle trajectories are shown in black. 96
- 7.10 Planning Algorithm Steps: Panels B and D show the generated knee and ankle trajectories respectively. The planned trajectory (red) lies within the computed bounds (dashed gray). In contrast, standard minimum jerk trajectories (blue) do not respect the bounds, thereby increasing the tripping hazard. Panels C and E show examples of inverse kinematics (IK) solutions for toe (purple) and heel (yellow) contact for the knee and ankle joints respectively. We use the IK solutions to generate bounded regions that the planned trajectory can safely traverse. We consider ground contact constraints for only the first half of the remaining swing duration after which we only consider joint angle constraints. We use Dijkstra's algorithm to select regions (green) that allow a path from the start point to the desired final point. Bounded regions that do not lie on the path are shown in red. Panel A shows the corresponding prosthesis motion. 98
- 7.11 Knee and ankle trajectories produced during normal walking and while eliciting trips. To avoid tripping during trip elicitation trials, trajectories generated by the proposed approach often flex the knee to a greater degree and for longer before quickly extending at the end of swing. At the ankle joint we see overall greater variability in the generated trajectories during the trip elicitation condition versus normal walking. 101

- 7.12 Kernel density estimate of the probability of various landing knee flexion angles with the proposed swing control (blue) and standard min-jerk swing control (red). Large landing knee angles indicate premature toe contact during swing. 102
- 7.13 Kernel density estimate of the probability of various integrated ground reaction force values for the proposed swing control (blue) and standard min-jerk swing control (red). Large integrated GRF during the swing phase is indicative of the toe scuffing on the ground. 103
- 7.14 Average toe height vs average hip height for the proposed swing control (blue) and standard min-jerk swing control (red). The toe height during swing is less sensitive to the hip height when using the proposed swing control than when using the min-jerk swing control. 104
- 8.1 Examples of learned control surfaces. We fit the surfaces to gait data from Moore et al. [2015]. This data includes information for three speeds, 0.8, 1.2, and 1.6 m/s, which are shown as the clustered trajectories in the above panels. For an automatic transition to standing, the surfaces are additionally fit to virtual data that causes the joint angles to approach 5 deg, the velocities to approach 0 deg/s, and the joint torques to approach 0 N·m as the phase velocity goes to zero. 111
- 8.2 CMU powered prosthesis used in experiments. The prosthesis has brushless motors at the knee and ankle joints, series elastic actuators for torque control, and an IMU mounted to the thigh portion to measure residual limb angle. 112
- 8.3 Ability to reproduce normal walking. Average knee angle (row 1), ankle angle (row 2), knee moment (row 3), and ankle moment (row 4) for the GP-EKF controller (column 1), neuromuscular controller (column 2), and impedance controller (column 3). Black traces and gray shaded areas show the mean and two standard deviations for very slow human walking data (from [Bovi et al., 2011]). Colored lines show individual subject data. Amputee gait data indicated by dashed lines and experienced user data indicated by dash-dot lines. 115
- 8.4 Average kinematic (a,b) and kinetic (c,d) errors produced by the three different controllers compared to able-bodied data. GP-EKF produces significantly more natural knee angles than NM or IMP control, but slightly less natural ankle angles and joint torques. Grey bars show median of subject data, circle markers indicate able-bodied subject data, triangle markers indicate amputee data, and square markers indicate experienced able-bodied user data. \* :  $p < 0.05$ , \*\* :  $p < 0.01$ . 116
- 8.5 Robustness to ground height disturbances. Number of falls accrued for each controller during ground height disturbance trials. GP-EKF control significantly reduced the number of falls compared to IMP control. 116

- 8.6 Adaptability of phase estimate. Mean phase error of EKF versus time-based phase estimation when walking with sinusoidally varying treadmill speed. The EKF significantly improves phase tracking compared to the time-based estimate. 117
- 8.7 Example of EKF-based phase estimation (red) versus time-based phase estimation (blue) for one subject. Due to step-to-step speed variations caused by the sinusoidally varying treadmill speed, the time based phase estimation accrues significant errors. In contrast, the EKF-based phase estimate is able to respond to changes in gait within the gait cycle, thus reducing phase estimation errors. 117
- 8.8 Response to sudden treadmill stops. Estimated phase (a) and phase velocity (b), and the measured knee (c) and ankle (d) angles when the treadmill is suddenly stopped half way through stance. When gait stops, the EKF-estimated phase stabilizes to a constant value (solid traces), phase velocity falls to zero, and the joint angles approach 5 deg as desired by the control surfaces (compare fig. 8.1). The time-based phase estimate fails to respond (dashed lines). Vertical black dotted line indicates heel strike of final stance phase. 118
- 8.9 GP-EKF phase-based control with fixed control surfaces and increased ankle impedance. 120

## *List of Tables*

2.1	Designed and achieved design specifications. (*Maximum total ankle torque is 290 N · m achieved at 10 degrees of dorsiflexion.)	22
3.1	Segment lengths ( $l_s$ ), center of mass ( $d_{COM}$ ) and joint ( $d_{Joint}$ ) locations measured from the distal end, masses ( $m$ ), and inertias ( $J$ ) approximated from Günther and Ruder [2003].	29
3.2	Joint limits for the hip, knee, and ankle joints listed in degrees. Positive joint angles represent flexion and negative joint angles represent extension (see fig. 3.1).	30
3.3	Neuromuscular parameters for shared entities (left) and the hamstring muscle (right)	32
5.1	Parameters optimized to generate parameter sets for dueling bandits optimization	60
6.1	Parameters optimized for parameter set generation for experiment comparing neuromuscular and impedance control	69
6.2	Tally of observed reasons for falls across all subjects and across both the undisturbed and disturbed walking conditions. Falls were manually classified based on video and logged prosthesis data. An individual Fall can be assigned more than one reason.	76
7.1	Classifier Performance, Able-Bodied	87
7.2	Classifier Performance, Amputee	88
7.3	Obstacle Avoidance Success Rates	88
7.4	Online and Offline Forward Classifier Performance, Amputee	88



# 1

## *Introduction*

### *1.1 Motivation*

SIX HUNDRED THOUSAND lower-limb amputees currently live in the United States according to recent estimates [Ziegler-Graham et al., 2008]. People undergo amputations due to a variety of reasons including traumatic injuries from workplace accidents, traffic collisions, and as casualties of war. In addition, a large percentage (54%) suffer from the loss of a limb due to complications arising from dysvascular disease associated with diabetes. Consequently, largely due to the expected increase in diabetes in the coming years, Ziegler-Graham et al. [2008] estimate that by 2050 the number of amputees living in the United States will likely double.

Currently, prosthetists often prescribe transfemoral amputees (those with amputations between the hip and knee joints) an energy storage and return composite foot such as the Thrive Foot (Freedom Innovations; Irvine, CA; fig. 1.1c) along with a microprocessor-controlled, mechanically-passive knee prosthesis. These knee prostheses feature control algorithms that adjust the knee's resistance in response to kinematic and force data measured by sensors embedded in the device. Examples of microprocessor-controlled prosthetic knees include the C-Leg (Otto Bock; Duderstadt, Germany; fig. 1.1a), which has an adjustable hydraulic damping system, and the Rheo Knee (Össur; Reykjavik, Iceland; fig. 1.1b), which achieves variable damping via a magnetorheological fluid. While Johansson et al. [2005] show these microprocessor-controlled knees can improve amputee gait characteristics by decreasing metabolic energy consumption and peak hip torque and increasing gait smoothness compared to that provided by fully-passive knee prosthesis, these prostheses still cannot fully replicate healthy leg behavior as they are incapable of providing positive net power during the gait cycle and are limited to providing positive power only during fixed portions of the gait cycle.



(a) C-Leg™ Knee ©Ottobock



(b) Rheo™ Knee ©Össur



(c) Thrive™ Foot ©Freedom Innovations

Figure 1.1: Examples of microprocessor-controlled mechanically-passive knee prostheses (a,b) and a energy storage and return ankle-foot prosthesis (c).

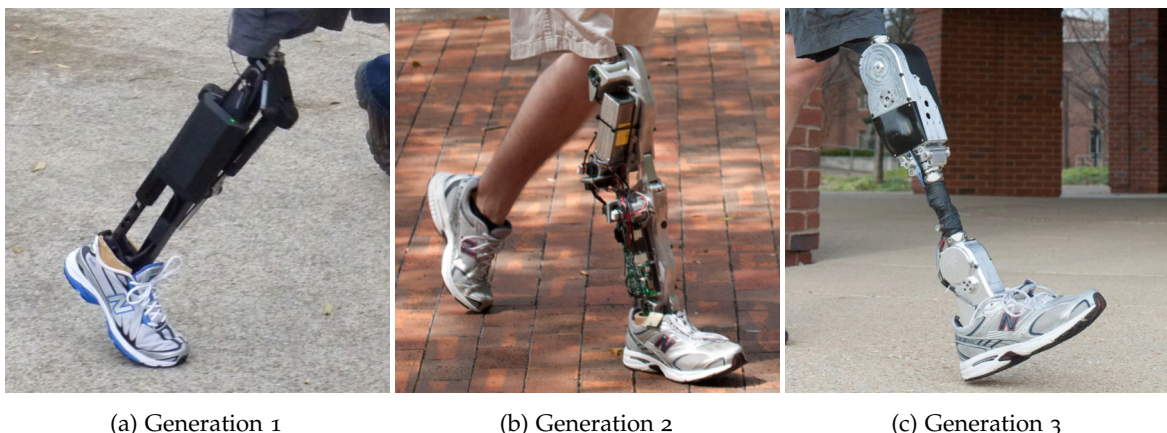
Control of positive power generation is important as positive power is evident in a number of locomotion tasks. In the knee joint, we see positive power during level walking [Perry and Burnfield, 2010], walking up stairs [Nadeau et al., 2003], running [Buczek and Cavanagh, 1990], and jumping [Hubley and Wells, 1983]. In addition, active knee flexion and extension muscle activations have been noted during stumble recovery [Eng et al., 1994]. At the ankle joint, passive spring-like prostheses cannot replicate the positive net work seen in the ankle joint during level ground walking, which is essential for push-off and forward propulsion [Perry and Burnfield, 2010].

Consequently, lower-limb amputees and especially *transfemoral amputees*, those with above the knee amputations, equipped with mechanically-passive prostheses suffer from a number of issues including markedly increased energy consumption [Waters et al., 1976], abnormal gait kinematics [Jaegers et al., 1995], and an increased likelihood of falling [Miller et al., 2001]. Specifically, large percentages of transfemoral amputees report they are unable to complete tasks such as walking outside in inclement weather (47.4%), walking while carrying a load (42.7%), walking up or down stairs without a handrail (38.5%, 37.9%), walking outside on uneven terrain (29.5%), picking up an object from the ground (28.1%) or getting up from the floor after a fall (22.8%) [Gauthier-Gagnon et al., 1999].

Importantly, these gait pathologies can lead to an avoidance of walking [Gauthier-Gagnon et al., 1999]. This is especially true in the case of falls. Miller et al. [2001] find 49.2% of lower limb amputees feared falling and that of those afraid of falls 76% avoided physical activity as a result. Avoidance of physical activity is eminently concerning as it may lead to reduced strength, endurance, and balance, feeding a positive feedback loop that causes further debilitation.

To help remedy this situation, in the past decade academic re-

Figure 1.2: Vanderbilt University's Robotic Transfemoral Prostheses. Images courtesy of Michael Goldfarb.



search groups and companies have developed robotic powered knee and ankle prostheses for lower-limb amputees. These prostheses feature actuators at the knee and/or ankle that, if controlled correctly, could potentially restore the kinetics, kinematics, and reactions of the healthy human leg. Notable examples include three generations of transfemoral prostheses developed by Vanderbilt University (fig. 1.2) [Sup et al., 2009, Lawson et al., 2013, 2014] and the Biom powered ankle (fig. 1.3) [Herr and Grabowski, 2011]. These powered prostheses have helped amputees walk on level ground more naturally and efficiently, as well as walk up stairs and slopes [Sup et al., 2011, Lawson et al., 2013], run [Huff et al., 2012, Shultz et al., 2015], perform sit-to-stand [Varol et al., 2009], and dance [Rouse et al., 2015]. These results illustrate the benefits of powered prostheses as many of these tasks require positive joint power and thus would be difficult to perform with mechanically-passive prostheses.



Figure 1.3: Biom Robotic Ankle Prosthesis. Photo by Steve Jurvetson, CC BY 2.0, Link (cropped from original).



## 2

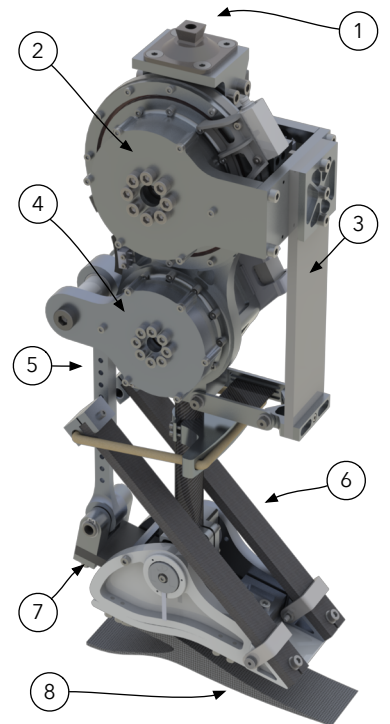
# *Transfemoral Prosthesis Development*

### *2.1 Mechanical Design*

TO TEST OUR PROPOSED NEUROMUSCULAR CONTROL APPROACH, and its ability to help subjects maintain or recover their balance, we build a custom transfemoral prosthesis capable of reproducing dynamic locomotion tasks. The proposed design, shown in fig. 2.1, uses brushless electric motors coupled to harmonic drive gear sets to drive both the knee and ankle joints. Additionally, the joints employ series elastic actuation to enable accurate torque control and to protect the prosthesis' gear sets from sudden impacts. The design also features a unidirectional parallel spring in the ankle that partly offsets the torque demands on the ankle motor. We design both joints to meet the demands of dynamic locomotion tasks such as running and trip recovery.

The overall design concept sits in a niche between low powered prostheses designed with commercial applicability in mind [Sup et al., 2007, 2009, Lawson et al., 2014, Rouse et al., 2015, Martinez-Villalpando et al., 2011] which feature onboard actuation and power sources, and high-powered tethered systems [Caputo and Collins, 2013, Caputo et al., 2015] with off-board actuation designed exclusively for use in lab environment. Our design features onboard actuators that are more powerful than those used in standalone devices, but less capable than those employed in tethered devices. To ensure a reasonable overall weight the device's batteries, motor drivers, and computers are off-board. With this design, we expect to be able to test control ideas without encountering hardware performance limitations as with a tethered device. At the same time the device is capable of functioning outside of the lab environment like a standalone prosthesis.

Table 2.1 shows the desired design specifications for the transfemoral prosthesis and the values achieved by the final design. To



- 1) Pyramid Adaptor
- 2) Knee Motor
- 3) Knee Series Spring
- 4) Ankle Motor
- 5) Adjustable Height
- 6) Unidirectional Parallel Spring
- 7) Ankle Series Spring
- 8) Composite Foot

Figure 2.1: Render of proposed powered knee and ankle prosthesis design. The prosthesis includes series elastic actuators to enable accurate torque control and a unidirectional parallel ankle spring to offset the required angle torque.

Specification	Desired Value	Theoretical Value	Achieved Value
Maximum Knee Torque	160 N · m	170 N · m	
Maximum Knee Speed	1.80 rev/s	1.93 rev/sec	
Knee Torque Bandwidth	4 Hz	11.7 Hz	
Maximum Ankle Torque	200 N · m	170 (+120*) N · m	
Maximum Ankle Speed	1.14 rev/s	1.22 rev/s	
Ankle Torque Bandwidth	3.5 Hz	5.9 Hz	
Weight	6.8 kg	5.9 kg	
Minimum Height	42.5 cm	42 cm	

obtain these design specifications we examined a number of studies that elicited trip responses.

We specify desired joint torque and speed values to meet the requirements of demanding tasks such as running. The maximum knee torque specification comes from the findings of Whitley [2008], who tested the joint torques used during recovery from a simulated fall. The maximum knee speed requirement comes from Grabiner et al. [1993], who tested subjects' responses to simulated trips induced by unseen obstacles on a walkway. We obtain the maximum ankle torque requirement from Pijnappels et al. [2005], who tripped subjects using obstacles that could suddenly emerge through the floor. The maximum ankle speed requirement comes from the running data of Novacheck [1998]. We set to the minimum height specification, measured between the center of the knee and bottom of the foot, to accommodate the 10<sup>th</sup> percentile female [Gordon et al., 1989]. Finally, the required weight corresponds to the mean leg weight of a 50<sup>th</sup> percentile male [Winter, 2009].

### 2.1.1 Knee Joint

In addition to achieving the maximum speeds and torques found in table 2.1, we design the knee joint so that it can reproduce the torque and speed required for a 80 kg person to run at 3.2 m/s as measured by Novacheck [1998]. To reproduce this trajectory in the knee joint, we utilize a RoboDrive ILM 85 × 13 HS-SP motor coupled to a Harmonic Drive Gear set with a 50:1 reduction (CSG-25-50). Figure 2.2 shows the motor torque and speed required to reproduce a running trajectory assuming a gear efficiency of 75%. In this plot, we see that the running trajectory lies within the speed-dependent torque limit of the motor. Moreover, the root mean squared torque of this trajectory (1.46 N · m) exceeds the torque rating of the motor (1.43 N · m) by just 2%. Therefore, the knee joint should be able to

Table 2.1: Designed and achieved design specifications. (\*Maximum total ankle torque is 290 N · m achieved at 10 degrees of dorsiflexion.)

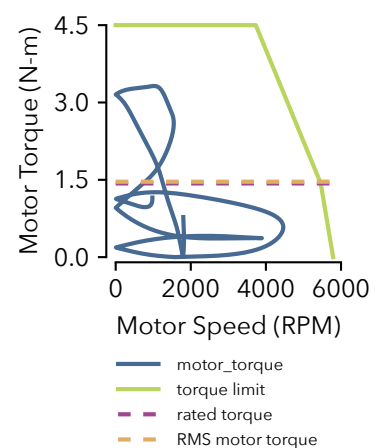
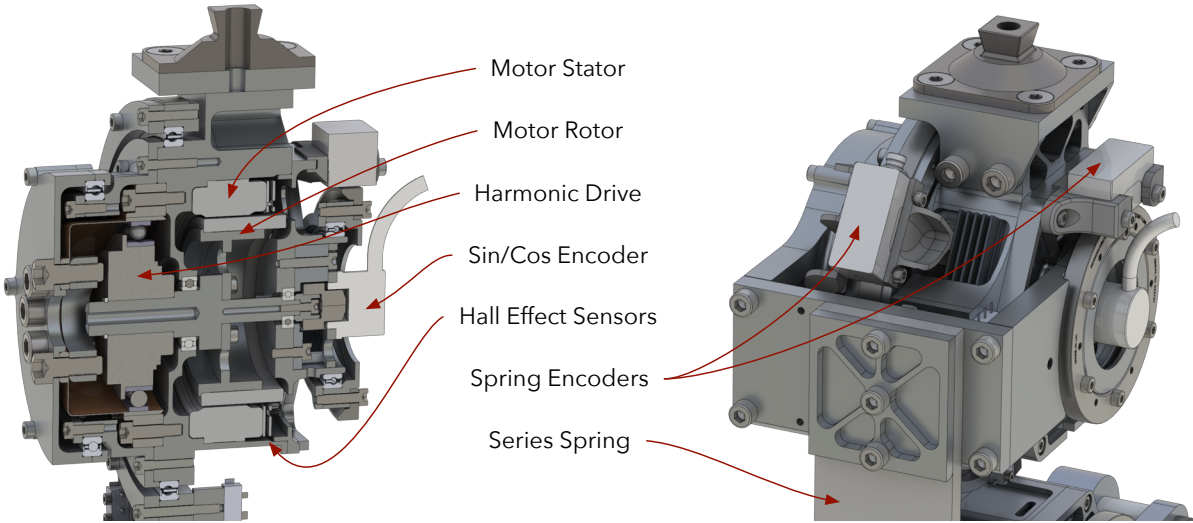


Figure 2.2: Knee motor torque required for running



provide the necessary torque to enable running for a short amount of time, or continuously for lighter subjects or at a slightly reduced speed.

Figure 2.3 shows the internal and external design of the knee joint. The primary component in the knee joint is the stator housing. On top of the housing is a standard pyramid adaptor that allows the prosthesis to connect to amputee's sockets. Within the stator housing, lies the brushless motor stator, rotor, and harmonic drive gear set. We sense absolute rotor angle for commutation of the brushless motor via hall effect sensors and a magnetic complementary sin/cos encoder. To incorporate series elasticity, we take inspiration from the design of the bipedal robot Atrias [Grimes, 2013], which uses fiberglass series leaf springs. In our design, the output of the gear set drives the proximal end of a fiberglass leaf spring in series with the shank. Two Renishaw Resolute absolute encoders measure the deflection of this spring to enable torque control.

In addition to allowing for accurate torque control, as shown by Au et al. [2007], Au and Herr [2008], the series elasticity also plays a crucial role in protecting fragile gear components from impact loads. To choose the spring stiffness for the knee joint, we simulate the prosthesis impacting a rigid wall with the foot during swing. To do this, we construct a model of the prosthesis in Matlab Simulink Simscape Multibody that includes the series elasticity, gear dynamics, and motor electrical dynamics. Figure 2.4 shows the simulation environment. The prosthesis is attached to the distal end of a thigh segment with a fixed hip position. We control the hip via the ideal swing leg control outlined in ?? (eq. (3.30)) and consider the case where the external

Figure 2.3: Internal and external design of the knee joint.

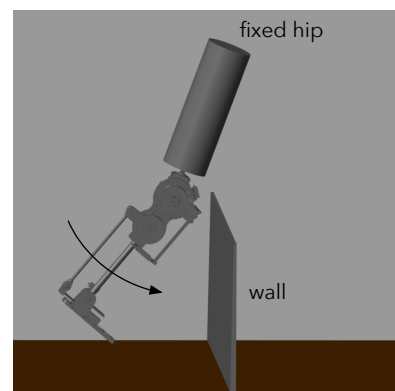


Figure 2.4: Impact simulation we used to determine appropriate series spring stiffness.

voltage applied to the motor is zero. This simulation suggests that a spring stiffness under  $2300 \text{ N}\cdot\text{m}/\text{rad}$  will ensure that the peak impact torque remains lower than the peak allowable impact torque of the Harmonic Drive of  $242 \text{ N}\cdot\text{m}$ .

We can also estimate the torque bandwidth of the actuator by analyzing the SEA dynamics for the system depicted in ?? [Assuming](#)  [check reference](#)  
the load is fixed, the transfer function between the motor and load torques is given by

$$\frac{\tau_l}{\tau_m} = \frac{k/J_m}{s^2 + k/J_m} \quad (2.1)$$

where  $\tau_l$  and  $\tau_m$  are the load torque and post-gearbox motor torque respectively.  $J_m$  is the sum of the reflected motor rotor inertia and inertia of components that form the motor-side attachment of the spring, which has stiffness  $k$ . From this equation we calculate the bandwidth of the system to be

$$f_{3dB} = \frac{\sqrt{k/J_m}}{2\pi}. \quad (2.2)$$

For a spring stiffness of  $2300 \text{ N}\cdot\text{m}/\text{rad}$  we estimate the torque bandwidth is  $11.7 \text{ Hz}$ . This value exceeds the required torque bandwidth of  $4 \text{ Hz}$  given by Sergi et al. [2012] (obtained by analyzing the torque data for walking reported by Winter [2009]). However, it should be noted that this is a very crude estimate of bandwidth. On the one hand, it may underestimate the true value, as it assumes that to achieve a desired output torque, the motor control applies the same torque to the motor side of the spring. In practice, a closed-loop torque control can transiently apply much larger torques to the motor side in order to achieve faster convergence to a desired steady-state output torque. On the other hand, this value may also underestimate the true bandwidth, as it does not consider the motor's voltage-current dynamics or gear friction.

### 2.1.2 Ankle Joint

In the ankle joint we utilize a RoboDrive ILM  $70 \times 10$  HS-SP motor coupled to a Harmonic Drive Gear set with a  $100:1$  reduction (CSG-20-100). As with the knee joint, we design the ankle joint to satisfy the requirements listed in table 2.1. Specifically, for the ankle joint we pay considerable attention to the tripping condition described by Pijnappels et al. [2005], in which the ankle generates a peak torque of  $202 \text{ N}\cdot\text{m}$ .

To avoid using a large and heavy motor to achieve this peak torque, we take inspiration from previous prosthetic ankle designs that employ a unidirectional parallel spring in the ankle joint that

performs the conservative portion of the ankle's torque versus angle trajectory during normal walking [Au et al., 2007, Au and Herr, 2008, Sup et al., 2009, Lawson et al., 2014]. The parallel spring offsets the required motor torque, as the actuator only needs to provide the difference between the desired torque and the torque provided by the parallel spring. Figure 2.5 shows the torque versus angle curve during level ground walking (Winter [2009], scaled to 80 kg person). In green we show the torque generated by a 700 N·m/rad parallel spring optimized to minimize the root-mean-squared motor torque for this trajectory. From this plot, we see that with the parallel spring, the peak torque is lower than the repeated peak torque limit of the Harmonic Drive Gear set.

The tripping data obtained by Pijnappels et al. [2005] shows that the ankle kinematics during trip recovery are similar to those seen during normal walking. Therefore, the parallel spring, should be able to contribute torque during the tripping case as well. To confirm this, fig. 2.6 shows the motor torque required for trip recovery (obtained by scaling walking torque data from Winter [2009] to have a peak torque of 202 N · m) We see that the inclusion of the parallel spring allows the prosthesis to produce enough net torque to reproduce the trip recovery trajectory without exceeding the torque limit of the motor.

Finally, fig. 2.7 shows the torque and speed required of the motor for running [Novacheck, 1998]. In this case, we use an ankle parallel stiffness of 267 N·m/rad. From this plot, we see that this combination of ankle motor and spring is nearly sufficient for running. Increasing the voltage of the prosthesis from 48 V to 60 V or decreasing the gear ratio from 100:1 to 80:1 will allow the torque trajectory to fit completely within the motor limits.

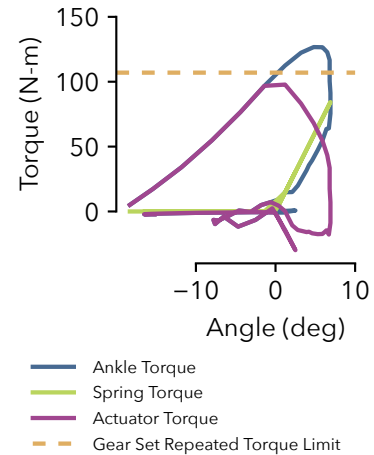


Figure 2.5: Ankle torque vs angle curve during steady, level-ground walking (blue) (Winter [2009] scaled to 80 kg person). A unidirectional parallel spring can provide a portion of this torque (green) and reduces the required actuator torque (purple) to lie under repeated torque limit of the Harmonic Drive Gear set (orange).

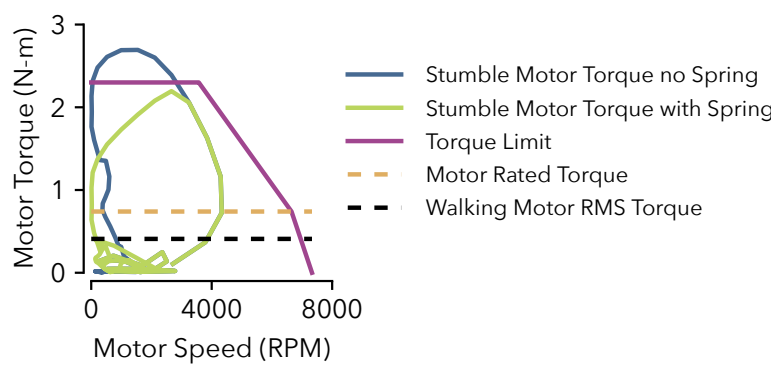


Figure 2.6: Ankle motor torque required to take the trip recovery action observed by Pijnappels et al. [2005] (blue, trajectory obtained by scaling walking data from Winter [2009] to a peak torque of 202 N · m, 75% gear efficiency assumed). Using a parallel spring allows the motor to produce the required torque (green) while remaining within its torque limit (purple).

Figure 2.8 shows an internal view of the ankle actuator and external views of the actuator and foot mechanism. In the ankle design, the output of the actuator actuates the foot through a four-bar mechanism. The actuator pulls or pushes on the proximal end of a length-adjustable tendon. The distal end of the tendon attaches to one end of a fiberglass series elastic leaf spring that is also connected to the foot. By measuring the angles of the ankle actuator output and the ankle joint and using the equations of the four-bar mechanism's kinematics, we can calculate the deflection of the leaf spring and thus the torque applied to the ankle.

The design of the ankle actuator represents a second iteration of the knee actuator design and features two main improvements. First, it has increased space on the side of the motor for cable routing. Second, the ankle actuator has a solid rotor shaft. In contrast, the knee actuator's shaft is comprised of two parts: one that held the motor rotor and transferred power through the gear set, and another that held the sin/cos encoder's magnetic shaft component. In practice, these two components proved difficult to align, causing degraded performance of the sin/cos encoder. The ankle actuator's solid shaft ensures the encoder magnet stays aligned with the read head.

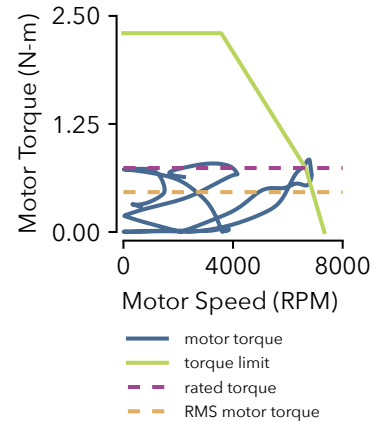


Figure 2.7: Ankle motor torque required to reproduce the running trajectory recorded by Novacheck [1998] assuming a parallel spring stiffness of  $267 \text{ N}\cdot\text{m}/\text{rad}$  and a gear efficiency of 75%.

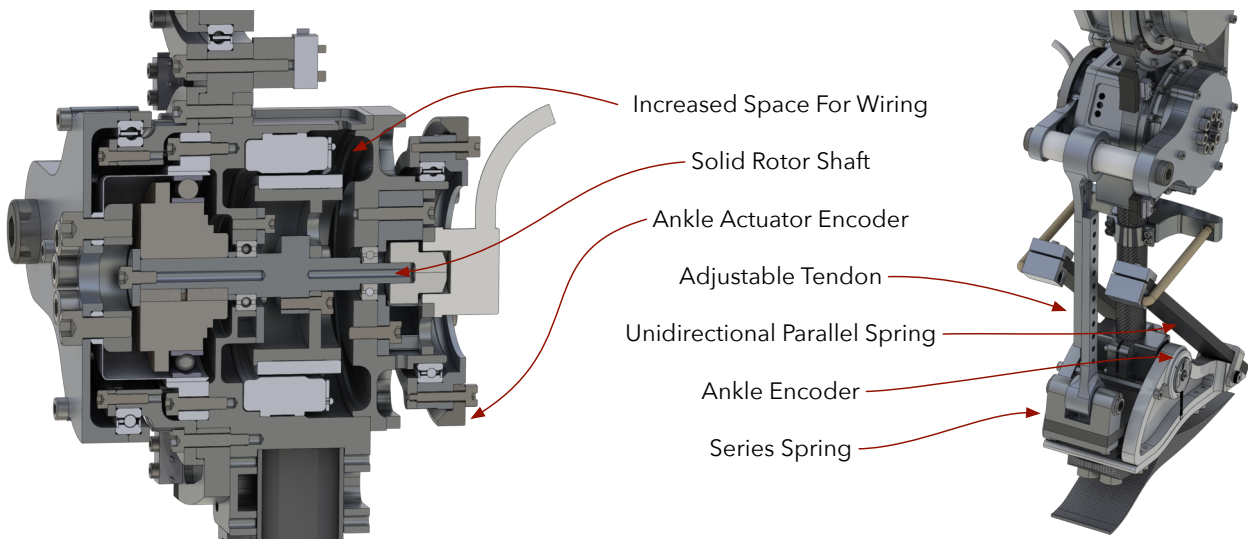


Figure 2.8: Internal and external design of the ankle joint.

As we did for the knee series spring, we again determine an acceptable ankle spring stiffness by performing an impact simulation. For the ankle, we simulate an 80 kg person stepping on the prosthesis when the motor driver provides the ankle motor with zero applied voltage. Figure 2.9 shows the simulation environment. From this simulation we find that a spring stiffness of about  $1000 \text{ N}\cdot\text{m}/\text{rad}$  should sufficiently protect the ankle gear set from impacts. This estimate is likely softer than necessary due to the additional series compliance in the amputee's socket and the composite foot that are not included in the simulation. Repeating the bandwidth calculation we performed for the knee spring, we estimate the ankle bandwidth may be around 5.9 Hz. This value exceeds the required torque bandwidth of 3.5 Hz given by Au and Herr [2008] (obtained by analyzing the torque data for walking reported by Winter [2009]).

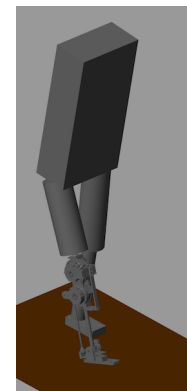


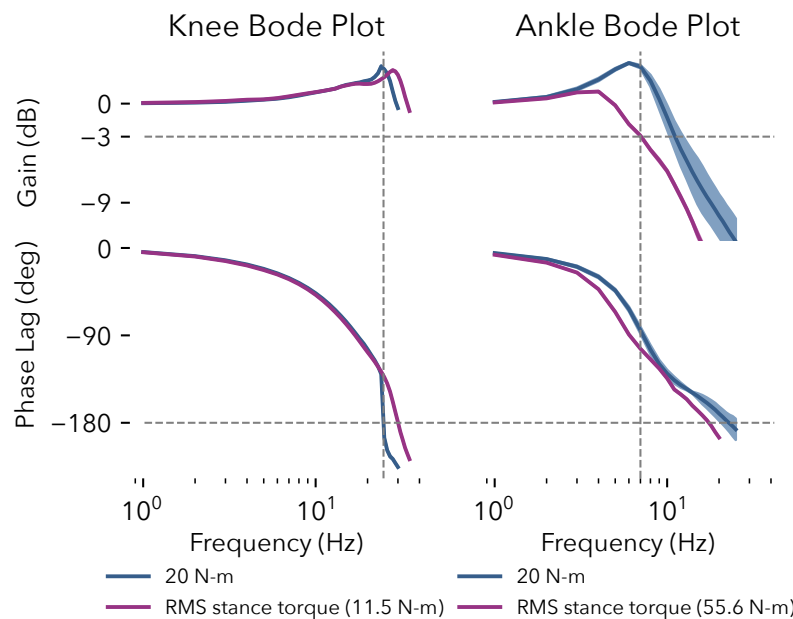
Figure 2.9: Impact simulation we used to determine appropriate series spring stiffness.

### 2.1.3 Ground Reaction Force Sensing

## 2.2 Series Elastic Actuator Control

## 2.3 Performance Evaluation

design of heel/toe grf sensors and plot of grf sensor readings



Closeup of final design

Pictures of test rig  
Figure 2.10: Experimentally obtained bode plots of knee and ankle actuator torque. Knee is phase limited at 24 Hz while the ankle is gain limited at 7 Hz.

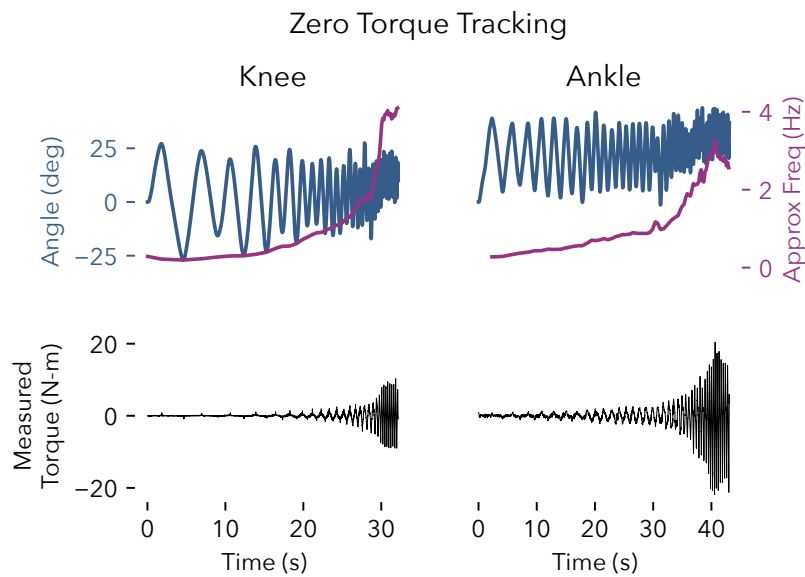


Figure 2.11: Zero torque tracking of knee and ankle joints. The prosthesis was fixed to a rigid mount and commanded to maintain zero net joint torque while the knee and ankle joints were manually oscillated (blue) by hand at increasingly fast rate (purple). The resulting measured torque is shown in the second row of axes in black.

torque tracking during walking RMS error

# 3

## *Neuromuscular Model*

IN THE FIRST PART OF THIS THESIS, we investigate the ability of neuromuscular reflex control to improve amputee gait robustness. To this end, here we provide a more detailed review the neuromuscular model components on which we base our prosthesis control. Four parts comprise the model: a mechanical simulation environment we use to obtain simulation results (section 3.1), biological motors modeled by the hill muscle model that apply torques to joints (section 3.2), and finally functionally-motivated stance (section 3.3) and swing (section 3.4) reflexes that implement the key behaviors required for walking.

### *3.1 Mechanical Model*

To obtain the simulation results we present in chapter 4, we construct a mechanical model in the Matlab Simscape Multibody environment similar to those presented in Geyer and Herr [2010], Song et al. [2013], Song and Geyer [2015]. This model represents the seven link biped in fig. 3.1 and includes two legs with thigh, shank, and foot segments as well as a lumped head-arms-trunk (HAT) segment. Table 3.1 lists the segment lengths, center of mass and joint locations measured from the distal end, masses, and inertias that approximate those of a 80 kg, 1.8 m tall person.

The mechanical model interacts with the environment through

	Feet	Shanks	Thighs	HAT
$l$ (cm)	20	50	50	80
$d_{COM}$ (cm)	14	30	30	35
$d_{Joint}$ (cm)	16	50	50	
$m$ (kg)	1.25	3.5	8.5	53.5
$J$ (kg)	0.005	0.05	0.15	3

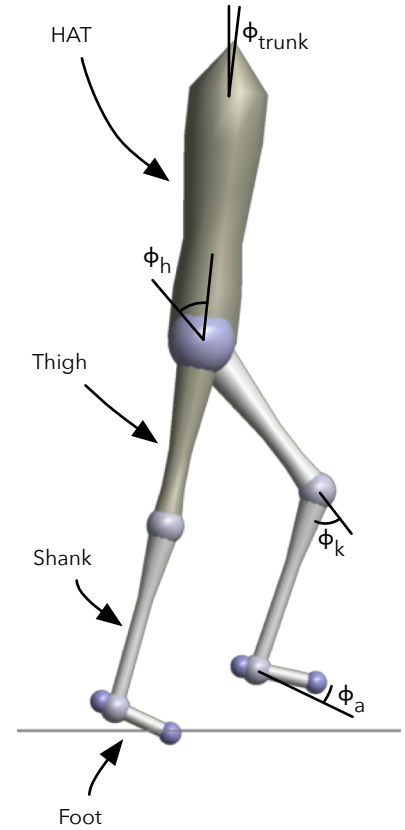


Figure 3.1: The skeletal model we use to simulate neuromuscular reflex control. The model consists of seven segments: left and right feet, shanks, and thighs, as well as a lumped head-arms-trunk (HAT) segment. Flexion joint angles are positive, extension joint angles are negative, and the zero angle configuration represents standing.

Table 3.1: Segment lengths ( $l_s$ ), center of mass ( $d_{COM}$ ) and joint ( $d_{Joint}$ ) locations measured from the distal end, masses ( $m$ ), and inertias ( $J$ ) approximated from Günther and Ruder [2003].

ground reaction forces on the toes and balls of the feet. Specifically, we use a 2-dimensional reduction of the 3D ground contact model presented in Song and Geyer [2013] to calculate forces in the normal and tangential directions with respect to the terrain. In the normal direction the force is

$$F_n = k_n \Delta n_c (1 + \dot{n}_c) (\Delta n_c > 0) (\dot{n}_c / v_{\max} > -1), \quad (3.1)$$

where  $k_n = 78.45 \text{ N/mm}$  is the stiffness coefficient in the normal direction and  $\Delta n_c$  and  $\dot{n}_c$  are the penetration direction and velocity in the normal direction. The form of the normal force is inspired by Günther and Ruder [2003] and Scott and Winter [1993] and represents a linear spring with multiplicative damping.  $v_{\max} = 3 \text{ cm/s}$  represents the maximum recovery velocity of the ground. If  $\dot{n}_c$  exceeds this velocity, ground contact is lost.

In the tangential direction, a state machine switches between two force models representing sliding and static friction. Sliding friction is given by

$$F_{t,slide} = -\text{sign}(\dot{t}_c) \mu_{slide} F_n \quad (3.2)$$

while static friction is given by

$$F_{t,static} = -k_t \Delta t_c \left( 1 + \text{sign}(\Delta t_c) \frac{\dot{t}_c}{v_{\max}} \right), \quad (3.3)$$

where  $\Delta t_c$  is the penetration in the tangential direction  $\dot{t}_c$  is the penetration velocity,  $\mu_{slide} = 0.8$  is the sliding coefficient of friction, and  $k_t = 78.45 \text{ N/mm}$  is the stiffness coefficient in the tangential direction.

The contact model begins in the sliding mode and switches to the static mode if  $\dot{t}_c < 1 \text{ cm/s}$ . It switches back to the sliding mode when  $|F_{t,static}| < \mu_{static}|F_n|$ , where  $\mu_{static} = 0.9$ .

Finally, the biped skeletal model includes soft joint limits to represent the skeletal joint limits on the knee, ankle, and hip joints. The functional form for the soft limit joint torque is identical to that of the normal ground reaction force given by eq. (3.1).

$$\tau_{jl} = k_{jl} \Delta \phi_{jl} (1 + \dot{\phi}_{jl}) (\Delta \phi_{jl} > 0) (\dot{\phi}_{jl} / \dot{\phi}_{\max} > -1), \quad (3.4)$$

where  $k_{jl} = 0.3 \text{ N}\cdot\text{m}/\text{deg}$  is the joint stiffness  $\Delta \phi$  and  $\dot{\phi}_{jl}$  are the joint limit penetration angle and velocity respectively, and  $\dot{\phi}_{\max} = 1 \text{ deg/s}$  is the maximum joint limit retraction velocity. Table 3.2 lists the engagement angles for the joint limits.

To obtain simulation results, we simulate the mechanical system with the ode15s variable step solver. We set the maximum step size to 10 ms, relative error tolerance to  $10^{-4}$ , and absolute error to  $10^{-6}$ .

Joint	ext. lim.	flex lim.
hip		50
knee	5	
ankle	-40	20

Table 3.2: Joint limits for the hip, knee, and ankle joints listed in degrees. Positive joint angles represent flexion and negative joint angles represent extension (see fig. 3.1).

### 3.2 Hill Muscle Models

Our proposed transfemoral prosthesis control is comprised of biological muscle actuators that are stimulated according to hypothesized reflex pathways. Specifically, we use a Hill-type *muscle tendon unit* (MTU) first described by Hill [1938]. It is comprised of a contractile element (CE) that represents muscle fibers and produces force when activated, a parallel elastic (PE) element that represents the stiffness of the collagen tissue between muscle fascicles, and series elastic (SE) element that models tendon stretch. Figure 3.2 shows the arrangement of these elements. Note that the PE and SE both are unidirectional springs with engagement lengths of  $l_{\text{opt}}$  and  $l_{\text{slack}}$  respectively.

The CE generates force according to

$$F_{\text{CE}} = F_{\max} A f_l(l_{\text{CE}}) f_v(v_{\text{CE}}). \quad (3.5)$$

In this equation, the force generated by the CE,  $F_{\text{CE}}$ , is the maximum isometric (constant length) force,  $F_{\max}$ , multiplied by activation,  $A$ , the force-length,  $f_l(\cdot)$ , and force-velocity,  $f_v(\cdot)$ , relationships of the CE. The activation,  $A$ , is a low-pass filtered version of the stimulation signal muscle  $S(t)$  generated by the muscle reflexes we will detail in the next section. This filter, given by  $A(t) = S - \tau \dot{A}(t)$  with time constant  $\tau$ , represents the diffusion dynamics of calcium ions that activate binding sites in the muscle fibers.

The binding sites are where overlapping actin and myosin filaments attach and generate pulling force. The contractile element length of  $l_{\text{opt}}$  corresponds to maximum overlap between these filaments. Therefore, as the muscle length moves away from  $l_{\text{opt}}$ , its force production capacity decreases leading to the force-length relationship shown in fig. 3.3. We model the force-length relationship via a bell curve

$$f_l(l_{\text{CE}}) = \exp \left( \ln(0.05) \left| \frac{l_{\text{CE}} - l_{\text{opt}}}{w l_{\text{opt}}} \right|^3 \right). \quad (3.6)$$

The velocity-dependent filament attachment probabilities give rise to a force-velocity relationship shown in fig. 3.4. The following expression captures this relationship.

$$f_v(v_{\text{CE}}) = \begin{cases} \frac{v_{\max} - v_{\text{CE}}}{v_{\max} + K v_{\text{CE}}}, & \text{if } v_{\text{CE}} < 0 \\ N + (N-1) \frac{v_{\max} + v_{\text{CE}}}{7.56 K v_{\text{CE}} - v_{\max}}, & \text{if } v_{\text{CE}} \geq 0 \end{cases} \quad (3.7)$$

In this expression,  $K$  is a shape parameter and  $N$  determines the force amplification when the contractile element is lengthening. The force-velocity relationship acts as a multiplicative damper causing the

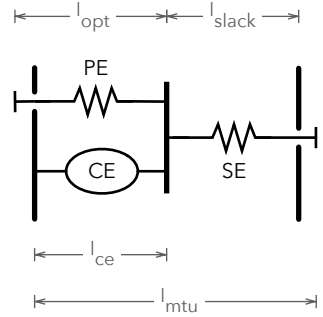


Figure 3.2: Hill-type muscle tendon unit with contractile element (CE), parallel elasticity (PE), and series elasticity (SE).

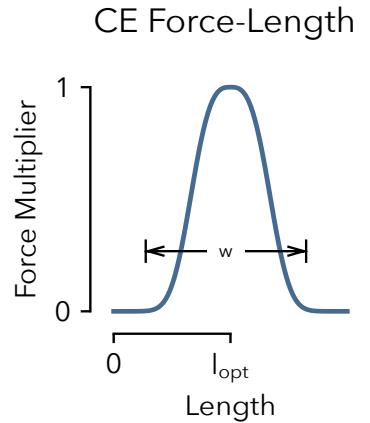


Figure 3.3: Force-length relationship of the CE.

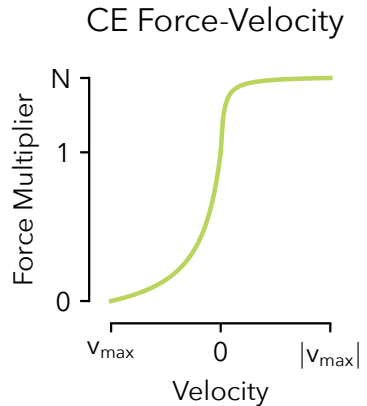


Figure 3.4: Force-velocity relationship of the CE.

Param	Value	Param	Value
$\tau$	0.01 s	$l_{\text{opt}}^{\text{ham}}$	0.10 m
$w$	0.56	$v_{\max}^{\text{ham}}$	-1.2 m/s
$K$	5	$F_{\max}^{\text{ham}}$	3000 N
$N$	1.5	$l_{\text{slack}}^{\text{ham}}$	0.31 m
$\epsilon_{\text{PE}}$	$w$		
$\epsilon_{\text{SE}}$	0.04		

Table 3.3: Neuromuscular parameters for shared entities (left) and the hamstring muscle (right)

CE to produce more contractile force when it is lengthening and less as it contracts.

We model both passive elements, the PE and SE, using the same functional form representing a unidirectional, stiffening spring, the behavior of which is shown in fig. 3.5. The expressions for the elastic force produces by these elements are

$$F_{\text{PE}}(l_{\text{CE}}) = F_{\max} \left( \frac{l_{\text{CE}} - l_{\text{opt}}}{\epsilon_{\text{PE}} l_{\text{opt}}} \right)^2 (l_{\text{CE}} > l_{\text{opt}}) \quad (3.8)$$

$$F_{\text{SE}}(l_{\text{SE}}) = F_{\max} \left( \frac{l_{\text{SE}} - l_{\text{slack}}}{\epsilon_{\text{SE}} l_{\text{slack}}} \right)^2 (l_{\text{SE}} > l_{\text{slack}}). \quad (3.9)$$

The left-hand side of table 3.3 lists the parameters common among all seven muscles of each leg of the neuromuscular model. On the right-hand side of the table, we list four muscle-specific parameters for hamstrings muscle. For a complete list of muscle parameters please refer to Song and Geyer [2015].

The full biped model, shown in fig. 3.6, includes seven Hill-Type muscle-tendon units: soleus, gastrocnemius, tibialis anterior, vastus, hamstring, hip flexors, and gluteus. The length of these MTUs is related to the joint angles according to the variable-length moment arms  $r_{\text{mtu}}^j(\phi^j)$  for each muscle about each joint. For example, the

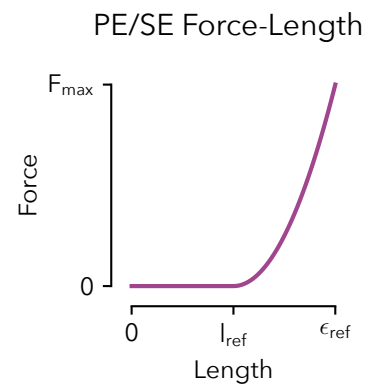


Figure 3.5: PE and SE force length relationship. For the PE,  $l_{\text{ref}} = l_{\text{opt}}$  and  $\epsilon_{\text{ref}} = \epsilon_{\text{PE}}$ . Likewise, for the SE,  $l_{\text{ref}} = l_{\text{slack}}$  and  $\epsilon_{\text{ref}} = \epsilon_{\text{SE}}$ .

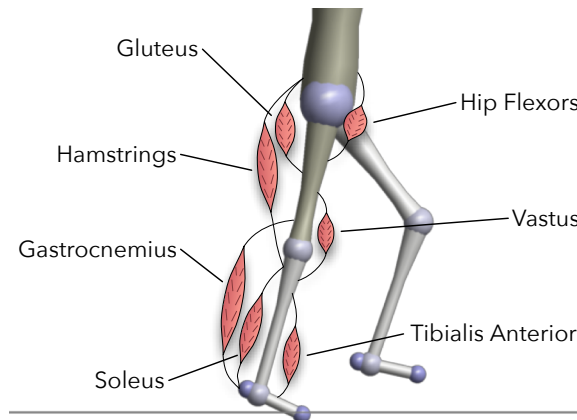


Figure 3.6: Biped walking model with labeled muscles.

length of a biarticular muscle spanning joints  $j$  and  $k$  is

$$l_{\text{mtu}} = l_{\text{opt}} + l_{\text{slack}} + \rho \left( \int_{\phi_0^j}^{\phi^j} r_{\text{mtu}}^j(\phi^j) d\phi^j + \int_{\phi_0^k}^{\phi^k} r_{\text{mtu}}^k(\phi^k) d\phi^k \right). \quad (3.10)$$

Where  $\rho$  is a parameter that approximates the effect of the pennation angle of the muscle fibers and  $\phi_0^j$  and  $\phi_0^k$  are reference joint angles at which the MTU settles to its rest length ( $l_{\text{opt}} + l_{\text{slack}}$ ). The variable length moment arms also govern the torque a muscle produces about a joint according to

$$\tau_{\text{mtu}} = r_{\text{mtu}}^j(\phi^j) F_{\text{mtu}}. \quad (3.11)$$

### 3.3 Stance Reflexes

During stance, hypothesized reflex feedback pathways stimulate the muscles of the leg. In general, a linear feedback law governs the stimulation  $S^m(t)$  of muscle  $m$ ,

$$S^m(t) = S_0^m + \sum_n G_n^m \text{Pro}_n(t - \Delta t_n), \quad (3.12)$$

where  $S_0^m$  is a constant pre-stimulation,  $\text{Pro}_n(t - \Delta t_n)$  is the time-delayed proprioceptive signal from muscle  $n$ , and  $G_n^m$  is the gain on that signal. The proprioceptive signal can take the form of force feedback,  $F_n^m(\cdot)$ , which uses the time delayed tendon force, or length feedback,  $L_n^m(\cdot) = l_n^{\text{CE}}(\cdot) - \text{off } l_n^m$ , which uses the difference between the length of the contractile element of muscle  $n$  and an offset length  $\text{off } l_n^m$ .

The time delay we apply to proprioceptive signals estimate the round-trip neural signal transmission delay of afferent signals from muscle spindles and Golgi tendons to the spine and efferent signals back to the muscles. For ankle muscles, the soleus, tibialis anterior, and gastrocnemius, the time delay is  $\Delta t_n = 20$  ms. For knee muscles, the vastus and hamstrings, it is  $\Delta t_n = 10$  ms. For the hip muscles, the hamstrings, gluteus, and hip flexors, the time delay is  $\Delta t_n = 5$  ms. We will denote time delayed signals using  $t_1 = t - 20$  ms,  $t_m = t - 10$  ms, and  $t_s = t - 5$  ms.

The reflexes encode several key functions of legged locomotion: generating compliant leg behavior, preventing knee overextension, and balancing the trunk. The first function, generating compliant leg behavior, is achieved via positive force feedback on the monoarticular leg extensors: the soleus, vastus, and gluteus. For example, the reflexes stimulate the vastus in part by

$$S^{\text{vas}}(t) = S_0^{\text{vas}} + G_{\text{vas}}^{\text{vas}} F_{\text{vas}}(t_m) + \dots. \quad (3.13)$$

To implement the second function, preventing knee overextension, the reflex control uses two strategies. First, positive force feedback of the biarticular gastrocnemius and hamstrings muscles helps counteract the tendency for knee overextension caused by ankle plantarflexion and hip extension torques respectively. For example, the gastrocnemius has a force feedback reflex,

$$S^{\text{gas}}(t) = S_0^{\text{gas}} + G_{\text{gas}}^{\text{gas}} F_{\text{gas}}(t_l), \quad (3.14)$$

that flexes the knee as it contributes to ankle plantarflexion. The hamstring also has a positive force feed back

$$S^{\text{ham}}(t) = S_0^{\text{ham}} + G_{\text{ham}}^{\text{ham}} F_{\text{ham}}(t_s) + \dots \quad (3.15)$$

that counteracts knee extension caused by hip extension. Also, the hamstring force feedback helps prevent hip flexion caused by heel-strike.

A second mechanism further protects the knee by inhibiting the vastus stimulation in proportion to knee extension beyond a threshold, resulting in the complete vastus stimulation

$$S^{\text{vas}}(t) = S_0^{\text{vas}} + G_{\text{vas}}^{\text{vas}} F_{\text{vas}}(t_m) - G_{\text{knee}}^{\text{vas}} (\phi_{\text{knee}}(t_m) - {}^{\text{off}}\phi_{\text{knee}}) (\phi_{\text{knee}}(t_m) < {}^{\text{off}}\phi_{\text{knee}}) (\dot{\phi}_{\text{knee}}(t_m) < 0) \quad (3.16)$$

where  ${}^{\text{off}}\phi_{\text{knee}}$  is the angle beyond which the vastus is inhibited.

The reflexes achieve the final function of balancing the trunk by proportional-derivative control that produces stimulations for the hip muscles (hip flexors, gluteus, and hamstrings) to stabilize the trunk at a reference lean. Because muscles can only provide pulling force, the proportional derivative control signal is distributed as hip flexor stimulation if the signal represents flexion torque and as simultaneous stimulation for the gluteus and hamstrings if it represents hip extension torque. For example, the complete hamstrings stimulation becomes

$$\begin{aligned} S^{\text{ham}}(t) = & S_0^{\text{ham}} + G_{\text{ham}}^{\text{ham}} F_{\text{ham}}(t_s) \\ & + \left\{ G_p^{\text{ham}}(\phi_{\text{trunk}}(t_s) - \phi_{\text{trunk}}^{\text{ref}}) + G_d^{\text{ham}} \dot{\phi}_{\text{trunk}}(t_s) \right\}_+ \end{aligned} \quad (3.17)$$

where the third term returns the positive reflex contribution from the trunk balance control.

The full set of stance reflexes are:

$$S^{\text{sol}}(t) = S_0^{\text{sol}} + G_{\text{sol}}^{\text{sol}} F_{\text{sol}}(t_1) \quad (3.18)$$

$$S^{\text{ta}}(t) = S_0^{\text{ta}} + G_{\text{ta}}^{\text{ta}} L_{\text{ta}}(t_1) - G_{\text{sol}}^{\text{ta}} F_{\text{sol}}(t_1) \quad (3.19)$$

$$S^{\text{gas}}(t) = S_0^{\text{gas}} + G_{\text{gas}}^{\text{gas}} F_{\text{gas}}(t_1) \quad (3.20)$$

$$S^{\text{vas}}(t) = S_0^{\text{vas}} + G_{\text{vas}}^{\text{vas}} F_{\text{vas}}(t_m) - G_{\text{knee}}^{\text{vas}} (\phi_{\text{knee}}(t_m) - {}^{\text{off}}\phi_{\text{knee}}) (\phi_{\text{knee}}(t_m) < {}^{\text{off}}\phi_{\text{knee}}) (\dot{\phi}_{\text{knee}}(t_m) < 0) \quad (3.21)$$

$$S^{\text{ham}}(t) = S_0^{\text{ham}} + G_{\text{ham}}^{\text{ham}} F_{\text{ham}}(t_s) + \left\{ G_p^{\text{ham}}(\phi_{\text{trunk}} - \phi_{\text{trunk}}^{\text{ref}}) + G_d^{\text{ham}} \dot{\phi}_{\text{trunk}} \right\}_+ \quad (3.22)$$

$$S^{\text{glu}}(t) = S_0^{\text{glu}} + G_{\text{glu}}^{\text{glu}} F_{\text{glu}}(t_s) + \left\{ G_p^{\text{glu}}(\phi_{\text{trunk}} - \phi_{\text{trunk}}^{\text{ref}}) + G_d^{\text{glu}} \dot{\phi}_{\text{trunk}} \right\}_+ \quad (3.23)$$

$$S^{\text{hfl}}(t) = S_0^{\text{hfl}} + \left\{ G_p^{\text{hfl}}(\phi_{\text{trunk}} - \phi_{\text{trunk}}^{\text{ref}}) + G_d^{\text{hfl}} \dot{\phi}_{\text{trunk}} \right\}_- \quad (3.24)$$

### 3.4 Swing Leg Control

During swing, the reflexes shape the natural double pendulum dynamics of the leg in order to achieve sufficient knee flexion, prevent toe scuffing, reach a target landing leg angle, and then extend the leg towards the ground. We here review an idealized control model, proposed in Desai and Geyer [2012], which proposes reflexes that directly apply torques to the hip and knee joints.

The idealized swing control comprises two layers. In the first layer, a leg placement policy,

$$\alpha_{\text{tgt}} = \alpha_0 + c_d d + c_v v, \quad (3.25)$$

prescribes leg angle for the leg to reach by the end of swing. We measure the leg angle between the hip-ankle line and horizontal as shown in fig. 3.7. In eq. (3.25),  $\alpha_{\text{tgt}}$  is the target leg angle,  $\alpha_0$  is the default leg angle,  $d$  is the horizontal distance between the stance leg ankle and the model's center of mass,  $v$  is the velocity of the center of mass, and  $c_d$  and  $c_v$  are constant gain parameters. This policy is taken from Yin et al. [2007] and represents an empirical generalization of the leg placement strategies that recover the linear inverted pendulum model of human walking from disturbances [Kajita et al., 2001, Pratt et al., 2006].

The target angle generated by this policy forms a central input to the second layer comprised of hip and knee controls. The portion of this control that governs the knee action uses a finite state machine to switch between three phases. The first phase allows the knee to passively flex in response to hip moments generated at the onset of swing. If the passive knee flexion is insufficient (the foot swings forward with a tendency to scuff the ground), the control produces active flexion torque of the knee in proportion to the rate  $\dot{\alpha}$

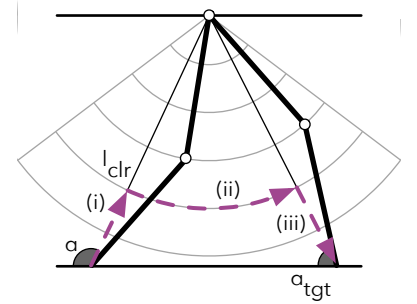


Figure 3.7: The idealized swing leg control guides the leg towards a desired landing leg angle  $\alpha_{\text{tgt}}$  through three phases: (i) Flex the knee until it achieves a clearance leg length  $l_{\text{clr}}$ . (ii) Hold the leg length via knee damping. (iii) Stop and Extend the leg towards the ground when the leg reaches  $\alpha_{\text{tgt}}$ . Figure reproduced from Desai and Geyer [2012].

of forward leg motion,

$$\tau_k^i = \begin{cases} 0, & \dot{\alpha} > 0 \\ -k^i \dot{\alpha}, & \dot{\alpha} \leq 0 \end{cases}, \quad (3.26)$$

where  $k^i$  is the flexion gain and the leg angle  $\alpha$  is defined as the angle between the horizontal and the hip-ankle line.

The second phase activates when the leg length, defined as the distance between the hip and ankle, contracts below a threshold. In this phase, the knee torque is given by

$$\tau_k^{ii} = \begin{cases} -k_1^{ii} \dot{\phi}_k, & \dot{\phi}_k \geq 0 \\ -k_2^{ii} \dot{\phi}_k (\alpha - \alpha_{tgt}) (\dot{\alpha} - \dot{\phi}_k), & \dot{\phi}_k < 0 \text{ \& } \dot{\phi}_k < \dot{\alpha}, \\ 0, & \text{otherwise} \end{cases}, \quad (3.27)$$

where  $k_1^{ii}$  and  $k_2^{ii}$  are damping coefficients. The first case dampens knee flexion, while the second case dampens knee extension, but allows progressively more extension as the leg angle approaches its target. The modulation term ( $\dot{\alpha} - \dot{\phi}_k$ ) prevents premature landing of the leg by damping the knee if it extends faster than the overall leg angle.

The third phase engages when the leg angle gets within a threshold of the target leg angle. The control then applies torque to stop and extend the knee,

$$\tau_k^{iii} = \begin{cases} k^{iii} (\alpha_{thr} - \alpha) \left( 1 - \frac{\dot{\alpha}}{\dot{\alpha}_{max}} \right), & \alpha < \alpha_{thr} \text{ \& } \dot{\alpha} < \dot{\alpha}_{max}, \\ 0, & \text{otherwise} \end{cases}, \quad (3.28)$$

where  $\dot{\alpha}_{max}$  is the maximum leg retraction velocity for which the stopping knee torque is applied. When this torque brings the leg velocity to zero, a knee extension torque is added,

$$\tau_k^{iii'} = \tau_k^{iii} - k^{ext} (l_0 - l), \quad (3.29)$$

where  $l_0$  is the rest leg length,  $l$  is the current leg length, and  $k^{ext}$  is a proportional gain.

The swing leg control also specifies a hip torque in the form of a proportional derivative control on the leg angle,

$$\tau_h^\alpha = k_p (\alpha - \alpha_{tgt}) + k_d \dot{\alpha}. \quad (3.30)$$

This hip torque is supplemented by a feed forward term

$$\tau_h = \tau_h^\alpha - 2\tau_k^{iii} \quad (3.31)$$

that neutralizes the coupling dynamics between the knee and hip during the knee's stop and extend phase (Eq. 3.28).

### 3.5 Control for Simulation Experiments

In chapter 4, in order to assess potential benefits of using the neuromuscular model for prosthesis control, we perform simulated experiments of an amputee walking with a powered knee and ankle prosthesis. In those experiments, to generate the reference torques for the SEAs, we use a hybrid neuromuscular control that blends the muscle based stance-control (section 3.3) with the idealized swing leg placement control section 3.4.

For the stance control of the prosthesis, we utilize only muscles and reflexes of the lower leg: the Hamstring, Vastus, Gastrocnemius, Soleus, and Tibialis Anterior. These muscles are stimulated by eqs. (3.18) to (3.22). However, because the hamstring muscle spans the hip joint as well, and we do not wish to instrument the torso of the amputee user, we assume that the torso angle remains fixed at  $\phi_{ref}$ , thereby reducing the hamstring stimulation to eq. (3.15).

Additionally, we make two modifications to the prosthesis-side swing leg control. First, on the prosthesis-side hip we remove the feed-forward term that neutralizes the disturbance created by the knee's stop and extend phase (eq. (3.31)), requiring that feedback control deal with this torque. Second, we do not use the adaptive leg placement policy of the swing control (eq. (3.25)) as the prosthesis does not have access to information about the amputee's center of mass and stance leg ankle position. Instead the prosthesis swing leg control employs a constant target leg angle,  $\alpha_{tgt} = const$ .

The torques produced by the swing controller augment the net torques produced by the Hill-type muscles and reflexes during stance. At heel strike, the control policy switches from using the swing leg control torques to the stance torques generated by the muscle models. In late stance, the policy mixes the torques specified by the stance and swing controllers by scaling the stance and swing torques and muscle stimulations in proportion to the normalized ground reaction force,

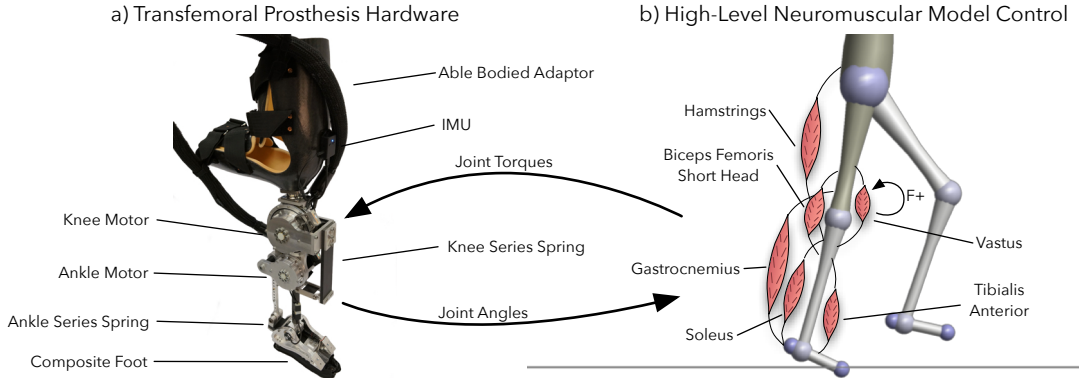
$$\tau_{late\ stance} = \tau_{stance}(GRF) + \tau_{swing}(1 - GRF), \quad (3.32)$$

$$S^m_{late\ stance} = S^m(GRF). \quad (3.33)$$

During swing, only the swing leg torques are used.

### 3.6 Control for Prosthesis Experiments

In chapters 5, 6, and 8 we perform experiments with the prosthesis hardware (detailed in chapter 2) with the neuromuscular model control. To operate this control on the prosthesis, we measure the prosthesis' joint angles using its onboard encoders, the user's thigh



angle using an inertial measurement unit, and ground reaction signals via hall effect sensors embedded in the foot. The measured joint angles feed into the muscle and reflex models in order to calculate the desired joint torques for the prosthesis, which are then achieved by the low-level SEA control (section 2.2). We use the ground reaction forces in

In chapters 6 and 8, the stance control follows the equations given in section 3.3 with the same modifications to the Hamstring as were made for the simulated experiments ( $\phi_{\text{hip}} = \phi_{\text{ref}}$ ). In chapter 5 we experiment with an augmented version of the model that contains a Biceps Femoris Short Head, a monoarticular knee flexor (see fig. 3.8). This muscle helps prevent knee over extension via length feedback of the form

$$S^{\text{bfsh}}(t) = S_0^{\text{bfsh}} + G_{\text{bfsh}}^{\text{bfsh}} L_{\text{bfsh}}(t_1). \quad (3.34)$$

In this model, knee over extension is further prevented by inhibiting the vastus in proportion to the BFsh length. Consequently, the vastus stimulation becomes

$$S^{\text{vas}}(t) = S_0^{\text{vas}} + G_{\text{vas}}^{\text{vas}} F_{\text{vas}}(t_m) - G_{\text{vas}}^{\text{bfsh}} L_{\text{bfsh}}(t_m). \quad (3.35)$$

The properties of BFsh muscle (as well the properties of the other muscles) are based on human physiological parameters described in Song and Geyer [2015].

While our simulated experiments used the idealized reflexive swing control described in section 3.4, in our prosthesis experiments we instead use the minimum-jerk trajectory swing controller proposed by Lenzi et al. [2014], which automatically adapts to walking speed and produces human-like trajectories. In this method, at every toeoff the control method generates a pair of minimum jerk trajectories for each joint: one that starts at the toeoff angle, velocity and acceleration and reaches peak knee flexion or ankle dorsiflexion and another that goes from the peak flexion state to the heel strike state.

Figure 3.8: (a) Custom transfemoral prosthesis with series elastic actuators. In experiments in this thesis, we use an adaptor to test the prosthesis with able-bodied subjects. (b) During stance, we propose a control based on a neuromuscular model of human physiology that generates joint torques through virtual muscles that are stimulated by hypothesized local reflex pathways.

The knee and ankle joints are set to 65 and 2 deg at peak flexion and 2 and -5 deg at heel strike respectively. The prosthesis then follows these desired joint angles via proportional/derivative feedback plus a model-based feedforward term. Combined, the feedback and feedforward terms specify the desired joint torques which the low-level SEA control tries to achieve (section 2.2). The use of the feed forward term and SEA torque control during swing allows the system to maintain a level of impact compliance despite following a trajectory.

The swing phase duration is set to 60% of the previous stance phase duration. In the chapters 5 and 6, we specified that the peak flexion angles for both the knee and ankle would be achieved simultaneously at 25% of swing. Later, in the work presented chapters 7 and 8, we delayed peak ankle flexion to 50% of swing to help avoid some of the frequent trips during swing that we discovered during the experiment presented in chapter 6. Chapter 7 also presents a more principled approach to avoiding these swing trips that explicitly predicts and plans to avoid premature foot contact with the ground.

We switched to this trajectory following swing control approach for two reasons: First, preliminary experiments with the idealized swing control on the prosthesis hardware revealed that it was more sensitive to errors in the torque control. This seemed especially true in the second phase of the control, in which small damping torques are used to control the rate of extension of the knee. In our SEA design (section 2.1), small errors in the torque measurement can build up over time due to encoder shift and thermal expansion. While these torque errors are insignificant during stance, they appeared to cause marked differences in the behavior of idealized swing control. In contrast, a trajectory based approach can compensate for these errors through its explicit position feedback. Second, in our simulated experiments, we held the target angle constant. However, in a real system, the target angle prediction should adapt to specific users and to variations in speed, terrain, and balance recovery intent. How best to predict this target angle remains an open research question and is not addressed in this thesis.

To switch between stance and swing phases, the prosthesis follows the state machine depicted in fig. 3.9. Transitions to stance occur when the leg is ahead of the frontal plane (leg angle  $\alpha > 90^\circ$ , see fig. 3.7) and when the ground reaction force (GRF) exceeds a hand-tuned threshold. Transitions to swing are allowed when the GRF falls below a threshold, the foot is behind the frontal plane ( $\alpha < 90^\circ$ ), and the hip is flexing. For the experiments described in chapters 5 to 7 we use the prosthesis' built-in GRF sensors detailed in section 2.1.3. In later work (chapter 8), involving stepping on objects, we use the GRF readings from an instrumented treadmill, as they proved more

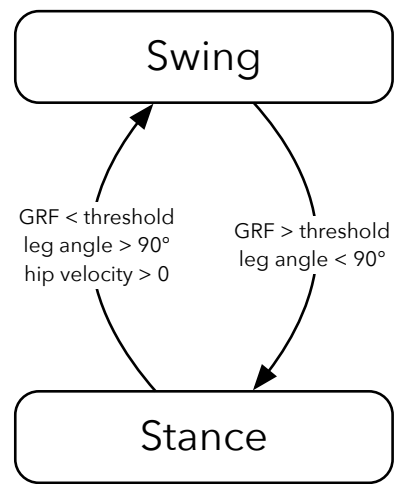


Figure 3.9: Universal stance/swing state machine utilized for all hardware experiments.

reliable in this disturbed case.

# 4

## *Simultated Comparison of Neuromuscular and Impedance Controllers*

*Material in this section based partially on Thatte and Geyer [2016]<sup>1</sup> and Thatte and Geyer [2014]<sup>2</sup>*

To evaluate the potential of neuromuscular prosthesis control to improve amputee gait robustness, we construct a simulation of an amputee walking on a powered prosthesis and perform optimizations to identify parameters that lead to robust locomotion over rough terrain. We then compare the performance of the proposed control to that of impedance control and find that the proposed control improves robustness to elevation changes and unexpected deviations from nominal walking, suggesting that it may help amputees prevent trips and falls (fig. 4.1).

### *4.1 Methods*

#### *4.1.1 Simulation Environment*

We study the performance of the proposed transfemoral prosthesis controller in a simulation model of a unilateral amputee equipped with the proposed powered prosthesis. To more accurately model an amputee's anatomy, we sever the femur of the unimpaired human model 11 cm above the knee and attach the hamstring muscle to the distal end of the shortened bone as recommended in Brown et al. [2012]. This change converts the biarticular hamstring into a monoarticular muscle that only extends the hip. Next, we attach a model of the full prosthesis to the severed femur. The prosthesis modeled in this study is an earlier version of the prosthesis design presented in chapter 2, which uses the knee actuator design for both the knee and ankle joints. Our simulation of the prosthesis models the series elasticity, electrical dynamics, gear ratios, and resultant

<sup>1</sup> Nitish Thatte and Hartmut Geyer. Toward balance recovery with leg prostheses using neuromuscular model control. *IEEE Transactions on Biomedical Engineering*, 63(5):904–913, 2016

<sup>2</sup> Nitish Thatte and Hartmut Geyer. Towards local reflexive control of a powered transfemoral prosthesis for robust amputee push and trip recovery. In *2014 IEEE/RSJ International Conference on Intelligent Robots and Systems*, pages 2069–2074. IEEE, 2014

reflected inertias of the actuators, and assumes a low-level current-based SEA control achieves desired torques [Pratt and Williamson, 1995].

To compare the performance of the proposed control, we also simulate the commonly-used impedance control method, described in detail in ??, at the behavior level. Specifically, we implement the impedance control presented in Sup et al. [2008] as it tended to perform better than other versions in our simulations. This control partitions the gait cycle into four phases. In each phase  $i$ , the torque of an actuated joint is governed by an impedance function

$$\tau_i = -k_{1,i}(\theta - \theta_{1,i}) - k_{2,i}(\theta - \theta_{2,i})^3 - b_i\dot{\theta}, \quad (4.1)$$

where  $\theta$  is the joint angle,  $\theta_{1,i}$  and  $\theta_{2,i}$  are angle offsets, and  $k_{1,i}$ ,  $k_{2,i}$  and  $b_i$  are the impedance parameters.

[check reference](#)

#### 4.1.2 Controller Optimization for Natural and Robust Walking

For both the hybrid neuromuscular controller and the impedance controller, we use optimization to search for gaits that appear natural and are robust to disturbances. For the hybrid neuromuscular model, we optimize 53 parameters that include reflex feedback gains and swing leg control parameters for both the amputee and prosthesis as well as the SEA control gains. To reduce the number of parameters to optimize, we use fixed values for many parameters, such as the muscle properties and prestimulations. For the impedance controller, we optimize 59 parameters that include the reflex feedback gains and the swing leg control parameters for the amputee model, and the impedance parameters and SEA controller gains for the prosthesis. Again to reduce the number of parameters to optimize, the impedance parameters that are set to zero according to Sup et al. [2008] are fixed to zero during the optimization.

We rely on the covariance matrix adaptation evolution strategy (CMA-ES) [Hansen, 2006] and perform optimization in two steps. In the first step, we search for control parameters that generate a gait with natural kinematics and kinetics. To this end, we take advantage of the observation that human gait seems to result from minimizing metabolic energy consumption [McNeill Alexander, 2002], and use the cost of transport

$$Cost = \frac{W}{mgx} + \frac{1}{mgx} \int (c_1 \tau_{cmd}^2 + c_2 \tau_{limit}^2) dt \quad (4.2)$$

as optimization criterion. In the cost,  $W$  accounts for the energy consumption of both the modeled amputee's muscles and the prosthesis' virtual muscles according to Umberger et al. [2003],  $\tau_{cmd}$  is the sum

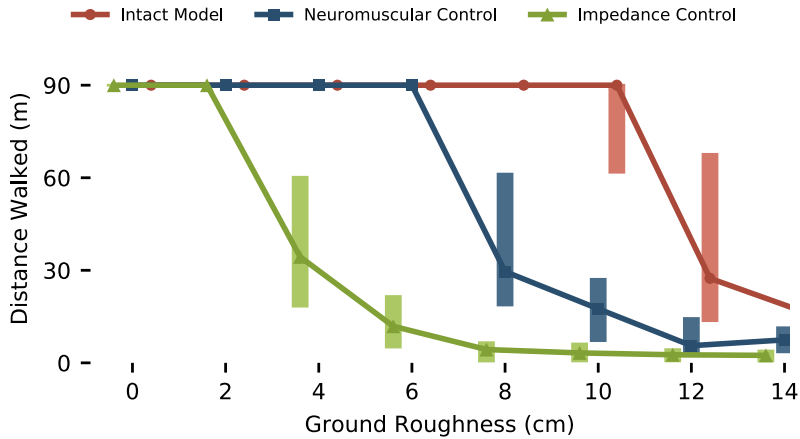


Figure 4.1: Control performance of simulated prosthesis on rough terrain. The distances walked over terrains with different ground roughness are compared between the amputee model using a powered knee-ankle prosthesis with impedance control (green) and hybrid neuromuscular control (blue) as well as with the unimpaired human model (red). Shown are the median and range (25<sup>th</sup> and 75<sup>th</sup> percentiles) of the covered distances for 50 terrains sampled at each roughness level.

of the torques commanded by the neuromuscular swing control or the impedance control,  $\tau_{\text{limit}}$  is the sum of torques produced by the model's mechanical hardstops, which prevent knee and ankle hyperextension,  $m$  is the mass of the amputee,  $g$  is the gravitational acceleration, and  $x$  is the distance travelled in 20 seconds. The hand tuned constants,  $c_1 = 0.1$  and  $c_2 = 0.01$ , ensure that the terms of the cost function have similar order-of-magnitude.

We run the above optimization for 300 iterations, and use the best resulting set of control parameters to seed an optimization for robustness to unexpected changes in ground height. For this second step, the cost function becomes

$$\text{Cost} = -x + c_3 \int \tau_{\text{limit}}^2 dt, \quad (4.3)$$

rewarding the distance travelled and penalizing joint hyperextension ( $c_3 = 0.0005$ ). Instead of level ground, the simulations evaluating the cost are performed on terrain that is flat for the first 10 meters (to allow the model to reach steady walking) and then features steps, spaced one meter apart and drawn from a uniform random distribution. The width of the distribution grows at a rate of 2.5 cm per meter distance travelled, resulting in steps that grow progressively rougher the farther the model walks. To avoid overfitting, the evaluation is performed on five different terrains, resulting in an average cost. Like in the first step, the optimization is stopped after 300 iterations, resulting in the final, best set of control parameters.

## 4.2 Results

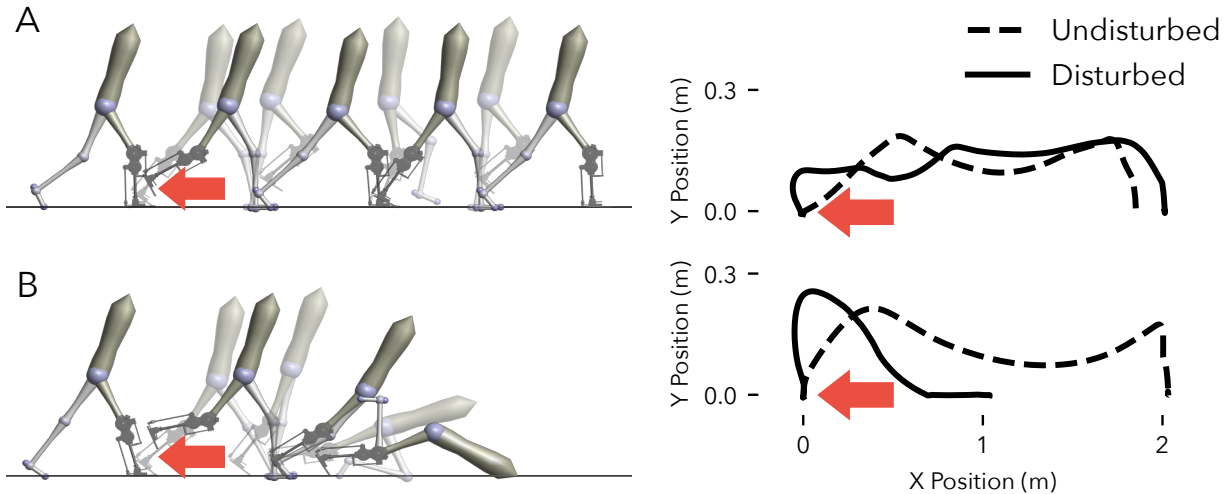
We evaluate the performance of the proposed control and of impedance control by subjecting the amputee model to terrains that are flat for 10 meters and then feature steps drawn from uniform distributions for another 90 meters. The widths of the distributions are constant but vary among the terrains to test the control performance on steps of increasing steepness (0 cm to  $\pm 14$  cm, 2 cm increments, total of 8 terrains).

Figure 4.1 shows the distances the amputee model walks over 50 trials at each roughness level (proposed neuromuscular control in blue, impedance control in green). Most of the trials with the impedance-controlled prosthesis cover the full distance up to a roughness of 2 cm. At a roughness of 4 cm, however, the median distance drops to 34 m, which further declines as the roughness increases. In contrast, the prosthesis using the neuromuscular control, allows the amputee model to walk the full distance up to a roughness of 6 cm. Moreover, neuromuscular control has a similar distribution of distances walked at a roughness of 8 cm as impedance control has at a roughness of 4 cm.

Although the prosthesis using neuromuscular control significantly improves the robustness of the amputee model on rough terrain, the performance trails by a large margin that of an unimpaired model (fig. 4.1, red line), for which most of the trials covered the full distance up to a roughness of 10 cm. Limiting the swing leg placement targets in the neuromuscular prosthesis control to constant angles may account for some of this performance gap. In future work, we may overcome this limitation by estimating the amputee's center of mass velocity and stance ankle position so that the prosthesis control can take advantage of the full leg placement policy (eq. (3.25)). Other sources for the performance gap could stem from differences in the inertial properties between the prosthesis and the healthy leg, delay and inaccuracy in the series elastic actuator torque tracking, and the increased number of parameters in the asymmetric amputee model, which can reduce the quality of the optimized solutions.

A possible explanation for why the neuromuscular control produces more robust behavior than impedance control is the former's attempt to mimic the underlying dynamics and goals of human motor control rather than to track impedance behavior about a predefined motion for each individual joint. To illustrate this difference, we subject the amputee model with both control strategies to a simulated trip in the form of a  $15 \text{ N} \cdot \text{s}$  impulse applied at 5% of the undisturbed swing duration.

Figure 4.2A shows the toe trajectory of the prosthesis using neu-



romuscular control both in the undisturbed and disturbed cases. While the impulse causes a large deviation from the nominal trajectory in early swing, the controller quickly recovers. From mid-swing onward, the foot follows a qualitatively similar path, maintains adequate ground clearance, and successfully reaches a similar foot placement as in the undisturbed case. In contrast, the prosthesis with impedance control does not respond adequately when subjected to the disturbance (fig. 4.2B). This is illustrated by the prosthesis behavior in mid swing, during which it does not react appropriately to maintain ground clearance of the toe. Rather, the joint-based impedance functions drive the knee into extension prematurely, and the prosthetic foot scuffs the ground resulting in a trip and subsequent fall.

#### 4.2.1 Discussion

Our simulation results suggest that the hybrid neuromuscular control policy may be able to improve amputee gait stability over existing impedance control methods. An amputee model walking with a powered prosthesis showed substantial improvements in balance recovery on rough ground and after swing leg trips when using the hybrid neuromuscular control policy as opposed to impedance control. One possible reason for the improvement is that the proposed controller considers global leg information such as the target leg angle (eqs. (3.26) to (3.28)), and it is well known that without placing the feet into proper target points on the ground, legged systems fail to balance [Townsend, 1985, Raibert, 1986, Kajita et al., 2001, Seyfarth

Figure 4.2: Tripping response of the amputee model with neuromuscular (A) and impedance control (B) of the prosthesis. Shown are the prosthetic toe trajectories during undisturbed gait (dashed line) and when disturbed by a  $15 \text{ N} \cdot \text{s}$  impulse (solid line). The neuromuscular controller effectively responds to the disturbance and maintains a qualitatively similar toe trajectory. The impedance controller leads to foot scuffing and an eventual fall.

et al., 2002, Pratt et al., 2006, Wu and Geyer, 2013]. A second reason could be that the design of the swing leg control policy explicitly accounts for large disturbances to the lower limb dynamics in order to achieve desired leg placements [Desai and Geyer, 2012]. Finally, the implemented impedance control strategy relies on reliable estimation of the discrete phase of gait during stance so that it can apply the appropriate impedance control parameters. In the presence of disturbances such as the ground height disturbances we studied here, this phase estimate may be incorrect, thus causing the impedance control to apply inappropriate torques.

These results capture only a small portion of the balance disturbances that humans typically encounter [Robinovitch et al., 2013]. Other disturbances may evoke amputee responses that the simulation model does not capture; especially since it is driven solely by a reflexive walking controller that ignores conscious interventions. Therefore, in future chapters of this thesis, we build towards and present results wherin we implement prosthesis controllers on real hardware being used by actual humans in order to more decisively compare control strategies.

# 5

## *Preference Based Optimization*

*Material in this section based on Thatte et al. [2017]<sup>1</sup> and Thatte et al. [2018]<sup>2</sup>*

As discussed in ?? previous work has explored learning from qualitative feedback such as preferences in order to circumvent defining objective functions and using Bayesian optimization in order to reduce the number of experiments required to optimize a system. In this section, we present a new optimization algorithm, Predictive Entropy Search with Preferences (PES-P), that combines these two ideas. The algorithm uses preference queries between pairs of control parameters to avoid the a priori definition of features and to consider unquantifiable qualities of the desired behavior. The algorithm further incorporates black-box Bayesian optimization to ensure its preference queries gather information efficiently without relying on a system model.

In developing the algorithm, we make three main contributions. First, we adapt an acquisition function previously proposed for interval scale feedback to the preference feedback case. This acquisition function seeks a pair of parameters for which a preference will maximally reduce the entropy of the distribution of objective function optima. Second, we compare in simulation the performance of the proposed optimization method against the expected improvement method (EI) and uniform random sampling via Latin hypercubes (LH) for two classes of examples: optimizing randomly generated objective functions and tuning the control parameters of simulated dynamical systems. Finally, we compare the performance of the three methods for the task of optimizing the control parameters of a robotic prosthesis given real user feedback.

<sup>1</sup> Nitish Thatte, Helei Duan, and Hartmut Geyer. A sample-efficient black-box optimizer to train policies for human-in-the-loop systems with user preferences. *IEEE Robotics and Automation Letters*, 2017

<sup>2</sup> Nitish Thatte, Helei Duan, and Hartmut Geyer. A method for online optimization of lower limb assistive devices with high dimensional parameter spaces. In *Robotics and Automation (ICRA), 2018 IEEE International Conference on*. IEEE, 2018

[check reference](#)

## 5.1 Bayesian Approach Preliminaries

### 5.1.1 Learning from Preferences

To learn latent objective functions from preferences, we rely on the method developed by Chu and Ghahramani [Chu and Ghahramani, 2005], briefly reviewed here. The method considers a training dataset  $D_n$  of  $n$  preferences between pairs of points,  $\{x_1^a \succ x_1^b, \dots, x_k^a \succ x_k^b, \dots, x_n^a \succ x_n^b\}$ . These points can, for instance, represent control policy parameters. From the dataset, the method finds a posterior distribution of latent objective functions  $f$ ,

$$P(f|D_n) = \frac{P(D_n|f) P(f)}{P(D_n)}. \quad (5.1)$$

where  $f = [f(x_1^a), f(x_1^b), \dots, f(x_n^a), f(x_n^b)]^T$ . First, the method assumes that the prior distribution of objective functions is a zero-mean Gaussian process (GP),  $P(f) = \mathcal{N}(0, \Sigma)$ . An appropriate kernel,  $\Sigma_{i,j} = k((x_i, x_j))$ , describes the elements of the covariance matrix  $\Sigma$ . (See [Williams and Rasmussen, 2006] for a full description of GPs.) Second,  $P(D_n|f)$  is the overall likelihood of preferences in the dataset given specific reward function values and is modeled as the product of the likelihood of each independent preference in the dataset,

$$P(D_n|f) = \prod_{k=1}^n P(x_k^a \succ x_k^b | f(x_k^a), f(x_k^b)) = \prod_{k=1}^n \Phi(q_k), \quad (5.2)$$

where  $P(x_k^a \succ x_k^b | f(x_k^a), f(x_k^b))$  is the probability of a preference if Gaussian noise with variance  $\sigma^2$  corrupts the function values,  $\Phi(\cdot)$  is the cumulative distribution function of a normal distribution, and  $q_k = \frac{f(x_k^a) - f(x_k^b)}{\sqrt{2}\sigma}$ . In essence, the likelihood model increases the certainty of a preference between  $x_k^a$  and  $x_k^b$  as the difference between  $f(x_k^a)$  and  $f(x_k^b)$  widens.

To obtain the posterior distribution  $P(f|D_n)$  the method approximates eq. (5.1) with a Gaussian distribution. As a result, the predictive distribution (subscript p) of the objective function at test points,  $f_t$ , is also Gaussian,  $P(f_t|D_n) = \mathcal{N}(\mu_p, \Sigma_p)$ . Finally, the predictive distribution of a preference between two points  $x^a$  and  $x^b$  is

$$P(x^a \succ x^b | D_n) = \int P(x^a \succ x^b | f_t, D_n) P(f_t|D_n) df_t \quad (5.3)$$

$$= \Phi\left(\frac{\mu^a - \mu^b}{\sigma_p}\right), \quad (5.4)$$

$$\sigma_p^2 = 2\sigma^2 + \Sigma_p^{aa} + \Sigma_p^{bb} - \Sigma_p^{ab} - \Sigma_p^{ba}. \quad (5.5)$$

Figure 5.1a provides an example of how the method estimates a ground-truth objective function shown in purple. The blue line and

shaded area show the mean and standard deviation of the posterior distribution of objective functions,  $P(f_t|D_n)$ , after two preference queries between pairs of parameters (orange, higher is preferred over lower value). The queries have the effect of lifting the estimated objective function close to preferred points and pushing it down close to unpreferred points, approximating the true objective function over time.

### 5.1.2 Active Learning for Optimization

Learning from preferences describes how to find a distribution of objective functions given a dataset of comparisons. The question now becomes how to efficiently solicit preferences from the user. As our main goal is to find the optimal parameters  $x^*$ , we should forgo modeling the objective function accurately in all parameter regions and instead focus on regions where the objective might be high. Bayesian optimization addresses this problem with an acquisition function that helps to efficiently sample training data.

One such acquisition function is the expected improvement, which has been used both in the context of preference feedback [Brochu et al., 2008] and interval scale feedback [Jones et al., 1998],

$$EI(x) = (\mu^* - \mu(x))\Phi(d) + s(x)\phi(d), \quad (5.6)$$

where  $d = (\mu^* - \mu(x))/s(x)$ ,  $\mu^*$  is the mean of the current estimate of the optimum, and  $\mu(x)$  and  $s(x)$  are the mean and standard deviation of the objective of a new point  $x$ , respectively. As an alternative, for interval scale feedback, [Hennig and Schuler, 2012] and [Hernández-Lobato et al., 2014] proposed acquisition functions that seek to reduce the uncertainty in the distribution of objective function optima, measured in terms of the differential entropy. For example, the Predictive Entropy Search acquisition function [Hernández-Lobato et al., 2014] seeks a point  $x$  that is expected to reduce the entropy of the distribution of optima  $x^*$  after observing its value  $y$ ,

$$\alpha_n(x) = H[P(x^*|D_n)] - E_{P(y|x,D_n)}[H[P(x^*|y,x,D_n)]], \quad (5.7)$$

where  $H[P(x)] = - \int P(x) \log P(x) dx$  is the differential entropy. The authors of these methods have shown they can outperform EI.

## 5.2 Bayesian Approach Methods

Our goal is to simultaneously address both the difficulty of defining objective functions when an expert cannot demonstrate the desired robot behavior and the expense of running experiments on hardware.

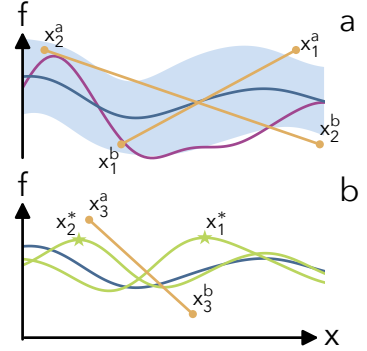


Figure 5.1: Learning from preferences. (a) Mean and standard deviation of  $P(f_t|D_n)$  (blue) after two preferences queries (orange) from the true objective function (purple). (b) Mean of  $P(f_t|D_n)$  (blue) and means of  $P(f_t|D_n, x_m^*)$  (green) for two samples of  $x_m^*$ . PES-P queries a new comparison (orange) for which the preference is currently uncertain, but on average is certain after conditioning on all  $x_m^*$ .

To this end, we adapt the Predictive Entropy Search acquisition function (eq. (5.7)) to the preference learning case.

### 5.2.1 Acquisition Function

To obtain the optimal parameters  $x^*$  with the smallest number of preference queries, we solicit preferences that maximize the expected information gain about the distribution of objective function optima  $P(x^*|D_n)$ . Adapting eq. (5.7) to preference feedback yields

$$\alpha_n(x^a, x^b) = H[P(x^*|D_n)] - E_{P(y|x^a, x^b, D_n)} \left[ H \left[ P \left( x^* | y, x^a, x^b, D_n \right) \right] \right], \quad (5.8)$$

where  $y$  is a binary random variable that represents the preference between  $x^a$  and  $x^b$ . The first term in this function is the current entropy of objective function optima and the second term is the entropy of optima after observing the preference  $y$ . As we have not yet observed the preference, we take the second term in expectation over the two possible preference outcomes.

As discussed in [Hernández-Lobato et al., 2014], this acquisition function is intractable to compute. However, following the approach used for the original PES algorithm, we can rewrite eq. (5.8) in terms of the entropies of the predictive distribution of the preference between  $x^a$  and  $x^b$ ,

$$\alpha_n(x^a, x^b) = H \left[ P \left( y | x^a, x^b, D_n \right) \right] - E_{P(x^*|D_n)} \left[ H \left[ P \left( y | x^*, x^a, x^b, D_n \right) \right] \right] \quad (5.9)$$

$$\approx H \left[ P \left( y | x^a, x^b, D_n \right) \right] - \frac{1}{M} \sum_{x_m^* \sim P(x_m^*|D_n)}^M H \left[ P \left( y | x_m^*, x^a, x^b, D_n \right) \right]. \quad (5.10)$$

This reformulation significantly improves computability. First, the new acquisition function uses the entropies of probabilities of preferences, given by eq. (5.4). Second, we now take the expectation over  $P(x^*|D_n)$ , which we can perform by sampling  $M$  functions from  $P(f_t|D_n)$  and optimizing each one to get  $M$  samples of  $x^*$  (see Appendix for details). Finally, the second term no longer requires conditioning the GP on every pair of  $x^a$  and  $x^b$  considered during optimization of the acquisition function. Instead, we only have to condition the Gaussian process  $M$  times on  $(x_m^*, D_n)$ .

For the experiments in section 5.3 we choose  $M = 12$ , which allows us to construct and optimize  $\alpha_n(x^a, x^b)$  in about five seconds, which is fast enough for our prosthesis application. Although 12 samples of  $x^*$  is not enough to compute an accurate expectation over  $P(x^*|D_n)$ , interpreting the algorithm as an example of active learning by disagreement may explain why it still works well. As

shown in fig. 5.1b, optimizing the acquisition function chooses a pair  $x^a$  and  $x^b$  for which the preference is currently uncertain, but certain on average after conditioning on all  $x_m^*$ . The sampled  $x_m^*$  do not necessarily agree on which point is preferred; hence, after observing the preference, the algorithm can rule out  $x_m^*$  that made the model certain but wrong about the preference. This intuition is similar to that provided by [Houlsby et al., 2012] for Bayesian active learning by disagreement for GP classifiers.

### 5.2.2 Conditioning the Gaussian Process on $x^*$

The second term on the right side of eq. (5.10) requires us to compute the distribution of the preference given the location of the optimum,

$$P(y|x_m^*, x^a, x^b, D_n) = \int P(x^a \succ x^b | f_t, x_m^*, D_n) P(f_t|x_m^*, D_n) df_t. \quad (5.11)$$

It is not directly feasible to condition the predictive distribution on  $x^*$ , so instead we turn to approximating this condition with three constraints (see appendix for details):

C1: First we impose that  $x^*$  is a local maximum by ensuring that the gradient of  $f(x^*)$  is zero and its Hessian is negative definite. We further simplify the Hessian constraint to only require that the Hessian's off-diagonal elements are zero and its diagonal elements are less than zero. We implement the gradient and off-diagonal constraints by conditioning the prior,  $P(f)$ , on derivative observations as outlined in [Solak et al., 2003]. To constrain the diagonal elements of the Hessian, we amend the likelihood term in eq. (5.1) by adding terms that penalize Hessians with positive diagonal elements.

C2: Second, we try to ensure that  $x^*$  is also a global maximum by enforcing that  $f(x^*)$  is greater than the function values of all training points sampled so far. We impose this constraint by adding more preference relations into the likelihood term in eq. (5.1) between  $x^*$  and all training points.

C3: Finally, to further ensure that  $f(x^*)$  is a global maximum, we require that it is also larger than the function values of the two new test points,  $f(x^a)$  and  $f(x^b)$ . Whereas C2 ensures  $f(x^*)$  exceeds function values in areas explored so far, C3 ensures that  $f(x^*)$  also exceeds function values in unexplored regions. We approximate this constraint analytically by conditioning on the single constraint  $f(x^*) > (f(x^a) + f(x^b))/2$  using the method detailed in [Xu and Li, 2010].

---

Algorithm 1: Predictive Entropy Search with Preferences

```

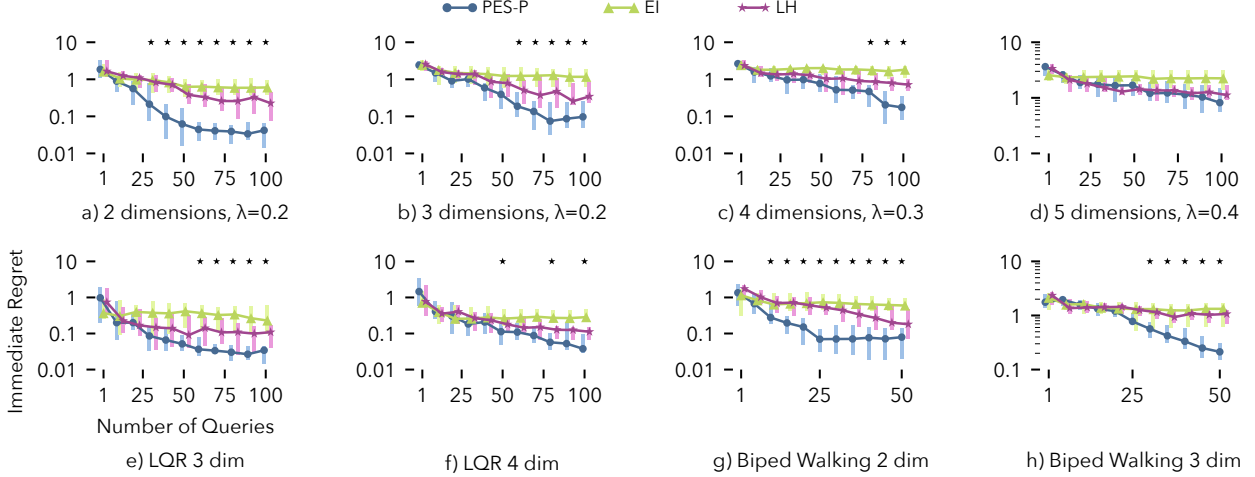
1: procedure PES-P
2:    $D_n = \emptyset$ 
3:   for  $n \leftarrow 0$  to  $N - 1$  do                                 $\triangleright N$  iterations
4:      $F \leftarrow \{f_m \sim P(f_t|D_n) | m \in [1, M]\}$ 
5:      $X^* \leftarrow \{\arg \max_x (f_m) | f_m \in F\}$ 
6:      $(x_{n+1}^a, x_{n+1}^b) \leftarrow \arg \max_{(x^a, x^b)} ff_n(x^a, x^b; X^*)$ 
7:      $y_{n+1} \leftarrow \text{QUERYUSERPREF}(x_{n+1}^a, x_{n+1}^b)$ 
8:      $D_{n+1} \leftarrow D_n \cup (x_{n+1}^a, x_{n+1}^b, y_{n+1})$ 
9:   end for
10:  return  $x^* \leftarrow \arg \max_x \text{mode}(P(f_t(x)|D_N))$ 
11: end procedure

12: function  $\alpha_n(x^a, x^b; X^*)$                        $\triangleright$  acquisition function
13:    $h \leftarrow \left\{ H \left[ P(y|x^a, x^b, D_n, C1, C2, C3) \right] | x_m^* \in X^* \right\}$ 
14:   return  $H \left[ P(y|x^a, x^b, D_n) \right] - \text{mean}(h)$ 
15: end function
```

---

### 5.2.3 Algorithm Summary

With constraints C<sub>1</sub> to C<sub>3</sub>, at each iteration we can efficiently compute the acquisition function, eq. (5.10). We summarize the resulting Predictive Entropy Search with Preferences (PES-P) algorithm as follows (algorithm 1): At each iteration  $n$ , first, the algorithm samples  $M$  objective functions from the current distribution,  $P(f_t|D_n)$ , and optimizes each one to generate  $M$  samples of  $x^*$  (lines 4 and 5). Next, using the set of sampled optima  $X^*$ , we maximize the acquisition function to obtain the next two points to present to the user  $x_{n+1}^a$  and  $x_{n+1}^b$  (lines 6 and 12–15). Note: we can precompute the effect of C<sub>1</sub> and C<sub>2</sub> before evaluating  $ff_n(x^a, x^b)$  as these two constraints do not depend on  $x_{n+1}^a$  and  $x_{n+1}^b$ . On the other hand, C<sub>3</sub> depends directly on  $x_{n+1}^a$  and  $x_{n+1}^b$  and therefore is computed within the acquisition function for every pair of points considered during the optimization of  $ff_n(x^a, x^b)$ . We then query the user to obtain their preference  $y_{n+1}$  between these two points and add it to the dataset of preferences (lines 7 and 8). Finally, at the end of the  $N$  iterations of the algorithm, we return the optimum  $x^*$  of the most likely function,  $\text{mode}(P(f_t(x)|D_N))$ , which is equal to the posterior mean function in the Gaussian process case (line 10). While it may be more correct to return  $\text{mode}(P(x^*|D_N))$ , we do not do this as the PES algorithm seeks to avoid approximating this distribution.



### 5.3 Bayesian Approach Results

We test the ability of PES-P to solve optimization problems in four cases with increasing realism from the optimization of randomly generated objective functions drawn from a GP, to the tuning of feedback gains of random linear systems and a neuromuscular walking model, to the optimization of control parameters for a powered transfemoral prosthesis given real user feedback. In all four cases, we compare the performance of the proposed algorithm to the expected improvement criterion (EI) (eq. (5.6)) and random sampling via Latin hypercubes (LH)<sup>3</sup> [McKay et al., 2000]. For the three simulated cases, we show results over 20 trials and measure performance in terms of the immediate regret, defined as  $IR = |f(\tilde{x}_n^*) - f(x^*)|$ , versus the number iterations. Here,  $f(\tilde{x}_n^*)$  is the objective value of the current estimate of the optimum at this iteration,  $f(x^*)$  is the value of the true optimum, and an iteration consists of a single preference query between two points. Additionally, we also check the statistical significance of the reduction in IR obtained by PES-P compared to both EI and LH via two-sided Mann-Whitney  $U$  tests ( $p < 0.05$ ).

#### 5.3.1 Optimizing Randomly Generated Objective Functions

To avoid inducing bias by hand-engineering test functions, we first evaluate the algorithm on random synthetic objective functions. We generate objective functions on the domain  $x \in [-1, 1]^D$  by sampling a vector of 500 function values from a GP prior with a quadratic mean,  $\mu(x) = -x^T x$ , and isometric squared exponential covariance  $k(x_i, x_j) = \exp\left(\frac{-1}{2\lambda} x_i^T x_j\right)$ . We use a quadratic mean function to bias

Figure 5.2: Performance of predictive entropy search with preferences (PES-P), expected improvement (EI), and Latin hypercube random sampling (LH) for optimizing random objective functions sampled from a GP (a-d), and tuning feedback control parameters of random linear systems (e-f) and a biped walking model (g-h). Shown are the median and interquartile range over 20 trials of the immediate regret (IR) against the number of preference queries. Black stars indicate iterations for which PES-P achieves statistically significant stochastic reductions in IR compared to both EI and LH according to two-sided Mann-Whitney  $U$  tests ( $p < 0.05$ ).

<sup>3</sup> LH sampling divides the parameter space into  $(2N)^D$  hypercubes, where  $D$  is the dimensionality of the space.  $2N$  samples are placed such that each hypercube has at most one sample and there is at most one filled hypercube along any row of hypercubes when viewed along any direction. This method ensures that the samples are roughly uniformly distributed in the entire space. At each iteration we choose two of these samples to query users.

the function distribution away from those that have their optimum on a boundary of the domain, as these functions are easier to optimize. We continue to generate the rest of the function as it is optimized by conditioning the GP on the 500 seed values and all function values sampled during the optimization. We assume the mean of the final function distribution is the true objective function. To simulate more realistic situations, we provide the algorithms with noisy preferences from the sampled function values ( $\sigma^2 = 0.1$ ).

Figures 5.2a-d show the immediate regret for two to five dimensional problems with  $\lambda$ , the length scale of the kernel, scaling from 0.1 to 0.4 as the dimensionality of the problem increases. On two to four dimensional problems, PES-P outperforms EI and LH by achieving statistically significant reductions in IR. However, as the dimensionality increases, it takes more iterations for this advantage to become apparent. In the five dimensional case, there is no significant difference between PES-P and LH, likely due to  $M = 12$  samples of  $x_m^*$  being insufficient and the difficulty of accurately sampling  $x_m^*$  in higher dimensions.

### 5.3.2 Tuning Controllers for Random Linear Systems

Next, we test the ability of PES-P to optimize simple control systems by optimizing the feedback gains  $K$  for  $D$ -dimensional single-input linear systems  $\dot{\xi} = A\xi + Bu$  with feedback  $u = K\xi$ . We sample the elements of the  $A$  matrix from the standard normal distribution while  $B = [0_{1 \times (D-1)}, 1]^T$ . We assume a quadratic instantaneous cost resulting in the objective function

$$f(K) = - \int_0^{t_f} \xi_K^T(t)(Q + K^T R K)\xi_K(t)dt, \quad (5.12)$$

where  $\xi_K(t)$  is the evolution of the state under the control policy  $K$  and a fixed initial condition  $\xi_0$ ,  $Q = I_{D \times D}$  and  $R = 1$ . To obtain a finite search domain, we find the stable range of parameters by varying the elements of the true optimal control parameters  $K^*$  one at a time while keeping other elements constant. We scale and shift this region to map to the domain  $[-1, 1]^D$ . Finally, we use the Automatic Relevance Determination Gaussian Kernel and optimize the hyperparameters at each iteration by maximizing the posterior probability of the hyperparameters under a gamma hyperprior [Chu and Ghahramani, 2005, Williams and Rasmussen, 2006]. In order to apply a consistent noisy preference model ( $\sigma^2 = 0.1$ ) across all sampled systems, we transform all objective values by first mapping them through  $-\log(-f(K))$  and then shifting and scaling the values by the mean and range of the values of  $10^D$  randomly sampled controllers.

Figures 5.2e and 5.2f show the resulting optimization performance on three and four dimensional systems. In the 3 dimensional case, PES-P achieves a lower median IR than LH after 30 iterations. This difference becomes significant after 60 iterations. In the 4 dimensional case, PES-P significantly outperforms LH after 50 iterations, but the significance of this improvement is sporadic as the iterations continue. A possible reason for the reduced performance difference between PES-P and LH in the LQR problem as compared to the random objective function problems is the existence of hard-to-optimize flat regions in the LQR objective functions. This suggests that PES-P may be more well suited for problems that have clear optimum.

### 5.3.3 Tuning Control Parameters of a Walking Model

In the third case, we test the ability of PES-P to optimize the feedback gains for a neuromuscular model of walking [Thatte and Geyer, 2016], a system with a complex non-linear controller addressing the specific application domain of human locomotion. We perform two and three dimensional optimizations, in which we tune the feedback gains for a subset of the model’s muscle actuators. We use the negative cost of transport plus the distance walked over a 20 second time span as the objective function. As in the previous linear systems example, we obtain noisy preferences between parameters and optimize the hyperparameters at every iteration.

Figures 5.2g and 5.2h show the performance of PES-P, EI, and LH. In this example, PES-P achieves a significant reduction in IR in just 10 iterations in the 2-dimensional case and in 25 iterations in the 3 dimensional case. Furthermore, in the 3D case the PES-P’s median solution is approximately 10 times better than those found by EI or LH.

## 5.4 Bayesian Approach Discussion

We presented a new optimization algorithm (PES-P) that extends Predictive Entropy Search to preference feedback. The algorithm addresses two key problems frequently encountered in system optimization. First, it circumvents the often difficult process of parameterizing and learning an objective function by directly querying users for preferences between pairs of parameters. Second, the algorithm minimizes the required number of experiments by employing Bayesian optimization techniques that ensure the queries maximize the information gained about the location of the optimum. Moreover, unlike previous approaches for preference learning on robotic systems [Wilson et al., 2012, Jain et al., 2013], PES-P does not require a

model of the system.

Our experiments show that the proposed algorithm outperforms baseline algorithms. In most of the simulation experiments PES-P found optima that achieved higher objective values than those found by the expected improvement method (EI) or by random comparisons via Latin hypercubes (LH) (fig. 5.2). The reason why PES-P outperformed EI is likely due to the former's explicit consideration of how the limited, noisy information obtained from a preference query will affect the knowledge about potential objective function optima. The acquisition function (eq. (5.8)) recognizes that preferences become more uncertain the closer two sample points are to each other. EI, on the other hand, does not reason about noisy preferences and, instead, still assumes it can sample values (eq. (5.6)). Consequently, EI ignores the distance between sample points, which often leads to a greedy strategy that solicits preferences between adjacent points. While this strategy can resemble gradient ascent with convergence to local optima in a noise-free optimization, it often failed in our experiments characterized by noisy observations. Note, however, that such limitations were not observed by Brochu and colleagues [Brochu et al., 2008], who successfully used EI with preferences to optimize parameters for a graphics application, possibly because the associated visual task produced less noisy responses than did our simulations or prosthesis walking task.

## 5.5 Bandit Approach - Introduction

There is a clear trend in research and recent commercial products towards robotic prostheses that promise to ameliorate the gait deficiencies imposed by prevailing mechanically-passive devices. With the robotization of prostheses, clinicians can now tune a large number of control parameters in order to maximize the performance of these devices for each user.

Given the variability in human gait patterns, it is important to tailor these gait policies for specific users. Recently, Zhang et al. [2017] demonstrated this by optimizing an ankle exoskeleton's torque trajectory for specific users. The authors found that optimized torque trajectories could reduce metabolic energy consumption beyond that provided by a generic assistance strategy.

Others have investigated optimization methods for prostheses specifically. For example, Huang et al. [2016] propose a cyber expert system that uses pre-defined rules to modify impedance control parameters in order to improve the trajectory-tracking performance of a powered knee prosthesis. This approach was later improved by

discuss how it could not handle high enough dimensions which motivates bandit based approach tried next

using adaptive reinforcement learning to circumvent predefining the tuning rules [Wen et al., 2016].

A drawback of these previously proposed methods are their reliance on numeric optimization criteria, such as metabolic energy or trajectory tracking performance. It is unclear if optimizing prostheses to follow a specific trajectory will result in a positive outcome given the asymmetries in actuation, kinematics, and inertia induced by an amputation and wearing a prosthesis. Moreover, myopic optimization of a single aspect of gait may neglect other characteristics that are often subjective such as comfort and confidence. Therefore, in this work, we utilize subjective preferences between pairs of policy parameters in order to achieve a more holistic approach to prosthesis optimization.

A second difficulty for existing methods is tackling the high dimensional, constrained optimization problem imposed by multi-joint assistive devices such as transfemoral prostheses. Previously published impedance control strategies for transfemoral prostheses have roughly 30 tunable parameters for a given gait condition, such as walking at a specific speed. Sup et al. [2011] show that these parameters also vary with alternative conditions such as incline. Therefore, these kinds of parameterized policies could require on the order of 100 parameters to deal with a range of situations. Previous work has attempted to reduce the number of parameters via heuristic rules that tie impedance parameters to other states of the prosthesis such as joint angles [Simon et al., 2014]. However, it is not obvious how to translate these heuristics to other control strategies, such as neuromuscular control [Thatte and Geyer, 2016], which models muscles and neural reflexes, or phase-based control [Quintero et al., 2016], which follows knee and ankle trajectories parameterized as functions of hip angle and hip angle integral.

To deal with high-dimensional parameter selection for prostheses, many have turned to offline optimization of control parameters. Markowitz et al. [2011] use data from a height-and weight-matched intact subject to obtain speed-adaptive neuromuscular control parameters for a transtibial amputee's prosthesis and Aghasadeghi et al. [2013] use an invariant gait representation to model an amputee's gait and find the appropriate impedance control parameters. In these approaches however, it is unclear how well the resultant parameters suit the subject when executed on actual hardware.

In this paper, we tackle these issues by framing prosthesis optimization as a dueling bandits problem [Yue et al., 2012]. The resulting approach utilizes the subject's preferences to include subjective user feedback in the tuning process. The method deals with high dimensional optimization problems by incorporating domain knowl-

edge in the form of an offline optimization step. We show that this method produces a library of parameters from which different users prefer different options and for which preferred controllers tend to follow human gait trends. Moreover, we explore further utilizing the offline optimization to help the controllers generalize to speeds that were not included during the online optimization process.

## 5.6 Bandit Approach Methods

### 5.6.1 Transfemoral Prosthesis Design and Control

In this study, we use a transfemoral prosthesis and high-level neuromuscular control that we first presented in Thatte and Geyer [2016]. We briefly review improvements to the hardware design and control strategy here.

Our prosthesis design (??a) features series elastic actuators at both joints (SEAs [Pratt and Williamson, 1995]) that enable accurate torque control. These actuators consist of brushless motors (knee: Robodrive ILM85-13HS, ankle: ILM70-10HS) coupled to Harmonic Drive gear sets (CSG-25-50 and CSG-20-100, respectively). The actuators deliver peak torques of 170 N·m at both joints and peak speeds of  $1.93 \text{ rev/s}$  at the knee and  $1.17 \text{ rev/s}$  at the ankle. Absolute encoders (2x Renishaw Resolute at the knee and one Renishaw Resolute and one Netzer DS-25 at the ankle) located on both sides of fiberglass leaf springs (Gordon Composites) measure spring deflection and thereby joint torque. We mount an IMU (YEI Technology 3-Space Sensor) to the user's ipsilateral thigh to estimate the thigh angle with respect to the vertical axis. We detect stance/swing transitions via hall effect sensors that measure the deflection in the prosthesis' composite foot (Freedom Innovations Pacifica-LP). The completed prototype weighs about 6 kg and is donned by able-bodied subjects via an L-shaped adaptor.

The control of the prosthesis distinguishes between a lower level and a behavioral level. At the lower level, each actuator is controlled by a SEA controller [Schepelmann et al., 2012] that regulates desired joint torque by commanding desired motor velocity. The behavioral level generates the desired joint torques for the knee and ankle. We further subdivide the behavior level into its stance and swing components.

clean up this section because  
I've been cutting and pasting  
out of it into earlier in the  
document

### 5.6.2 Optimization method

To optimize the control parameters of this neuromuscular trans-femoral prosthesis control for specific users, we frame the task as a  $K$ -armed dueling bandits problem [Yue et al., 2012]. In this formalism, at each iteration  $t \in [1, \dots, T]$  of the optimization, an algorithm chooses two options, referred to as bandits, out of the set of  $K$  possibilities, so as to minimize the total cumulated regret over the iterations. The cumulated regret is defined as

$$R(T) = \zeta^* T - \frac{1}{2} \sum_{t=1}^T E[\zeta_{1t} + \zeta_{2t}] \quad (5.13)$$

where  $\zeta^*$ ,  $\zeta_{1t}$ , and  $\zeta_{2t}$ , are the values of the optimal bandit and first and second bandits chosen on iteration  $t$  respectively. To minimize  $R(T)$ , algorithms must effectively trade off exploration of all bandits to gain confidence in their values and exploitation of the best bandit so as to not incur regret.

In a dueling bandits problem, we do not observe numeric rewards directly. Rather, we observe if an oracle prefers the first bandit to the second. Because we never directly observe numeric values, algorithms for this problem use alternative notions of value. In this work, we utilize the Double Thompson sampling method [Wu and Liu, 2016], which achieves state-of-the-art regret on several datasets. This method defines a bandit's value as its Copeland Score: the number of other options that a bandit defeats on average.

Key to employing this method for prosthesis optimization is offline generation of parameter sets for which we are likely to obtain reasonable gaits for different subjects. This task can be viewed as sampling from the set of parameters that produce gait patterns consistent with human locomotion. In this work, we explore generating this set of controllers using a recently published gait data set that includes kinematics and kinetics for individual subjects walking at three different speeds, 0.8, 1.2, and 1.6 m/s [Moore et al., 2015]. For each subject in this dataset, we use the Covariance Matrix Adaptation Strategy [Hansen, 2006] to find neuromuscular model parameters  $\Gamma$  that reproduce the subject's body-weight-normalized knee and ankle joint torques  $\tau_h = [\tau_h^k, \tau_h^a]^T$  given the subject's hip, knee, and ankle angle trajectories  $\theta_h = [\theta_h^h, \theta_h^k, \theta_h^a]^T$ . Specifically, we solve

$$\Gamma = \operatorname{argmin}_{\Gamma} (\tau_h - \tau_{nm})^T (\tau_h - \tau_{nm}) + \alpha \xi_{nm}^T \xi_{nm} \quad (5.14)$$

where  $(\tau_{nm}, \xi_{nm}) = \text{neuro}_{\Gamma}(\theta_h)$  are the torques and muscle activations generated by the neuromuscular model given the human joint angle trajectories and model parameters.  $\alpha = 0.01$  is a small constant we use to help regularize the solutions.

Table 5.1 shows the parameters we optimize during this process. For each parameter in the Speed-Independent category, we look for a single value to use across all speeds. For parameters in the Speed-Dependent category we search for three different values, one for each gait speed in the dataset (0.8, 1.2, and 1.6 m/s). The parameters we choose to optimize include the isometric force and feedback gains for each muscle, which are closely related to the effective stiffness of the joint [Geyer et al., 2003], muscle prestimulations, which are related to the stride energy [Geyer et al., 2003], and the muscle reference angles, to help deal with the kinematic variability between subjects [Geyer and Herr, 2010].

From the dataset provided by Moore et al. [2015], which contains samples for twelve subjects, we were able to extract nine parameter sets. (One subject’s torque data is corrupted and two subjects’ data resulted in an overly flexed knee when used on the prosthesis.) Figure 5.3 shows an example of two subjects’ torque patterns shown in red. We see that there are significant differences between the two subjects in terms of both timing and magnitude of torque. In green, we see that after optimizing the neuromuscular model for each subject, it is able to capture both gait patterns.

We can quantify the quality of the model fit to the data by computing the root mean squared (RMS) error between the model’s predicted torques and the actual torques. Over the nine parameter sets we achieve a median RMS knee torque error of 35% of the RMS human knee torque, and a median RMS ankle torque error of 15% of the RMS human ankle torque. Much of the error in the knee torque prediction occurs right after heel strike, where the model typically predicts near-zero torque. In future work we plan to adapt the model to produce more knee flexion torque at heel strike, which should significantly reduce the model error.

To compensate for kinematic differences between the prosthesis and the training data, before sending prosthesis joint angles to the neuromuscular control, we add constant bias angles to the joint encoder readings so that at joint  $j$ ,

$$\theta_{\text{model}}^j = \theta_{\text{encoder}}^j + \theta_0^j. \quad (5.15)$$

We hand-tune these bias parameters for each bandit and subject to ensure the bandits work as well as possible.

### 5.6.3 Experiment Procedure

In our experiment, we test the ability of our offline optimization approach to generate controllers that are suited to different subjects and to produce kinematics and kinetics similar to those of intact subjects.

	Speed-Independent	Speed-Dependent
$F_{\text{ham}}^{\text{max}}$	ham $\phi_0^{\text{hip}}$	$F+G_{\text{ham}}^{\text{ham}}$
$F_{\text{vas}}^{\text{max}}$	ham $\phi_0^{\text{knee}}$	$F+G_{\text{vas}}^{\text{vas}}$
$F_{\text{bfsh}}^{\text{max}}$	vas $\phi_0$	$F+G_{\text{gas}}^{\text{gas}}$
$F_{\text{gas}}^{\text{max}}$	bfsh $\phi_0$	$F+G_{\text{sol}}^{\text{sol}}$
$F_{\text{sol}}^{\text{max}}$	gas $\phi_0^{\text{knee}}$	$F-G_{\text{sol}}^{\text{sol}}$
$F_{\text{ta}}^{\text{max}}$	gas $\phi_0^{\text{ankle}}$	$L+G_{\text{bfsh}}^{\text{bfsh}}$
$\text{off}_{\text{bfsh}}^{\text{bfsh}}$	sol $\phi_0$	$L-G_{\text{vas}}^{\text{vas}}$
$\text{off}_{\text{vas}}^{\text{bfsh}}$	ta $\phi_0$	$L+G_{\text{ta}}^{\text{ta}}$
$\text{off}_{\text{ta}}^{\text{ta}}$	$S_{\text{vas}}^{\text{ham}}$	
	$S_0^{\text{ham}}$	

Table 5.1: Optimized parameters,  $\Gamma$ . Speed-independent parameters use a single value for all speeds, while speed dependent parameters have distinct values for 0.8, 1.2, and 1.6 m/s gaits. Consequently, in total we optimize 43 parameters.  $F_{\text{max}}$  refers to a muscle’s maximum isometric force,  $\phi_0$  is a parameter used for muscle moment arm calculations, and  $S_0$  is a muscle’s pre-stimulation.

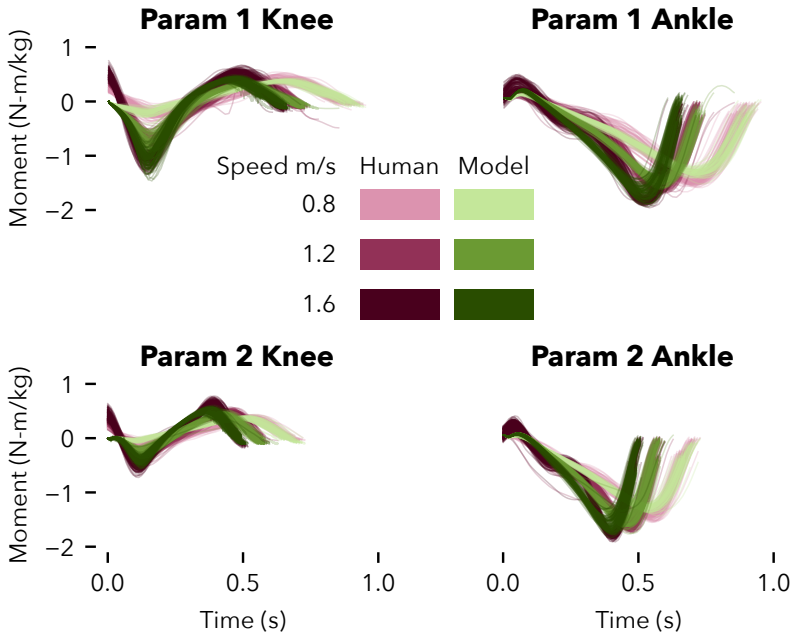


Figure 5.3: Results of the offline optimization that fits the neuromuscular model to intact-subject gait data. Shown are the knee and ankle torques for two different subjects. These plots show there can be significant inter-subject gait variability.

We further test the effectiveness of using offline optimizations to help improve the ability of the control to generalize to speeds different than those experienced during the online optimization.

After providing informed consent to a protocol approved by the Carnegie Mellon University Internal Review Board, five non-amputee subjects (four male, one female, average mass = 68.8 kg std 11.17 kg) donned the prosthesis via the able-bodied adaptor shown in ???. On the contralateral leg, subjects wore a lift shoe, the height of which we adjusted to ensure subjects' hips were even when standing.

Subjects participated in a three day study. On the first day, subjects acquainted themselves with the prosthesis for roughly 2 hours. By the end of this period, all subjects were able to walk (while holding hand rails) consistently without tripping on a set of hand-tuned parameters at a speed of up to 1.2 m/s. On the second day, the first 15 minutes consisted of hand-tuning the bias angles for each parameter set (eq. (5.15)) to allow the subject to achieve adequate ankle and knee flexion for as many parameters as possible. Then, we performed the dueling bandits optimization for 50 iterations, which required approximately thirty minutes of walking at 0.8 m/s. Each iteration consisted of roughly ten seconds of walking on each parameter, after which the subject indicated their preference. If subjects were unsure of their decision they could walk with both parameter sets multiple times. If their uncertainty persisted, the experimenter chose

the parameter set that produced angles and torques more aligned with human data. If the experimenter also had no preference, a random number generator selected the winner. We chose to perform fifty iterations, as pilot testing suggested this was sufficient for the algorithm to begin comparing the optimal parameter set to itself, indicating a high level of confidence in the optimum.

On the third day, subjects walked with their preferred parameters at 0.8, 1.0, 1.2, 1.4, and 1.6 m/s. For each speed, we tested both the appropriate speed-dependent parameters and those designed for 0.8 m/s. To obtain parameters for 1.0 and 1.4 m/s we performed linear interpolation between the adjacent parameters. Finally, we recorded the subject's gait at 0.8 m/s for all non-preferred parameter sets and the hand-tuned parameters used on the first day.

## 5.7 Bandit Approach Results

### 5.7.1 Copeland Scores

The five subjects in the study preferred four different parameter sets out of the nine parameter sets they could choose from, thereby demonstrating that the offline optimization approach can generate parameters that suit different users. Figure 5.4 shows the total Copeland score achieved by each parameter set across all five subjects. From this chart, we can see it is possible, as in the case of parameter set 6, that a controller receives high scores from some users while receiving a score of zero from other users. This illustrates the importance of tailoring prostheses to individual users. Some parameters such as parameters 1, 4, and 8, achieved consistently low scores across all users. It may be possible for us to remove these parameters from future studies. However, more subjects would be needed before making such a determination as parameter set four received a relatively high score from subject five.

### 5.7.2 Kinematics and Kinetics at 0.8 m/s

Figure 5.5 shows the ankle and knee kinematics achieved by all subjects on all parameters at 0.8 m/s. The thicker solid lines indicate the gait data produced by subjects' preferred parameters and the dashed lines indicate the gait data produced by the hand-tuned parameters. We see that subject gait with both their preferred parameters and hand-tuned parameters follow similar trends to intact gait data [Bovi et al., 2011], whose mean and three sigma variance is shown as the blue shaded region. However, all subjects preferred the optimized parameters to the hand-tuned set.

Just as in the intact data, there is significant variation in subjects' preferred gait characteristics, which reinforces the idea that targeting a specific kinematic or kinetic pattern may not be ideal for all users. This seems to be especially true of the knee joint moment, where there are significant differences in the amount of knee extension torque in early stance and flexion torque in late stance among users.

We found that most subjects produced relatively little ankle dorsiflexion as they walked. Consequently, for most subjects the neuromuscular model control produced less ankle plantarflexion torque than is average for able-bodied subjects. We believe the low level of ankle dorsiflexion was caused by the relatively short foot of the prosthesis, which we plan to rectify for future experiments. However, this effect also betrays a potential weakness of the approach: optimizing to match able-bodied kinetics given able-bodied kinematics may not be able to rectify some types of discrepancies between the human and the prosthesis.

### 5.7.3 Control Performance at Higher Gait Speeds

Figure 5.6 shows the average net ankle work<sup>4</sup> produced by the control strategy at speeds ranging from 0.8 to 1.6 m/s. Data from subjects 1, 2, and 3, who chose parameter sets 5, 9, and 3 respectively, show a clear downwards trend in ankle work as speed increases when using a constant set of gains. On the other hand, with the adaptive gains, as speed increases ankle work increases, mimicking the behavior of the biological ankle [Herr and Grabowski, 2011]. All three of these subjects preferred the behavior of the adapted parameters to the parameters for 0.8 m/s when walking at 1.4 and 1.6 m/s.

Subjects 4 and 5 both chose parameter set six and show no clear trend in ankle work as speed increases. For this parameter set, the

<sup>4</sup>The area within the torque versus angle plot of the ankle over a stride.

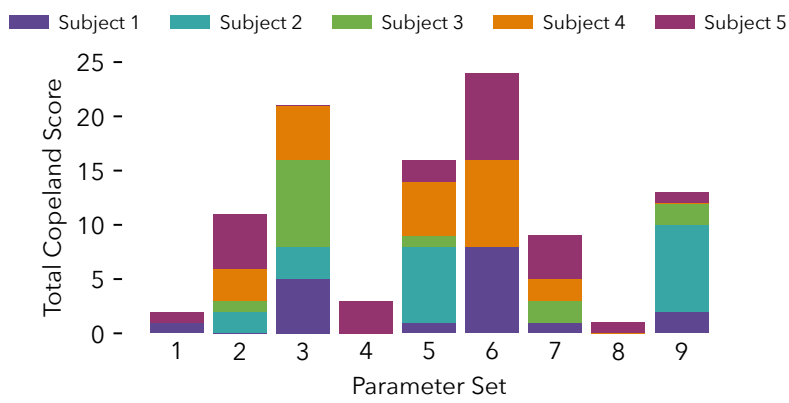


Figure 5.4: Total Copeland score achieved by each parameter set across all five subjects.

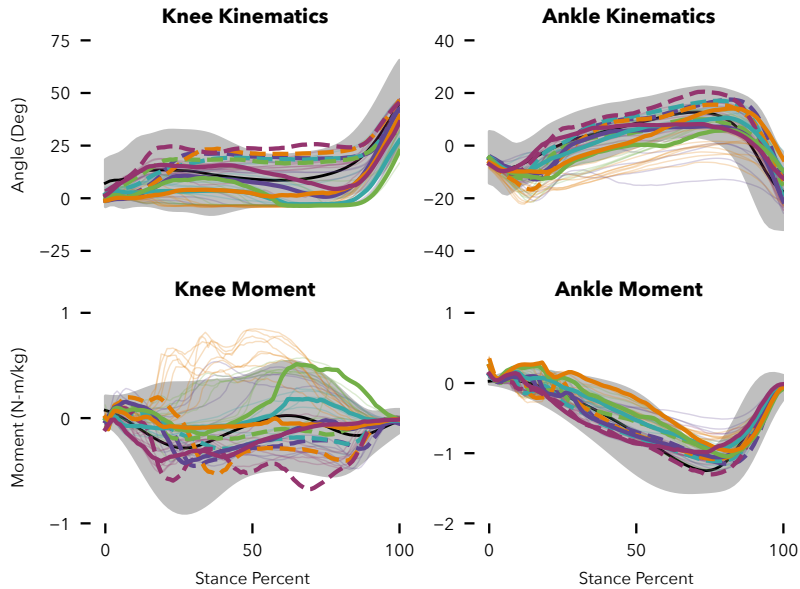


Figure 5.5: Median angles and moments at 0.8 m/s for all parameter sets for all subjects. Thicker weight solid lines indicate each subject's gait with their preferred parameters. Dashed lines indicate gait with hand-tuned parameters. The grey shaded regions show the mean and three sigma intact subject gait data (from the extra slow walking data in [Bovi et al., 2011]).

speed adapted gains only increased ankle work significantly over baseline at 1.6 m/s for both subjects. Additionally, these two subjects indicated no trend in preference between the adapted and unadapted parameters at the higher speeds. These two subjects produced different amounts of net work despite using the same parameter set. This is likely due to kinematic differences between the subjects as well as differently tuned bias settings for the ankle joint.

From this result we can conclude that the offline optimization approach can produce improved responses at speeds other than that at which we conduct the online optimization, but that the improvement needs to be confirmed on a per-parameter basis. It is not currently clear why parameter set six does not exhibit increasing ankle work as speed increases as the underpinning human data for this parameter set does indeed exhibit the desired trend. The issue could possibly lie with the structure of the high level control or with local minimums obtained by the CMA-ES method.

### 5.8 Bandit Approach Discussion

We present a new approach for online optimization of lower limb assistive devices that uses preference feedback to incorporate the user's subjective assessment of device behavior. The method tackles high dimensional tuning problems by incorporating domain knowledge via an offline optimization step that utilizes kinetic and kinematic data from intact subjects to obtain a library of policy parameters. We find

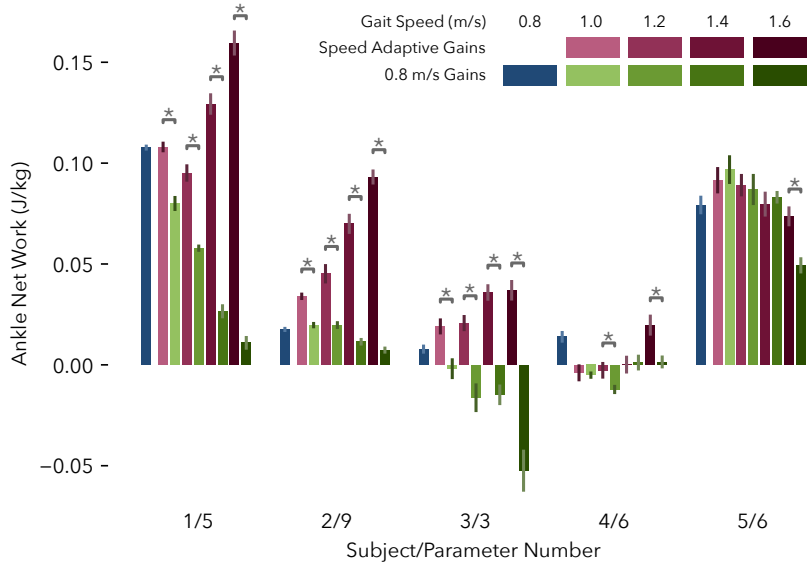


Figure 5.6: Average net ankle work for each subject at each speed. Red bars indicate trials where speed-adaptive gains were used whereas green bars indicate trials performed with the gains for 0.8 m/s. Stars indicate statistically significant differences between the work produced by the speed adaptive gains and that produced by the 0.8 m/s gains ( $p < 0.05$ ).

that the five subjects who completed our experiment preferred four different parameter sets from this library. The resulting gait patterns resembled intact human gait data and were preferred to hand-tuned parameters, confirming that the method can generate parameters suited for different subjects.

A result of the offline optimization we use is that the method is largely agnostic to the number of tunable parameters. Consequently, we were able to additionally optimize neuromuscular model parameters for different speeds. Our experimental results show that these parameters improved the ankle work characteristics and user preferences as speed increased for three out of four tested parameter sets.

Previous works such as Eilenberg et al. [2010] and Markowitz et al. [2011] have demonstrated control of powered ankle prostheses via neuromuscular models of muscles and reflexes. This paper extends that work, as it presents the first instance of neuromuscular control on a powered knee and ankle prosthesis. With the tuning method presented here, we hope to comprehensively test this prosthesis control strategy in future work.

Due to the ability of the method to handle problems of arbitrary dimensionality given sufficient computational resources, it may be used to tune many types of control strategies. For example, one could use the approach to optimize the phase variable control strategy, in which the prosthesis follows predefined knee and ankle trajectories parameterized as functions of hip angle and hip angle in-

tegral [Quintero et al., 2016]. In this case, each bandit would provide a different knee and ankle trajectory. Importantly, the ability of this method to optimize various types of controllers may help researchers compare control strategies fairly. Many control strategies for transfemoral prostheses have been proposed in recent years [Quintero et al., 2016, Thatte and Geyer, 2016, Lawson et al., 2014], but currently there is a dearth of studies that directly compare their merits and disadvantages.

It is probable that the parameter library we obtained in this work can be further improved. We propose two directions for further investigation: First, it may be possible to improve the library by obtaining a larger set of gait data and then using clustering algorithms to arrive at a reduced set of canonical gaits. Vardaxis et al. [1998] apply a similar idea to EMG data to cluster gaits into five major styles. With a library derived from canonical gaits, we may cover the parameter space more evenly. A second approach is to use biomechanical measurements from the amputee, such as segment lengths and measured peak joint torques, to obtain probability distributions for the neuromuscular model parameters. We could then compose the parameter library by sampling parameters from the distributions and performing rigid body simulations of the amputee and prosthesis system.

The optimization approach we have presented may have considerable practical value for commercial prostheses as well. Because it uses preference feedback, lay users of an assistive device can easily provide feedback via smartphones or wearable devices. Moreover, the dueling bandit algorithm is well suited to lifelong learning. Since the algorithm seeks to minimize regret, we can ensure its exploration is only as obtrusive as necessary.

On the third day of our experiment, we also asked three subjects to rate their sub-optimal controls relative to their optimal control from day two. Two users indicated they had slight preferences for controllers other than the one they had preferred on day two, illustrating that user preferences are not stationary. Garivier and Moulines [2008] have proposed algorithms for non-stationary  $k$ -armed bandit problems that could be adapted to the dueling bandits case and applied to assistive device optimization.

The study we presented has several limitations. First, we only had five subjects complete the study. Ideally, we would have more subjects than the number of parameter sets so we could determine if any parameters are never preferred or if any group is not currently well represented by the current set of parameters. Also, we should confirm that the proposed optimization framework provides suitable control parameters for amputees wearing this prosthesis.

### Bayesian Approach Appendix

To obtain  $X^*$  (line 5, algorithm 1), we sample  $M$  functions from the posterior by approximating  $P(f_t|D_n)$  using Bayesian linear regression with Fourier features (as outlined in [Hernández-Lobato et al., 2014]) and sampling  $M$  feature weight vectors. As the Fourier features have analytic derivatives, we can optimize each linear function using a second order method with multiple restarts.

We approximate conditioning the predictive distribution on  $x^*$  via three constraints:

$C_1$   $x^*$  is a local maximum.  $\nabla f|_{x^*} = 0$  and the Hessian of the objective function is negative definite by imposing  $\text{diag}(\nabla \nabla f|_{x^*}) < 0$  and  $\text{upper}(\nabla \nabla f|_{x^*}) = 0$ . We group  $\nabla f|_{x^*} = 0$  and  $\text{upper}(\nabla \nabla f|_{x^*}) = 0$  into constraint  $C_{1.1}$  and  $\text{diag}(\nabla \nabla f|_{x^*}) < 0$  into constraint  $C_{1.2}$ .

$C_2$   $x^*$  is preferred to current training points,  $f(x^*) > f(x_k^a)$  and  $f(x^*) > f(x_k^b)$ ,  $\forall k \in [1, n]$ .

$C_3$   $x^*$  is preferred to new training points,  $f(x^*) > f(x_{n+1}^a)$  and  $f(x^*) > f(x_{n+1}^b)$ .

We precompute the effects of constraints  $C_1$  and  $C_2$  before evaluation of  $\text{ff}_n(x^a, x^b)$ . To impose  $C_1$  and  $C_2$ , we first divide their components into two groups:  $c = [\nabla f|_{x^*}^\top, \text{upper}(\nabla \nabla f|_{x^*})^\top]^\top$  and  $f' = [f^\top, \text{diag}(\nabla \nabla f|_{x^*})^\top, f(x^*)]^\top$ . Note  $C_{1.1} \implies c = 0$ . We write the predictive distribution of the objective function at test points  $f_t$  given constraints  $C_1$  and  $C_2$  as

$$P(f_t|D_n, C_1, C_2) = \int P(f_t|f') P(f'|D_n, C_1, C_2) df'. \quad (5.16)$$

We use Bayes rule to evaluate the second term in the integral,

$$P(f'|D_n, C_1, C_2) = \frac{P(D_n, C_{1.2}, C_2|f') P(f'|C_{1.1})}{P(D_n, C_{1.2}, C_2|C_{1.1})}. \quad (5.17)$$

We form the prior term  $P(f'|C_{1.1})$  by conditioning the joint distribution,  $P(c, f')$  on  $C_{1.1}$  given by  $c = 0$ .

$$P(f'|c) = \mathcal{N}\left(f'|\Sigma_{cf'}^\top \Sigma_{cc}^{-1} c, \Sigma_{ff'} - \Sigma_{cf'}^\top \Sigma_{cc}^{-1} \Sigma_{cf'}\right) \quad (5.18)$$

implies  $P(f'|c = 0) = \mathcal{N}(f'|0, \Sigma_{ff'}|_c)$ .

We implement the likelihood term by adding extra factors to the likelihood in eq. (5.1) that impose soft constraints representing  $C_{1.2}$  and  $C_2$ . For  $C_{1.2}$  we use the penalty term  $P([\nabla \nabla f|_{x^*}]_{dd} < 0 | \nabla \nabla f|_{x^*}) = \Phi(-[\nabla \nabla f|_{x^*}]_{dd}/\sigma_h)$  and for  $C_2$  we add more preference relations between  $x^*$  and all training points.

$$\begin{aligned}
 P(D_n, C1.2, C2, |f') &= \left[ \prod_{k=1}^n P\left(x_k^a \succ x_k^b | f(x_k^a), f(x_k^b)\right) P\left(x^* \succ x_k^a | f(x^*), f(x_k^a)\right) P\left(x^* \succ x_k^b | f(x^*), f(x_k^b)\right) \right] \\
 &\quad \times \prod_{d=1}^D P([\nabla \nabla f|_{x^*}]_{dd} < 0 | [\nabla \nabla f|_{x^*}]_{dd}) \\
 &= \left[ \prod_{k=1}^n \Phi(q_k) \Phi(q_k^{a*}) \Phi(q_k^{b*}) \right] \prod_{d=1}^D \Phi(q_d^h)
 \end{aligned} \tag{5.19}$$

Where  $q_k^{a*} = \frac{f(x^*) - f(x_k^a)}{\sqrt{2}\sigma}$  and  $q_k^{b*} = \frac{f(x^*) - f(x_k^b)}{\sqrt{2}\sigma}$  and  $q_d^h = \frac{-[\nabla \nabla f|_{x^*}]_{dd}}{\sigma_h}$ .

We use Laplace's approximation to approximate  $P(f'|D_n, C1, C2)$  as Gaussian,

$$P(f'|D_n, C1, C2) \approx \mathcal{N}\left(f' | f'_{\text{MAP}}, \left(\Sigma_{f'|c}^{-1} + \Lambda_{f'_{\text{MAP}}}\right)^{-1}\right), \tag{5.20}$$

where  $f'_{\text{MAP}} = \arg \min_{f'} -\log P(f'|D_n, C1, C2)$  and  $\Lambda_{f'_{\text{MAP}}}$  is the Hessian of  $-\log P(D_n, C1.2, C2|f')$  evaluated at  $f'_{\text{MAP}}$ .

We compute the first term in eq. (5.16),  $P(f_t|f', C1.1)$  by conditioning the joint distribution  $P(c, f', f_t)$  on  $f'$  and  $c = 0$ ,

$$P(f_t|f', c = 0) = \mathcal{N}\left(f_t | \left(\Sigma_{ct}^T B + \Sigma_{ft}^T D\right) f' - \left[\Sigma_{ct}^T \quad \Sigma_{ft}^T\right] \begin{bmatrix} A & B \\ C & D \end{bmatrix} \begin{bmatrix} \Sigma_{ct} \\ \Sigma_{ft} \end{bmatrix}\right), \tag{5.21}$$

where,  $\begin{bmatrix} A & B \\ C & D \end{bmatrix} = \begin{bmatrix} \Sigma_{cc} & \Sigma_{cf'} \\ \Sigma_{cf'}^T & \Sigma_{ff'} \end{bmatrix}^{-1}$ . We can substitute eq. (5.21)

and eq. (5.20) into eq. (5.16) to yield the predictive distribution subject to constraints C1 and C2.

$$\begin{aligned}
 P(f_t|D_n, C1, C2) &= \mathcal{N}\left(f_t | (\Sigma_{ct}^T B + \Sigma_{ft}^T D) f'_{\text{MAP}}, \Sigma_{tt} - \left[\Sigma_{ct}^T \quad \Sigma_{ft}^T\right] \begin{bmatrix} A & B \\ C & D \end{bmatrix} \begin{bmatrix} \Sigma_{ct} \\ \Sigma_{ft} \end{bmatrix} \right. \\
 &\quad \left. + \left(\Sigma_{ct}^T B + \Sigma_{ft}^T D\right) \left(\Sigma_{f'|c}^{-1} + \Lambda_{f'_{\text{MAP}}}\right)^{-1} \left(\Sigma_{ct}^T B + \Sigma_{ft}^T D\right)^T \right).
 \end{aligned} \tag{5.22}$$

We obtain  $P(f_t|D_n, C1, C2, C3)$  by analytically conditioning eq. (5.22) on the single inequality  $f(x_m^*) > (f(x^a) + f(x^b))/2$  using the method detailed in [Xu and Li, 2010]. Finally, using eq. (5.11) we can compute the predictive distributions of preferences given the locations of  $x_m^*$ .

To optimize  $ff_n(x^a, x^b)$  (line 7, algorithm 1) we construct its gradient by evaluating  $P(f_t|D_n)$  and  $P(f_t|D_n, C1, C2, C3)$  at test points  $x^a$  and  $x^b$  as well as points offset by  $\delta_x = \pm 0.001$  along each dimension.

We then optimize  $\alpha_n(x^a, x^b)$  via gradient ascent.

# 6

## *Experimental Comparison of Neuromuscular and Impedance Controllers*

### 6.1 Introduction

Seek to compare controllers in a similar way as in chapter 4.

Want to make comparison as objective as possible -Minimize experimenter influence on controller parameter design/selection -Both NM and impedance control use similar procedure for generating parameters -Preferences allow user instead of experimenter to select parameters -Iterative learning for fine tuning instead of hand tuning as in section chapter 5

### 6.2 Methods

#### 6.2.1 Parameter Generation

To obtain suitable parameters for the neuromuscular and impedance control methods we rely on the dueling bandits optimization approach outlined in section 5.6.2. Whereas in section 5.6.2 we optimized control parameters to match gait data at different speeds to achieve a speed-adaptive control, in this work, we optimize control parameters to match both undisturbed and disturbed gait in order to obtain robust control parameters. We use the dataset provided by Moore et al. [2015], which provides gait data for undisturbed walking and walking with treadmill velocity disturbances.

For the neuromuscular control, we use the black-box CMA-ES optimizer [Hansen, 2006] to obtain parameters that can reproduce the behavior of each subject in the gait dataset. The model proceeds by feeding joint hip, knee, and ankle angles into the neuromuscular model which generates torques for the knee and ankle. We optimize the parameters listed in table 6.1 so the model's output torques match those in the gait dataset. Specifically, we minimize the following cost

Optimized Parameters	
$F_{\max}^{\text{ham}}$	$F^+ G_{\text{ham}}^{\text{ham}}$
$F_{\max}^{\text{vas}}$	$F^+ G_{\text{vas}}^{\text{vas}}$
$F_{\max}^{\text{gas}}$	$F^+ G_{\text{gas}}^{\text{gas}}$
$F_{\max}^{\text{sol}}$	$F^+ G_{\text{sol}}^{\text{sol}}$
$F_{\max}^{\text{ta}}$	$F^- G_{\text{sol}}^{\text{ta}}$
$\text{off}_{\text{ta}}$	$L^+ G_{\text{ta}}^{\text{ta}}$
$\text{off}_{\phi_{\text{knee}}}^{\text{vas}}$	$\phi G_{\text{knee}}^{\text{vas}}$
$S_0^{\text{vas}}$	$\epsilon_{\text{SE}}^{\text{ap}}$
$S_0^{\text{ham}}$	$F_{\text{init}}^{\text{ham}}$

Table 6.1: Optimized parameters,  $\Gamma$ . We optimize 18 parameters.  $F_{\max}^m$  refers to muscle  $m$ 's maximum isometric force,  $S_0^m$  is muscle  $m$ 's pre-stimulation, signal  $G_n^m$  is the gain on a feedback signal from muscle  $n$  acting on muscle  $m$ ,  $\epsilon_{\text{SE}}^{\text{ap}}$  is the tendon reference strain of the ankle plantarflexors (sol and gas) and  $F_{\text{init}}^{\text{ham}}$  is the initial force in the hamstring MTU at heelstrike.

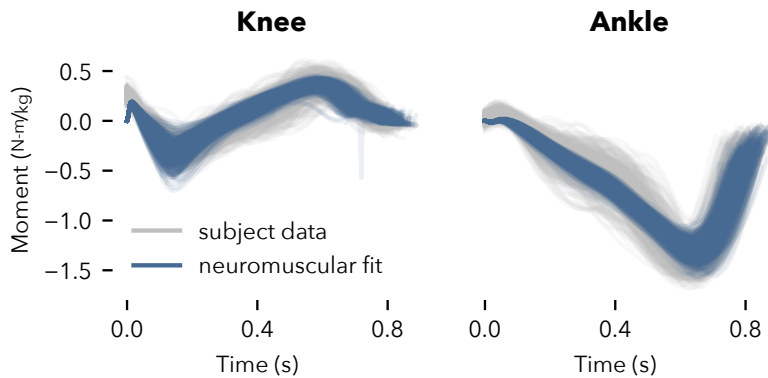


Figure 6.1: Example of fit to subject data achieved by neuromuscular model.

function:

$$\Gamma = \operatorname{argmin}_{\Gamma} (\tau_h - \tau_{nm})^T (\tau_h - \tau_{nm}) + \alpha \xi_{nm}^T \xi_{nm} \quad (6.1)$$

where  $(\tau_{nm}, \xi_{nm}) = \text{neuro}_{\Gamma}(\theta_h)$  are the torques and muscle activations generated by the neuromuscular model given the human joint angle trajectories and model parameters  $\Gamma$ .  $\alpha = 0.01$  is a small constant we use to help regularize the solutions and prevent muscle stimulations from saturating. Figure 6.1 shows an example of the fit achieved to one subject's joint moments.

To generate parameters for impedance control, which is described in full in ??, we follow a two step procedure: In the first step, we identify appropriate joint angle thresholds that define the impedance controller's finite state machine transition rules. The impedance control transition from phase 1 to phase 2 of stance is based on the knee angle crossing a threshold. We specify this threshold such that 95% of steps in the subject's gait data pass from phase 1 to phase 2. As we use gait data with disturbances, this procedure automatically sets the threshold such that it allows for a large degree of gait variation. Next, we identify the ankle angle threshold that defines the transition between stance phases 2 and 3. Again, we set this threshold such that 95% of steps successfully complete the transition.

fix reference

Once we identify the joint angle thresholds that define state transitions, we next fit the impedance parameters within each phase. In

each phase, the torque output of the impedance control is

$$\tau_{\text{imp}} = -k(\theta - \theta_0) - b\dot{\theta} \quad (6.2)$$

$$= \begin{bmatrix} -\theta & -\dot{\theta} & 1 \end{bmatrix} \begin{bmatrix} k \\ b \\ k\theta_0 \end{bmatrix} \quad (6.3)$$

$$= \Theta \vec{k} \quad (6.4)$$

where  $\Theta$  is a matrix of the subject's joint angles and velocities and  $\vec{k}$  is a vector of the impedance parameters. Therefore, the squared error between the subject's joint torque and the impedance control model is

$$\epsilon_\tau = (\tau_{\text{imp}} - \tau_h)^T (\tau_{\text{imp}} - \tau_h) \quad (6.5)$$

$$= \vec{k}^T \Theta^T \Theta \vec{k} - 2\tau_h^T \Theta \vec{k} + \tau_h^T \tau_h \quad (6.6)$$

To calculate the impedance parameters for each phase we minimize the squared error subject to the constraints that  $k > 0$  and  $b > 0$ , which ensures that the resulting impedance models are stable. Finally, to obtain model parameters that are robust to outlier steps in the dataset, we utilize the RANSAC procedure, which iteratively solves the above optimization on randomly sampled subsets of the data in order to classify and fit to inliers only [Fischler and Bolles, 1981].

Figure 6.2 shows an example of the impedance control model optimized to match one subject's gait data. In this figure, the color of the lines indicates the phase of gait. We see that the majority of steps fit the subject's joint moments (grey) well. However, there are a few steps for which the color of the line and thus the phase does not transition properly. Consequently, the resulting torque diverges greatly from the human data. This is expected as the phase transition angles were selected such that 95% of steps pass through each phase transition. We did not allow 100% percent of steps through so as to ignore potential outlier steps.

### 6.2.2 Iterative Learning

In section 5.6, in order to compensate for kinematic differences between the joint angles in the gait dataset and the joint angles of the prosthesis, we applied hand-tuned offsets to the measured prosthesis joint angles before calculating the neuromuscular model torques (eq. (5.15)). These offsets helped ensure the prosthesis achieved comfortable levels of ankle dorsiflexion, and prevent knee over extension (or flexion) during stance. In this experiment, in order to reduce the potential for bias induced by hand tuning, we take a more systematic, iterative learning approach to tuning these offsets.

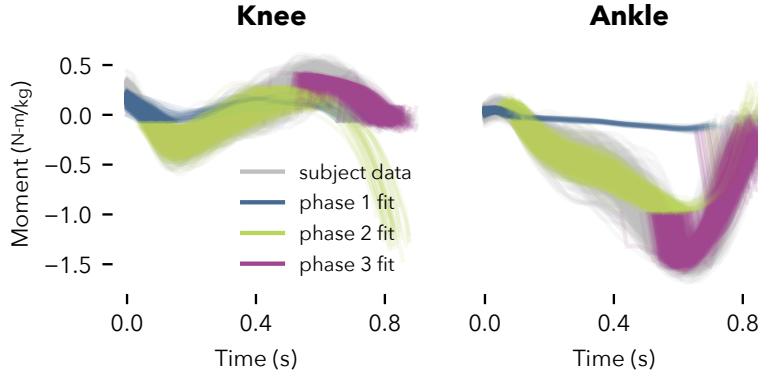


Figure 6.2: Example of fit to subject data achieved by impedance control model to. Note that green trajectories in knee moment plot and blue trajectories in ankle moment plot that do not track subject data are those that did not successfully transition to the next phase.

During the iterative learning procedure, a subject walks with each parameter set for both the neuromuscular and impedance controllers. The knee and ankle angle trajectories during stance are recorded and after each step, the following update rules are applied to the knee and ankle joint offsets

$$\theta_{\text{knee}}^{\text{offset}} \leftarrow \theta_{\text{knee}}^{\text{offset}} + k_{\text{lrm}} (\theta_{\text{knee}}^{\text{ext}} - \theta_{\text{knee}}^{\text{ext,tgt}}) (\theta_{\text{knee}}^{\text{flex}} < \theta_{\text{knee}}^{\text{flex,max}} \text{ OR } \theta_{\text{knee}}^{\text{ext}} > \theta_{\text{knee}}^{\text{ext,tgt}}) \quad (6.7)$$

$$\theta_{\text{ankle}}^{\text{offset}} \leftarrow \theta_{\text{ankle}}^{\text{offset}} + k_{\text{lrm}} (\theta_{\text{ankle}}^{\text{flex}} - \theta_{\text{ankle}}^{\text{flex,tgt}}), \quad (6.8)$$

where  $k_{\text{lrm}} = 0.05$  controls the learning rate,  $\theta_{\text{knee}}^{\text{ext}}$  and  $\theta_{\text{knee}}^{\text{ext,tgt}} = 0^\circ$  are the measured and target knee extension in mid-stance respectively and  $\theta_{\text{ankle}}^{\text{flex}}$  and  $\theta_{\text{ankle}}^{\text{flex,tgt}} = 12^\circ$  are the measured and target ankle dorsiflexion in mid-stance respectively. The conditional terms in the knee iterative learning rule prevent the knee offset angle from inducing more knee flexion if the knee flexion in early stance  $\theta_{\text{knee}}^{\text{flex}}$  crosses a threshold  $\theta_{\text{knee}}^{\text{flex,max}} = 10^\circ$ .

### 6.2.3 Treadmill Disturbance

In our experiment we probe the robustness of the impedance and neuromuscular prosthesis controllers. To this end, we disturb gait using treadmill velocity disturbances similar to those in the gait dataset we used to generate parameters [Moore et al., 2015]. During the disturbed walking conditions, the treadmill velocity is generated as follows: First, random accelerations are sampled from a zero-mean Gaussian distribution with variance  $35 \text{ m}^2/\text{s}^4$ . These accelerations are saturated to the range,  $[-15, 15] \text{ m/s}^2$ . Next, the acceleration is integrated to obtain a velocity signal, which is then high-pass filtered with a passband edge frequency of 0.5 hz to remove long-term drift in

the signal. Finally, a constant offset of 0.8 m/s is applied to the velocity signal, which is then saturated to the range [0, 3.6] m/s.

#### 6.2.4 Experimental Protocol

In our experiment, we evaluate the robustness and user ratings the neuromuscular and impedance controllers in an experiment with ten able-bodied subjects wearing the prosthesis via an adaptor. All subjects provided informed consent to IRB-approved protocols.

Subject's participated in a six-day procedure:

subject stats

*Day 1: Practice Session* Subjects practiced walking on the prosthesis until they could achieve consistent gait without the use of handrails. Subjects who could not achieve hands free walking by the end of the two-hour practice session did not continue with the experiment.

*Day 2: Practice Session* Subjects returned for a second day of practice walking on the prosthesis without the use of hand rails. In addition, on this day subjects practiced walking with the disturbance described in section 6.2.3. This session lasted for 2 hours.

*Day 3: Iterative Learning* Subjects walked with each of the nine parameter sets for each controller while the iterative learning procedure (section 6.2.2) tuned the joint angle offsets.

*Day 4: Dueling Bandits Optimization* We performed the dueling bandits optimization procedure (section 5.6) to find each subject's preferred parameters with both controllers. The order in which we optimized the controller was chosen randomly.

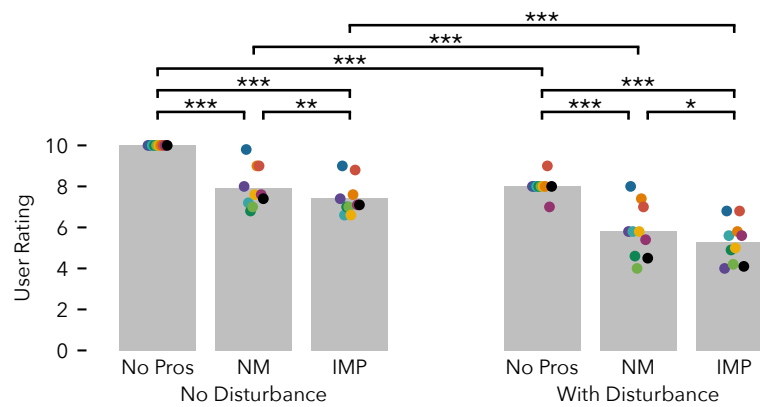
*Day 5: Disturbance Experiment - Practice* We performed a practice session for the full disturbance experiment. First, subjects walked without the prosthesis at 0.8 m/s for 2 minutes without disturbances and then 2 minutes with the treadmill velocity disturbance applied. After these no-prosthesis trials were completed, subjects donned the prosthesis and tested the neuromuscular and impedance controllers in five rounds of experiments, each consisting of three trials. In each trial, subjects walked without disturbances for 1 minute and with disturbances for 1 minute. In each round of trials, the subjects tested their preferred neuromuscular and impedance control parameters along with a set of suboptimal parameters for one controller type. Odd numbered subjects tested a suboptimal neuromuscular parameter set, while even numbered subjects tested a suboptimal impedance parameter set. For the suboptimal parameter set we chose the parameter set that ranked

#3/9 in terms of cumulative Copeland score at the end of the dueling bandits experiment.

*Day 6: Disturbance Experiment - Data Collection* The procedure for this day was identical to that of day 5. Subjects wore Vicon motion capture markers during all trials, which captured the kinematics of the legs. Additionally, subjects wore a torso-mounted IMU that measured the roll and pitch torso angles during walking. During trials, we recorded the number of falls (measured as the number of times subjects needed to use the hand rails or the ceiling-mounted hardness to recover balance) and the user ratings for both the undisturbed and disturbed conditions of each trial.

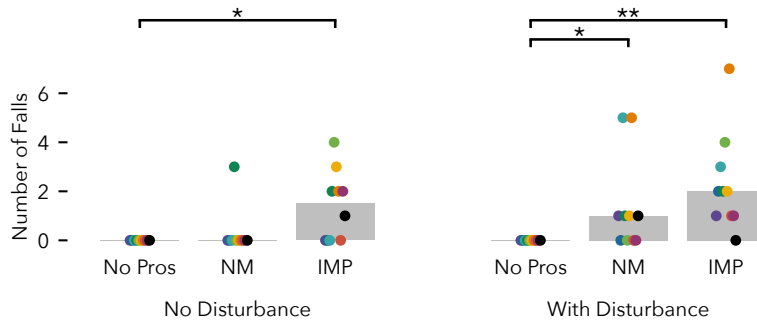
We evaluate the robustness of the two control strategies primarily by looking at the number of falls experienced by each subject in the no disturbance and disturbance cases for each controller. As a baseline, we also compare to the no prosthesis case. As secondary measures of gait robustness, we also measure the variability of the torso pitch and roll angles. The variability is measured by subtracting the median torso angle trajectory over the strides in a condition from the corresponding torso angle trajectories. Then the interquartile range (IQR) of the median subtracted trajectories is used as the measure of variability.

### 6.3 Results



First, fig. 6.3 shows the user ratings of the different conditions. We mandated that users rate the No Prosthesis/No Disturbance case 10/10 so that other conditions could be rated relative to this case. We see that in both the no disturbance and disturbance cases,

Figure 6.3: Average user ratings across all trials in both the undisturbed and disturbed walking conditions when walking without the prosthesis (No Pros) and with the Neuromuscular (NM) prosthesis control and impedance (IMP) prosthesis control. Grey bars show the mean across subjects. Statistical significance assessed by Welch's  $t$ -test. \*:  $p < 0.05$ , \*\*:  $p < 0.01$ , \*\*\*:  $p < 0.001$ .



neuromuscular control was rated significantly more preferably than impedance control. Neither control could match the ratings given to the no prosthesis case. Introduction of the disturbance caused a significant drop in user rating for all controllers.

Next, fig. 6.4 shows the number of falls in each condition. Here we see that there was significant differences in the median number of falls between impedance control and no prosthesis walking in the no disturbance case and both impedance and neuromuscular walking in the disturbance case. No significant differences were found directly between the neuromuscular and impedance controllers.

Figures 6.5 and 6.6 show the torso pitch and roll angle variability respectively. We see significant differences between the no prosthesis and with prosthesis cases as well as the no disturbance and with disturbance cases. There is also a significant increase in torso pitch variability with the impedance control compared to the neuromuscular control in the disturbance case.

Finally, table 6.2 shows a tally of the reasons for the observed falls

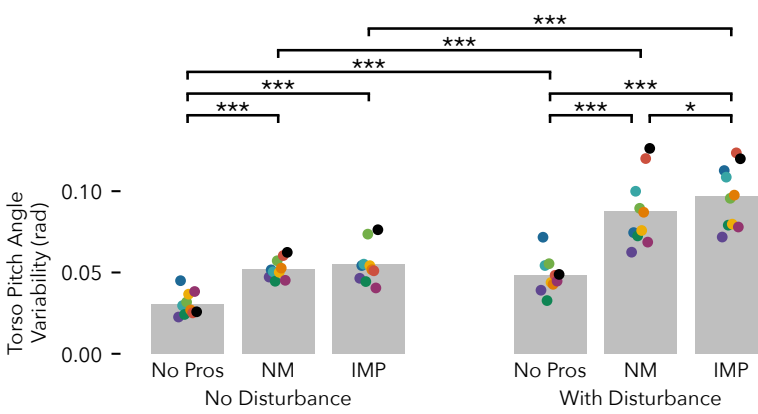


Figure 6.4: Total number of falls across all trials in both the undisturbed and disturbed walking conditions when walking without the prosthesis (No Pros) and with the Neuromuscular (NM) prosthesis control and impedance (IMP) prosthesis control. Grey bars show the median number of falls across all subjects. Statistical significance assessed by Wilcoxon signed-rank test. \*:  $p < 0.05$ , \*\*:  $p < 0.01$ .

Figure 6.5: Torso pitch angle variation. Angle variation calculated as the interquartile range of torso angles after the median torso angle trajectory over the strides in a trial is subtracted out. For the prosthesis trials, we report the average variation across the five trials for each condition. Grey bars show the mean across subjects. Statistical significance assessed by Welch's  $t$ -test. \*:  $p < 0.05$ , \*\*\*:  $p < 0.001$ .

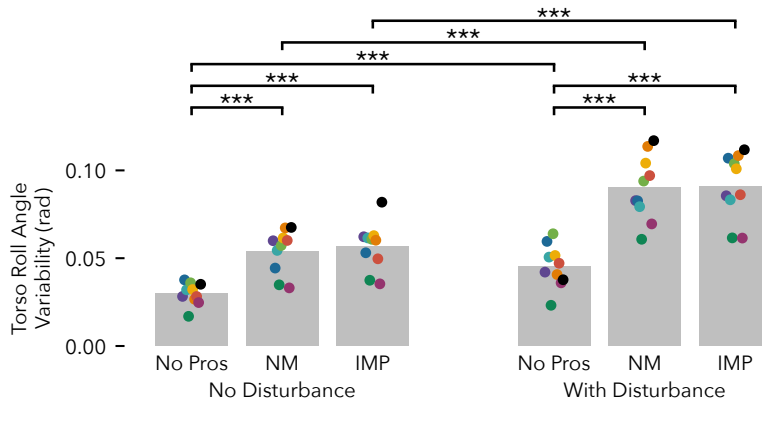


Figure 6.6: Torso roll angle variation. Angle variation calculated as the inter quartile range of torso angles after the median torso angle trajectory over the strides in a trial is subtracted out. For the prosthesis trials, we report the average variation across the five trials for each condition. Grey bars show the mean across subjects. Statistical significance assessed by Welch's  $t$ -test.\*\*\*:  $p < 0.001$ .

Fall Types	Neuromuscular	Impedance
Fall Forward	1	0
Fall Backwards	6	4
Fall Left	1	0
Fall Right	0	3
Missed Stance / Swing Transition	3	0
Missed Stance 2 / Stance 3 Transition	0	7
Knee Collapse	0	15
Swing Trip	4	12

with each controller type when using preferred parameters. The reason for each fall was determined from analyzing video recordings and logged prosthesis data. The first four categories refer to general losses of balance resulting in a fall in the four cardinal directions. Backward falls generally resulted from the treadmill suddenly stopping when the prosthesis stance leg was still in front of the body, causing a loss of balance backwards. The falls forward, left and right were generally more ambiguous in their cause, but may be due to improper leg placement.

The missed stance/swing transitions in the neuromuscular control were caused when subjects did not allow the leg angle to cross the  $90^\circ$  threshold set in stance/swing state machine (compare fig. 3.9). The missed stance 2/stance 3 transitions occurred with impedance control if the user did not dorsiflex the ankle sufficiently to trigger the transition. This could cause the knee to produce an extension torque in late stance, making it difficult to enter the swing phase (compare fig. 6.2).

As shown in fig. 6.7, the rate at which the impedance controller

Table 6.2: Tally of observed reasons for falls across all subjects and across both the undisturbed and disturbed walking conditions. Falls were manually classified based on video and logged prosthesis data. An individual Fall can be assigned more than one reason.

failed to transition through all three stance phases significantly increased with the introduction of disturbances.

In contrast, the knee collapse fall type was triggered with impedance control if the user dorsiflexed the ankle too early causing a premature switch to the third phase of stance. In this phase, knee torque typically trends towards zero to allow for passive flexion of the knee heading into swing. However, in the case of a premature switch to the push-off phase, these near-zero knee torques can cause the knee to suddenly collapse under the user's weight.

The last cause of falls, trips during swing, occurred when using both controllers, but 3x more often with impedance control than with neuromuscular control. Many of the swing trips for impedance control were also preceded by a missed stance 2/stance 3 transition. Others occurred when kinematics were drastically changed by the disturbance. For example, several swing trips occurred after a sudden acceleration of the treadmill caused the stance step length to dramatically increase, thereby altering kinematics at toeoff and in swing, and leading to the toe hitting the ground mid-swing.

Finally, we look at the effect of using suboptimal controllers on user ratings and falls. Figure 6.9 shows the median ratings of each the preferred and suboptimal parameters for each controller. For neuromuscular control, we see no significant difference between the preferred controller from day 4 and the suboptimal controllers. In fact for the neuromuscular control with disturbances, 4 out of 5 users slightly preferred the suboptimal control from day 5. On the whole, choosing a suboptimal set of parameters seemed to have a larger effect on impedance control with 4 out of 5 subjects preferring the optimal to suboptimal without disturbances and all five subjects preferring the optimal impedance parameters to the suboptimal parameters in disturbed case.

Figure 6.9 shows the median number of falls garnered by optimal

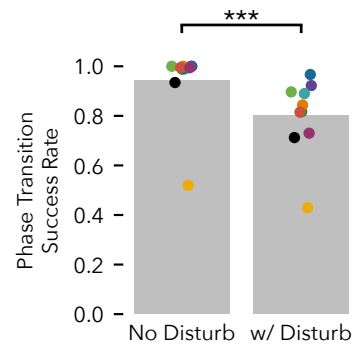


Figure 6.7: Fraction of steps for which impedance control successfully transitions through all three stance phases. Introduction of gait disturbances significantly decreases the transition success rate. Grey bars show the mean success rate across all users. Statistical significance assessed by Welch's *t*-test. \*\*\*:  $p < 0.001$ .

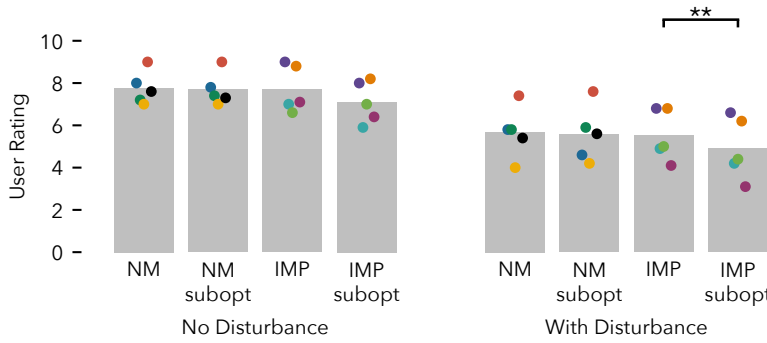


Figure 6.8: Comparison of user scores of optimal versus suboptimal parameters for the neuromuscular and impedance control strategies. Grey bars show the mean user rating across subjects. Statistical significance assessed by Welch's *t*-test. \*\*:  $p < 0.01$ .

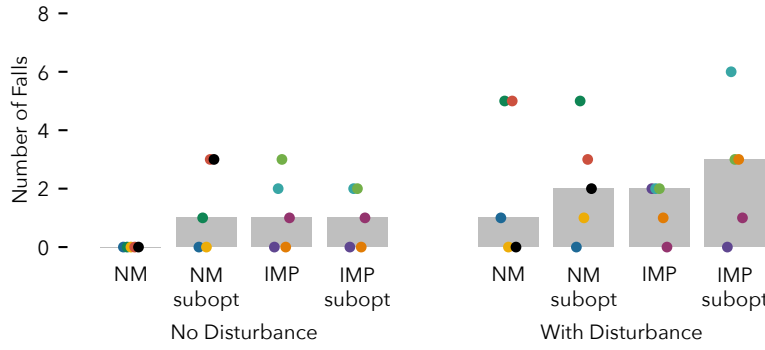


Figure 6.9: Comparison of number of falls of optimal versus suboptimal parameters for the neuromuscular and impedance control strategies. Grey bars show the median number of falls across subjects. Statistical significance assessed by Wilcoxon signed-rank test.

and suboptimal parameters. In the disturbance case we see a increase in the median number of falls with the suboptimal parameter sets over the preferred parameter sets. However this difference was not significant.

#### 6.4 Discussion

In this work, we sought to objectively compare the robustness and user preference of the neuromuscular and impedance control strategies for powered, robotic knee and ankle prostheses. Overall, we found that users rated the neuromuscular control more highly than impedance control and using impedance control led to significantly more falls compared to walking without a prosthesis. While the median number of falls accrued by impedance control across all subjects in both the undisturbed and disturbed conditions was higher than those of neuromuscular control, these differences were not significant. The only measure of gait stability in which a significant difference between the neuromuscular and impedance controllers was measured was the torso pitch variability, which neuromuscular control significantly reduced in the disturbance case compared to impedance control.

Categorizing the falls by their type gives more insight into differences between the controllers. There were reasons for falls with each controller that did not exist for the other. For NM control, missed transitions between stance and swing caused three falls. While these falls could be directly attributed to the leg-angle threshold in the high level state machine that governs the stance/swing state transition (fig. 3.9), that these falls only occurred with neuromuscular control suggests a causal difference in the two strategies. One possible important difference between the implemented neuromuscular and impedance control strategies was that impedance control typically

provided much more ankle push of work, as shown in fig. 6.10. In impedance control, the transition transition to the third phase of gait generates a large burst of ankle power, which users may interpret as a signal that the prosthesis is ready to enter swing. In contrast, neuromuscular control may not have provided any such signal due to the lack of ankle work. It is possible that such cues to the user should be explicitly considered in the design of prosthesis controllers, especially when they can help inform correct transition of discrete state.

Impedance control suffered from two failure modes specific to the structure of its stance finite state machine. The first failure mode, missed transitions between the second and third phases of stance, occurred if the user did not dorsiflex the ankle enough to trigger the transition. This failure often led to trips during swing or a later loss of balance. In contrast, the knee collapse failure mode happened if the impedance controller switched to the third phase of stance too early, which could cause a sudden reduction in knee extension torque. The fact that individual subjects fell for both of these reasons suggests that we cannot fix these failure modes by simply tuning the ankle angle threshold. Decreasing the threshold to prevent missed transitions would likely cause more knee collapses. Conversely, increasing the threshold would likely cause more missed transitions.

Finally, users suffered from trips during swing when using both stance control strategies, which were both paired with the same minimum-jerk trajectory generation swing control strategy. However, these trips occurred three times more frequently with impedance stance control than with neuromuscular stance control. Many of the trips that occurred with impedance control were preceded by a missed transition between the second and third stance phases. Neuromuscular control, in contrast, is smooth throughout stance with no discrete transitions, and thus may allow for a smoother transition to swing and fewer swing trips. Nonetheless, even with its smoother stance phase, subjects still tripped during swing several times with the Neuromuscular control. Therefore, in section 7.5 we seek to explicitly minimize the risk of falling by using an estimate of the current and future trajectories of the hip height and orientation to plan knee and ankle swing trajectories that avoid premature ground contact.

The smooth stance phase of the neuromuscular model, which eliminates failure modes such as knee collapses and missed stance phase transitions, and may help reduce swing trips, comes at the cost of dramatically increased model complexity. The implemented impedance controller has 20 parameters: 3 stance phases  $\times$  2 joints  $\times$  3 parameters per joint per phase + 2 transition parameters. In contrast, the implemented neuromuscular control is more than 4

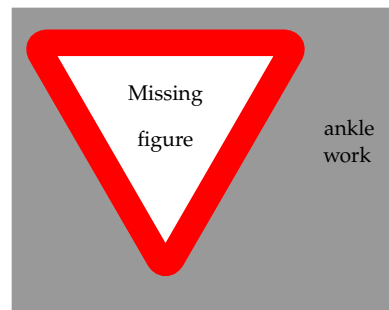


Figure 6.10: Normal Walking, impedance and neuromuscular control ankle work.

times as complex as it has 80 parameters: 54 defining muscle-specific mechanical properties, 9 defining shared muscle properties, and 17 defining the neural reflexes.

Of these 80, we chose to only optimize 18 when generating parameter sets in order to avoid local minimum and to complete the optimization in a reasonable amount of time. The choice of which 18 parameters to choose was based on trial and error. In the clinical setting, this lack of transparency about the function of and interdependencies between these 80 parameters may make practical application of neuromuscular control difficult. Therefore, in order to achieve the potential benefits of a smooth controller that does not have discrete stance phases, while avoiding excessive complexity, in chapter 8, we explore an alternative approach to stance control. This approach relies on a continuous estimate of phase and easily interpretable models for the output behavior as a function of phase.

A surprising result of this experiment is the lack of substantial differences between suboptimal and optimal controllers. Only in the case of impedance control under disturbances did the user unanimously restate their preference for the control parameter sets they had preferred on the optimization day. The lack of clear differences between the neuromuscular parameter sets could be the result of the neuromuscular model generally being less sensitive to its parameters than the impedance controller. For example, large differences in behavior between impedance control parameter sets can result if one set of parameters causes many missed phase transitions and another parameter set does not. Another reason for the lack of clear difference in user ratings could be the difference in the query. During the optimization procedure, subjects were asked to directly prefer one controller to other after short  $\sim 10$  sec bouts of walking on each control. In contrast, on the data collection day, controllers were independently rated on a 1-10 scale after 2 minutes of walking. In future work, we should check for consistency of the preferred parameters by performing the dueling bandits optimization procedure on multiple days in order to see if the users preferences are consistent from day to day.

Finally, our simulated results presented in chapter 4 predicted a larger difference between controllers that was not borne out by this experiment. In future work, the motion capture data collected during these trials should be used to improve the neuromuscular model so that researchers can perform experiments investigating prosthetic device performance with a higher likelihood that those results translate to the real world. Such predictive models would vastly reduce the time it takes to iterate on prosthesis controllers.

# 7

## *Reactive Swing Control for Trip Avoidance*

### *7.1 Classification Approach Introduction*

Avoiding obstacles on the ground is a necessity for maintaining safety while performing a variety of locomotion tasks. This behavior requires anticipation of an obstacle and active leg control strategies to avoid it [Patla and Prentice, 1995]. Transfemoral amputees, however, have a compromised ability to negotiate obstacles, as shown in Figure 7.1, as current prosthesis technology relies on mechanically passive knees that necessitate significant compensation at the hip in order to replicate able-bodied trip recovery strategies [Shirota et al., 2015]. Compromised ability to avoid and recover from trips may contribute to the large number of falls that leg amputees suffer. For instance, 58% of unilateral amputees reported a fall within a year [Kulkarni et al., 1996]. Moreover, the fear of falling can cause amputees to avoid activity, leading to further deterioration of their physical condition [Miller et al., 2001].

An increasing availability of powered prostheses in research labs provides the opportunity to study active obstacle avoidance strategies in prosthetics, although so far only a limited number of studies exist on this topic. These studies focus on detecting and classifying the correct response strategy after the amputee has tripped. For example, Lawson et al. [2010] developed a classifier that uses fast Fourier transform and the root mean square of accelerometer data as features to classify stumbles and recovery strategies, respectively. Zhang et al. [2011a] found that adding EMG signals from the residual limb to accelerometer data can help reduce false positives for stumble and strategy detection. Finally, Shirota et al. [2014] identified the optimal sliding window lengths and increments for feature calculation for trip detection and strategy selection classifiers. While detecting and classifying trip recovery strategies after their occurrence is a necessary step towards obstacle avoidance, it does not provide a proactive prosthesis control strategy that prevents obstacle encounters in the



first place.

Another major drawback of the previous studies is that they train and test the classifiers offline. However, a deployed trip classifier needs to function online and deal with temporal adaptation of the learner and amputee. The adaptation is required as the obstacle avoidance behavior triggered by a trip classifier alters the amputee's movements and, therefore, the data used to train the classifier. Consequently, trip classifiers trained offline may be ineffective due to the mismatch of training and testing data, a common problem faced in imitation and reinforcement learning [Ross et al., 2011].

Here we present the first pilot study that combines online learning and proactive control of a powered transfemoral prosthesis to implement obstacle avoidance in amputee locomotion. The obstacle avoidance system uses early-swing measurements of the residual limb angle, angular velocity, and linear acceleration to recognize in-process obstacle avoidance attempts. To address the online learning aspect of this system, we adapted a previously proposed algorithm for detecting gait modes [Spanias et al., 2018]. We also changed the existing swing leg behavior of the prosthesis to facilitate obstacle avoidance. This change includes a regression to predict the appropriate degree of knee and ankle flexion given the user's previous obstacle response motions. Finally, we evaluated the system behavior in trials with both non-amputee and amputee subjects.

Figure 7.1: a) Utilizing minimum jerk trajectories during swing does not allow for appropriate adaptation of swing trajectories to enable obstacle avoidance. b) Our adaptive system learns online to detect the presence of an obstacle from the amputee's late stance/early swing movements. Once detected, the controller modifies the trajectories of the knee and ankle to achieve improved obstacle clearance.

## 7.2 Classification Approach Methods

### 7.2.1 Forward-Backward Classifier

In order to learn to classify trips online with minimal hand-labeling of data, we rely primarily on the forward-backwards classifier approach first proposed by Spanias et al. [2018] for the purpose of classifying different modes of gait such as level ground walking, standing, and stair climbing. In their work, a *forward classifier* predicts the next step's gait mode using data in a window shortly before the transition. In parallel, a *backward classifier* labels completed steps with their correct gait mode in hindsight. Because the backwards classifier has access to features from the completed step, it can achieve accurate labels with a small amount of hand-annotated data. Once trained, the backwards classifier can provide labels for training the forward classifier, obviating the need for further hand-labeling of steps.

In our work, the forward classifier predicts, shortly after toe-off, if the upcoming swing will require obstacle avoidance or not. For this purpose, we use a linear support vector machine and features of the residual limb motion in the last 210 ms of stance and first 90 ms of the swing phase. Because user behavior changes over time in response to changes in prosthesis obstacle avoidance behavior, we retrain the forward support vector machine every ten steps using labels from the backward classifier.

The backward classifier is another linear support vector machine, trained once for each user, which uses features extracted from the entire swing phase to label a step as an avoidance attempt after the fact. To train the backwards classifier we hand label obstacle avoidance attempts and normal steps for roughly ten obstacles.

Figure 7.2 provides an overview of this system.

### 7.2.2 Target Knee Angle Regression

A prosthesis user will not always encounter obstacles of the same height. As the obstacle avoidance response can be disruptive to the user, it is desirable to give the user control over the magnitude of the prosthesis response. We seek to achieve this functionality by using the normalized backward classifier score as a metric for the difficulty of avoiding an obstacle. We then implement a simple linear feedback law that assigns higher target flexion knee angles to obstacle avoidance attempts that are more difficult according to this metric. Figure 7.3 outlines this feedback mechanism, which has the

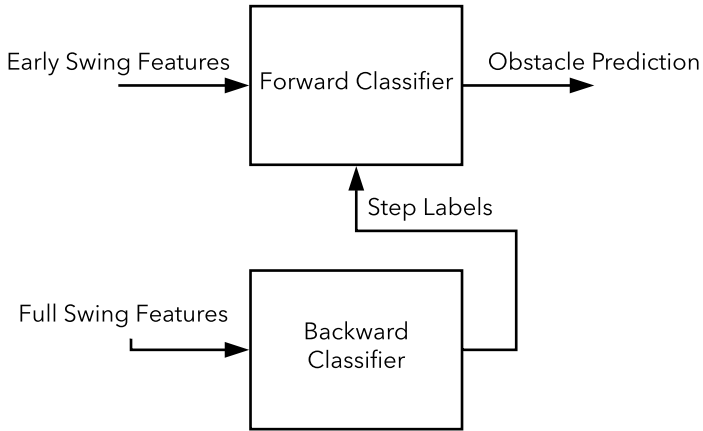


Figure 7.2: Forward-Backward Classifier Overview. The backwards classifier uses features from the entire swing to provide training class labels to a forwards classifier. The forwards classifier uses features from late stance and early swing in order to predict if an upcoming swing will be an obstacle avoidance attempt.

form

$$\theta_{n+1}^{tgt} = \theta_n^{tgt} - k_{decay}(\theta_n^{tgt} - \theta_{min}) + k_{score}\hat{\xi}, \quad (7.1)$$

$$\hat{\xi} = \frac{\xi - \xi_{10^{\text{th}} \text{ percentile}}}{\xi_{90^{\text{th}} \text{ percentile}} - \xi_{10^{\text{th}} \text{ percentile}}}, \quad (7.2)$$

where  $\theta_{tgt}$  is the current target angle for a given set of features,  $n$  is the current time step,  $k_{decay}$  is a gain that prevents continual target angle growth by decaying target angles towards  $\theta_{min}$ , and  $k_{score}$  is a gain on the normalized class score,  $\hat{\xi}$ . The system shifts class scores,  $\xi$ , so that scores below the 10<sup>th</sup> percentile of tripped step scores result in a reduction of the target knee angle. Furthermore, the system normalizes the scores by  $\xi_{90^{\text{th}} \text{ percentile}} - \xi_{10^{\text{th}} \text{ percentile}}$  so that the gain  $k_{score}$  has a predictable effect across subjects whose score ranges vary.

The system fits the target knee angles with a linear support vector regression. Every time the trip avoidance triggers, it appends an additional target angle, specified by eq. (7.1), to a training data set. The system retrains the regression using this data set every ten trip-avoidance steps.

### 7.2.3 Feature Extraction

For the forwards and backwards classifiers, as well as the target knee angle regression, we use features of the thigh angle, angular velocity, and linear accelerations in a time window. Specifically, we use the mean, standard deviation, minimum value, and maximum value of each signal. For forward classification and regression the time window begins 210 ms before toe-off and ends 90 ms after toe-off, while for the backward classification we use a window consisting of the entire swing phase between toe-off and heel strike.

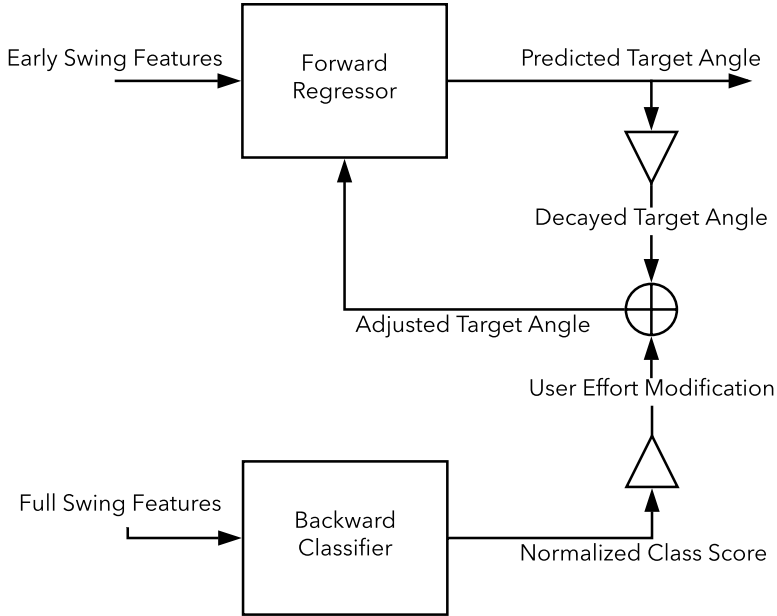


Figure 7.3: Knee Angle Regression Feedback. In order to enable volitional control of the knee and ankle flexion angles to allow users to achieve greater flexion angles for larger obstacles, we implement a feedback system that uses the backwards classifier class score to quantify obstacle difficulty. After each step, the system increases the desired target angle for that step's forward features proportionally to the normalized back classifier score. We also decay the current desired target angle for those features to prevent continual growth of the target angle. The regression is retrained every ten avoidance attempts.

#### 7.2.4 Trajectory Planning

To generate the knee and ankle motions for unperturbed swing, we follow the method proposed by Lenzi et al. [2014] to generate and follow human-like minimum jerk trajectories that start at the toe-off state of each joint (angle, angular velocity, and angular acceleration), go to a target flexion state, and then extend to desired final angles at the estimated heel strike time. We estimate the swing period to be 65% of the stance period.

When the forward classifier triggers an obstacle avoidance attempt, we switch to bang-bang trajectories for the knee and ankle joints. These trajectories maximize foot clearance while respecting joint angle, velocity, and acceleration limits. The bang-bang trajectories achieve desired flexion angles as quickly as possible and then extend as late as possible such that they achieve extension before the predicted heel strike time. The trajectory planner uses the target knee angle regression to determine the appropriate peak angle for the knee trajectory, while the ankle trajectory's target flexion angle is a linear function of the knee's target angle. The knee trajectory's peak flexion angle is constrained to lie within 65 and 90 degrees while the peak ankle flexion is constrained within 5 and 15 degrees. Examples showing the minimum jerk swing trajectories and obstacle avoidance trajectories planned for large and small obstacles are given in fig. 7.4.

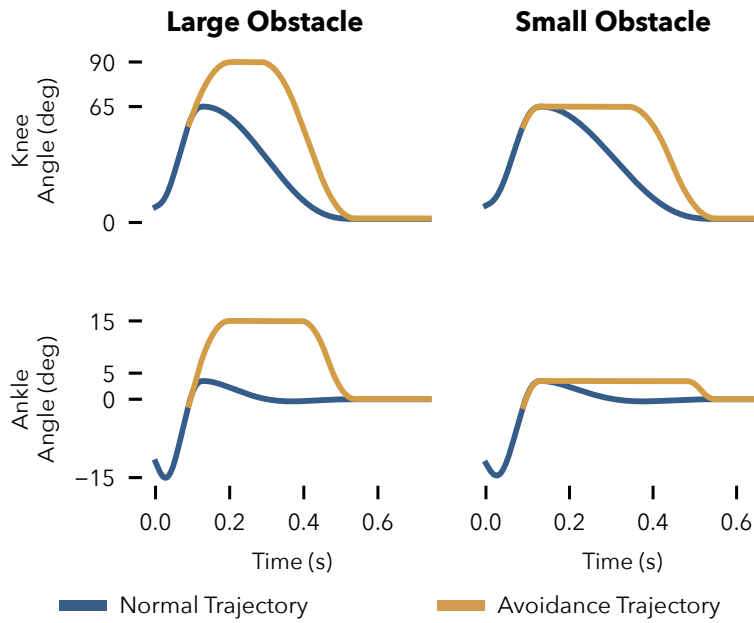
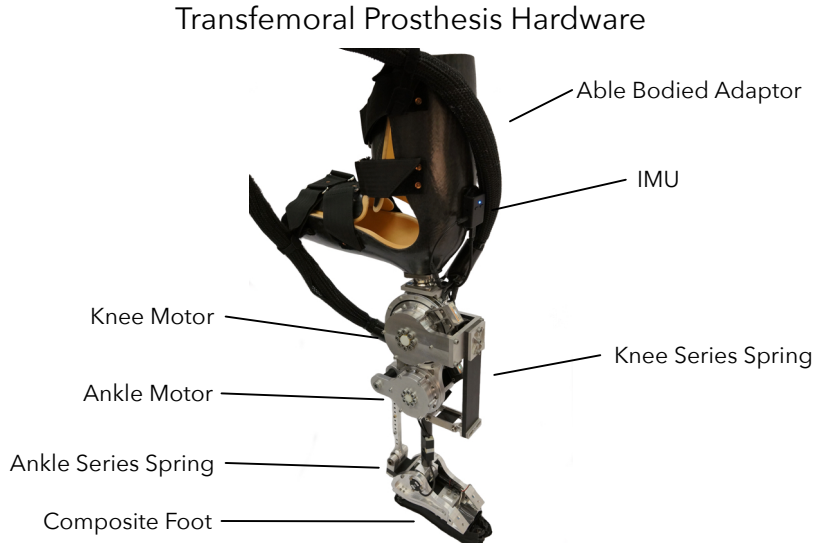


Figure 7.4: Bang-bang obstacle avoidance trajectories (yellow) vs normal minimum jerk trajectories (blue) for the knee and ankle.

### 7.2.5 Experimental Protocol

We tested the ability of the proposed online learning system to accurately classify trips and normal swings, help subjects avoid tripping on obstacles, and modulate knee and ankle flexion appropriately for obstacles of different heights. To evaluate these aspects of system performance, we conducted experiments with a powered knee and ankle prosthesis shown in fig. 7.5 (previously described in Thatte et al. [2018]).

Two subjects, one non-amputee with prior experience using this prosthesis, and one inexperienced amputee subject, performed walking trials with the obstacle avoidance system enabled. As subjects walked, an experimenter placed objects on the treadmill belt in front of each subject's prosthetic leg, necessitating an obstacle avoidance reaction. To obtain a baseline performance level for non-reactive prosthetic swing control, we also performed obstacle avoidance trials with the minimum jerk swing trajectories designed for undisturbed swing. Before the online trials, the backwards classifier was trained for the prosthesis user with 75 steps. The able bodied subject completed 446 total steps, with 53 box avoidance steps, while the amputee completed 222 total steps, with 40 box avoidance steps. The amputee subject performed trials in an ABBA order, where A is minimum jerk control and B is the reactive control, in order to average out potential learning effects. The amputee subject also had an additional practice session the day prior to the box avoidance trials in which he



acclimated to walking with the powered prosthesis without obstacles.

### 7.3 Classification Approach Results

#### 7.3.1 Results

Tables 7.1 and 7.2 show the overall classification accuracies, sensitivities, and specificities for the forward and backwards classifiers for the able-bodied and amputee subjects respectively. The forward and backwards classifiers for both subjects achieve high specificity (the number of normal steps classified correctly) and accuracy (> 95%). The sensitivity, the percentage of true trips classified correctly, of the classifiers for both subjects is substantially lower than the specificity or accuracy. For the forward classifier, we see that because the model is trained online, the sensitivity improves from the first half of the trial to the second half, which explains some of the low overall sensitivity.

Controller	Classification Accuracy	Sensitivity	Specificity
Forward, 1 <sup>st</sup> Half	96%	73% *	99%
Forward, 2 <sup>nd</sup> Half	99% *	93% *	99%
Forward Overall	98%	85% *	99%
Backward	99%	100%	99%

Importantly, the ability of the forward classifier to correctly trigger the bang-bang obstacle avoidance trajectories improves obstacle avoidance success rates as shown in table 7.3. Both subjects were

Figure 7.5: Our powered transfemoral prosthesis prototype features series elastic actuators at both the knee and ankle joints for accurate torque control. We mount an IMU (3-Space Sensor, Yost Labs) to the thigh in order to measure hip angle and angular velocity and thigh linear accelerations. Able-bodied subjects wear the prosthesis via an L-shaped adapter (shown), whereas amputee subjects can attach the prosthesis to their personal socket via a standard pyramid adapter.

Table 7.1: Classifier Performance <sup>1</sup>, Able-Bodied Steps: 446, Avoidance Attempts: 53

<sup>1</sup>\*  $\implies p < 0.05$ , \*\*  $\implies p < 0.01$ , \*\*\*  $\implies p < 0.001$ , Chi-squared test

Controller	Classification Accuracy	Sensitivity	Specificity
Forward, 1 <sup>st</sup> Half	95%	80%	98%
Forward, 2 <sup>nd</sup> Half	96%	85%	98%
Forward Overall	95%	83%	98%
Backward	98%	90% *	99%

able to avoid significantly more obstacles with the obstacle avoidance controller than with the minimum jerk trajectory controller.

Controller	Able-Bodied Success Rate	Amputee Success Rate
Minimum Jerk	37% *	35% *
Adaptive Bang-Bang	89%	71%

We also compared our online learning approach for obstacle avoidance to an offline approach similar to that taken by Lawson et al. [2010], Zhang et al. [2011a], and Shirota et al. [2015]. To do this, we trained a classifier offline using the first half of the amputee subject's bang-bang control data and tested it on the second half of the data. Table 7.4 shows that the classifier trained offline has trouble generalizing to the second half of the data, as it performs significantly worse than the online-trained model in terms of accuracy and sensitivity.

Classifier	Classification Accuracy	Sensitivity	Specificity
Offline	89%	39% *	100%
Online	95% *	83%	98%

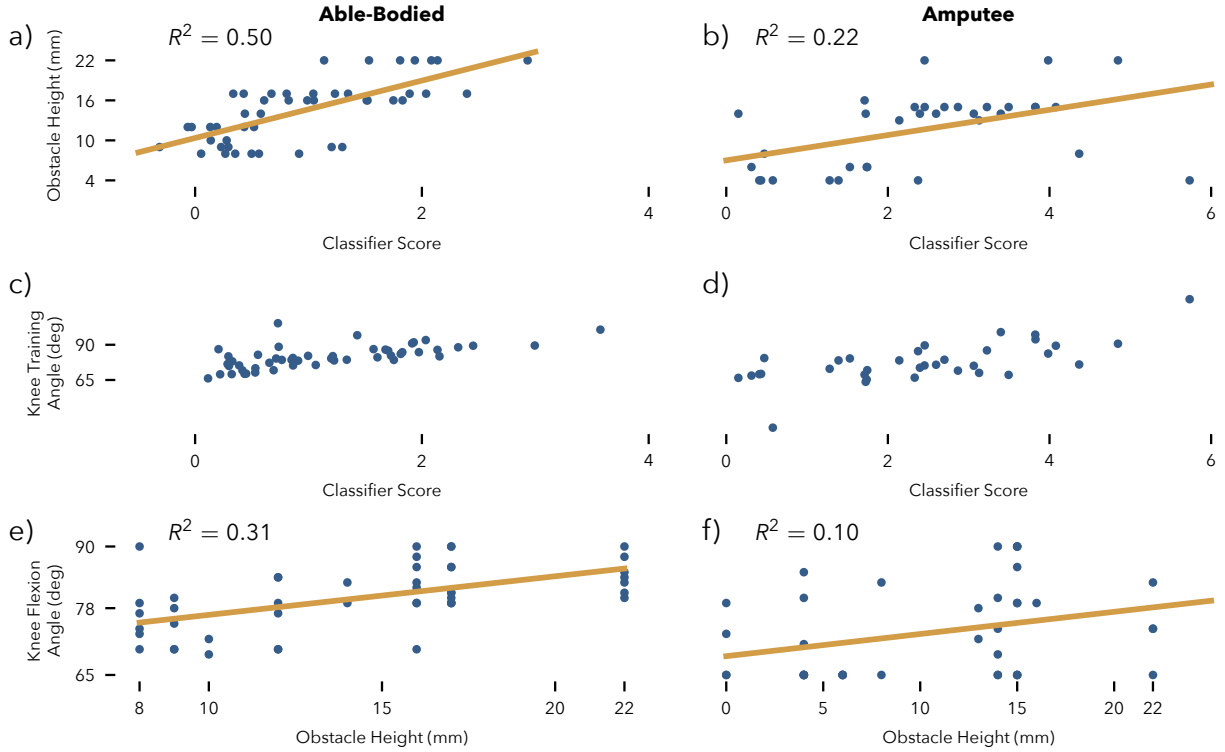
Finally, we examined the ability of the knee angle regression to choose a target knee angle that is appropriate for the object size. The feedback law proposed in eq. (7.1) assumes we can use the backwards classifier score as a metric of obstacle difficulty. For the able-bodied subject, this assumption seems warranted, as there is a strong relationship between the obstacle height and the classifier score (fig. 7.6a,  $R^2 = 0.50$ ). However, for the amputee subject, who was less experienced with walking with the powered prosthesis, this relationship is less clear (fig. 7.6B,  $R^2 = 0.22$ ).

As shown in fig. 7.6c&d, our system is able to ensure that high classification score steps, associated with high user effort, obtain larger target flexion angles. This relationship led to noisy volitional control of the knee flexion angle for the able-bodied subject (fig. 7.6e) as evidenced by the linear relationship between knee angle and obstacle height ( $R^2 = 0.31$ ). However, for the amputee subject, there is no clear relationship between the obstacle height and knee flexion angle (fig. 7.6f,  $R^2 = 0.10$ ).

Table 7.2: Classifier Performance, Amputee, Total Steps<sup>1</sup>: 222, Avoidance Attempts: 40

Table 7.3: Obstacle Avoidance Success Rates<sup>1</sup>

Table 7.4: Online and Offline Forward Classifier Performance, Amputee<sup>1</sup>



#### 7.4 Classification Approach Discussion

We developed an online learning system to help users of powered transfemoral prostheses avoid obstacles. Our system uses information from an inertial measurement unit during the late stance to early swing period to classify the upcoming swing as either normal or a trip avoidance attempt. Unlike previous work on obstacle negotiation for transfemoral prostheses [Lawson et al., 2010, Zhang et al., 2011a, Shirota et al., 2014], our system learns online on an actual transfemoral prostheses. We compared the classification performance of our online system with a hypothetical offline system using online trials to provide testing and training data for offline analysis. This comparison showed that the online learning system provided an improvement in sensitivity and accuracy to obstacle avoidance attempts. Both an experienced, able-bodied subject and an inexperienced, amputee subject were able to improve their obstacle avoidance success rates significantly. However, only the experienced, able-bodied subject was able to achieve some level of volitional control of the prosthesis flexion as a function of obstacle height.

There are several reasons why the amputee subject may not have

Figure 7.6: Obstacle height vs backwards classifier score for (a) the able-bodied and (b) amputee subjects. The system uses the backwards classifier score as a metric for obstacle avoidance difficulty. This score is used in a feedback loop that forms the training set for the flexion target angle regression (c-d). With this feedback system, the able bodied user (e) is able to achieve a degree of volitional control over flexion angle as evidenced by the linear relationship between knee flexion angle and obstacle height ( $R^2 = 0.31$ ). However, the amputee (f) was not able to achieve meaningful control over the flexion of the prosthesis ( $R^2 = 0.10$ ), possibly due to the decreased experience level of this subject.

been able to achieve volitional control of prosthesis flexion. First, the amputee had far less experience using the prosthesis than the able-bodied subject. Consequently, even though both subjects were informed that trying harder to lift the leg over bigger obstacles would likely lead to greater flexion once the prosthesis learns, it is likely that only the first subject was able to incorporate and implement this information. The amputee may have concentrated on more rudimentary aspects of gait, as evidenced by his use of the handrails to walk, whereas the able-bodied subject did not need to use the hand rails. Moreover, the amputee's socket may have provided less control over the prosthesis than did the intact subject's able-bodied adapter (shown in fig. 7.5). Finally, we noted that the relationship between joint flexion and obstacle height tended to oscillate over the course of our trials. This may imply that the gains we used for the target knee angle regression (eq. (7.1)) were too high.

Before settling on the specifics of the obstacle avoidance system presented here, we also tested other options for its components. For example, we also evaluated incorporating EMG signals from the non-prosthetic limb in our obstacle avoidance classifier. Previous research showing that able-bodied subjects utilize stance leg musculature to help raise the hip during obstacle avoidance motivated this choice of EMG placement [Patla and Prentice, 1995]. However, as was found by Spanias et al. [2018], using EMG data along with mechanical data in the forwards-backwards online learning algorithm did not seem to improve classification accuracy, which is already high. This lack of improvement may also result from a significant delay in our wireless EMG sensors (Delsys Trigno). It is possible that a low-latency wired EMG sensor would be able to improve classification performance or the performance of the target angle regression.

We also tried using imitation learning techniques to model able-bodied strategies for stepping over obstacles. Specifically, we employed maximum margin inverse optimal control [Ratliff et al., 2007] to learn, offline, cost functions for the knee that explained obstacle avoidance trajectories. However, when used online, the generated trajectories tended to diverge and produce unexpected results because the initial toe-off state of the prosthesis did not match those in the able-bodied data set. For the obstacle avoidance classifier, we correct this sort of offline-online mismatch via the backwards classifier that provides labels to train the forwards classifier online. It is less clear how to update trajectories in hindsight as we never see the obstacle. For this reason, we used bang-bang trajectories during obstacle avoidance, which maximize the time the joints remain flexed.

In the future, we plan to overcome this issue by incorporating a laser distance sensor into the prosthesis. This sensor should allow

precise measurement of the ground and obstacle shape during the initial part of swing as the hip moves forward. We plan to then use this information to explicitly plan knee and ankle trajectories that will avoid the obstacle and the floor until the appropriate touch down time.

There are several other limitations of the current study we should address in future work as well. First, we only tested the algorithm with two subjects. More subjects of varying skill levels are necessary to determine how applicable the system is to a broader population. Additionally, a likely reason why the forward classifier's sensitivity was relatively low, was that there were many more normal steps than obstacle avoidance attempts in the training data set. This may cause the SVM loss function's minimum to focus more heavily on classifying normal steps correctly. Deploying this system on a commercial prosthesis, for which trips are more rare, would exacerbate this issue. Therefore, future development should investigate how to train a classifier given heavily unbalanced class frequencies.

### *7.5 Planning Approach Introduction*

Lower limb amputees using state of the art commercial prostheses face a number of gait deficiencies that negatively impact their quality of life [Gauthier-Gagnon et al., 1999]. Of acute significance among these deficiencies are the increased risk of falling and the related injuries, which can lead to amputees avoiding activity out of a fear falling [Miller et al., 2001]. As falls and their avoidance are linked to swing leg placement in locomotion, active swing control strategies could help to substantially reduce the risk of falling. However, current swing controllers of transfemoral prostheses do little to proactively minimize this risk.

Existing swing phase control approaches for powered prostheses predominantly seek to reproduce the average swing phase behavior of the human leg. Whether the approach is based on trajectory planning [Lenzi et al., 2014], impedance control [Sup et al., 2009], or phase-based control [Quintero et al., 2016], they all treat the swing phase motion as an “open loop” problem with respect to trip hazards, as none of the approaches take the location of the heel and toe of the prosthetic foot with respect to the ground explicitly into account. Therefore, current swing control strategies neglect a clear advantage that robotic prostheses can have over their passive counterparts: the ability to sense and act upon environmental information.

In this work, we develop a swing control strategy to reactively avoid trips with powered transfemoral prostheses that uses visual information about the environment and an estimate of the prosthesis

configuration. Some previous studies have explored incorporating visual feedback into the control of leg prostheses. For example, Scandaroli et al. [2009] developed a state estimator and controller that allowed the ankle joint of a prosthesis to conform to the slope of the ground under the foot. To address the problem of terrain recognition, Zhang et al. [2011b] developed a classifier using a LIDAR and an IMU to discriminate between terrains such as flat ground and steps. More recently, Liu et al. [2016] combined this terrain classifier with a Bayesian intent classifier (based on [Du et al., 2012]) to develop an environment-aware locomotion mode recognition system. In addition, RGBD sensors have been explored as a source of rich environmental information for legged assistance, including gait recognition [Mas-salin et al., 2017] and stair detection [Krausz et al., 2015, Duan et al., 2018]. However, none of these previous studies have implemented a control strategy that uses environmental information to reactively govern the motion of a powered prosthesis in real-time.

We present such a real-time reactive control of a powered prosthesis that combines three building blocks. First, we use an extended Kalman filter (EKF) that fuses measurements from an IMU, a LIDAR, and encoders on the prosthesis to estimate the current pose of the prosthetic leg with respect to the ground. Second, we predict likely future leg trajectories with sparse Gaussian process models learned online during swing. Finally, we use the leg pose estimate and trajectory predictions in a fast quadratic-program planner to reactively generate in real time leg joint trajectories that avoid premature toe and heel contact with the ground. To evaluate the proposed control, we compare our method for trip avoidance to a standard non-reactive minimum-jerk trajectory planning approach in a prosthesis walking experiment designed to elicit trips.

## 7.6 Planning Approach Methods

The trip avoidance control we propose involves (1) estimating the position and orientation of the leg (section 7.6.1), (2) predicting the future hip angles and heights (section 7.6.2), and (3) planning corresponding knee and ankle trajectories such that the heel and toe will not contact the ground prematurely (section 7.6.3).

### 7.6.1 Extended Kalman Filter for estimating Leg Position/Orientation

To estimate the position and orientation of the leg, we employ an EKF that fuses information from a LIDAR distance sensor (SICK OD1000), an IMU (YEI Technologies 3-Space sensor), and encoders on the prosthesis (Renishaw Resolute, Netzer DS-25). The EKF filters the

nonlinear, discrete-time dynamics given by

$$\begin{aligned} \mathbf{x}_t = \begin{bmatrix} q_t \\ p_t \\ \dot{p}_t \end{bmatrix} &= \begin{bmatrix} f_{\text{gyro}}(\omega_t) & 0 & 0 \\ 0 & I_{3 \times 3} & \Delta t I_{3 \times 3} \\ 0 & 0 & I_{3 \times 3} \end{bmatrix} \mathbf{x}_{t-1} \\ &+ \begin{bmatrix} 0 \\ \frac{1}{2} \Delta t^2 I_{3 \times 3} \\ \Delta t I_{3 \times 3} \end{bmatrix} \left[ R_{\text{OI}}(q_{t-1}) \mathbf{a}_t - \begin{bmatrix} 0 \\ 0 \\ g \end{bmatrix} \right] + w_t \quad (7.3) \\ &= f(\mathbf{x}_{t-1}, \mathbf{u}_t) + w_t, \end{aligned}$$

where  $q$  is the quaternion orientation,  $R_{\text{OI}}$  and  $p$  are the rotation matrix and position of the IMU in inertial coordinates,  $\omega$  is the angular rate measured by the gyroscope,  $f_{\text{gyro}}$  integrates the gyroscope rate to update the orientation,  $a$  is the accelerometer measurement,  $\mathbf{u}_t = [\omega_t, \mathbf{a}_t]^T$ , and  $\Delta t$  is the integration time step (1 ms).

The dynamics are corrupted by process noise  $w_t \sim \mathcal{N}(0, Q_t)$  due to the inaccuracy of the IMU's measurement of the true acceleration and angular velocity. Consequently,  $Q_t$  is given by

$$Q_t = \frac{\partial f}{\partial u} \Big|_{x_{t-1}, u_t} \begin{bmatrix} \sigma_\omega^2 I_{3 \times 3} & 0 \\ 0 & \sigma_a^2 I_{3 \times 3} \end{bmatrix} \frac{\partial f}{\partial u} \Big|_{x_{t-1}, u_t}^T, \quad (7.4)$$

where  $\sigma_\omega^2$  and  $\sigma_a^2$  are the gyroscope and accelerometer measurement variances, respectively.

To estimate the pose given our sensor measurements, we follow a standard EKF procedure [Anderson and Moore, 1979], reviewed here for completeness. The EKF state estimation process has two steps: First, we *predict* the next state distribution by forward-propagating the mean  $\hat{x}_{t-1|t-1}$  and covariance of the state estimate  $\Sigma_{t-1|t-1}$  using the dynamics given by eq. (7.3),

$$\hat{x}_{t|t-1} = f(\hat{x}_{t-1|t-1}, \mathbf{u}_t) \quad (7.5)$$

$$\Sigma_{t|t-1} = F_t \Sigma_{t-1|t-1} F_t^T + Q_t, \quad (7.6)$$

where  $F_t = \partial f / \partial x|_{\hat{x}_{t-1|t-1}}$ .

Next, we incorporate information from noisy sensor observations to *update* the state estimate. To do this, we utilize a observation model given by  $z_t = h(x_t) + v_t$ , where  $v_t \sim \mathcal{N}(0, R)$ , and the following update equations:

$$K_t = \Sigma_{t|t-1} H_t^T \left( H_t \Sigma_{t|t-1} H_t^T + R \right)^{-1} \quad (7.7)$$

$$\hat{x}_{t|t} = \hat{x}_{t|t-1} + K_t (z_t - h(\hat{x}_{t|t-1})) \quad (7.8)$$

$$\Sigma_{t|t} = (I - K_t H_t) \Sigma_{t|t-1} \quad (7.9)$$

where  $z_t$  are the actual sensor measurements and  $H_t = \partial h / \partial x|_{\hat{x}_{t-1|t}}$ .

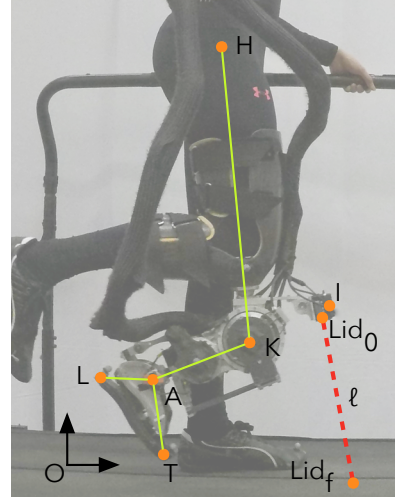


Figure 7.7: Kinematic model of the user and prosthesis used for state estimation and motion planning. The model includes the hip (H), knee (K), ankle (A), heel (L) and toe points (T). Additionally, the start ( $Lid_0$ ) and end ( $Lid_f$ ) points of the LIDAR beam (with length  $\ell$ ) are indicated. The IMU is located at point I. Both the LIDAR and IMU are mounted to the thigh portion of the powered knee-and-ankle prosthesis.

The observations in our EKF formulation use the kinematic model shown in fig. 7.7. We calibrate this model using ground truth data from a VICON motion capture system. In our application we incorporate three observations:

1. The expected acceleration vector points up in the global coordinate frame,

$$h_1(x_t) = \{R_{OI}(q)\}_{\text{row } 3} \quad (7.10)$$

$$z_1 = a \quad (7.11)$$

2. The expected LIDAR measurement given the position of the IMU,

$$h_2(x_t) = \left\{ \ell : \{p_{OLID_f}(x_t, \ell)\}_{\text{row } 3} = 0 \right\} \quad (7.12)$$

$$z_2 = \ell_{\text{meas}}, \quad (7.13)$$

where  $p_{OLID_f}$  is the location of the laser beam endpoint represented in the global coordinate system,  $\ell = \|\overrightarrow{LID_0 LID_f}\|$  is the modeled laser beam length, and  $\ell_{\text{meas}}$  is the actual measured LIDAR distance.

3. During stance, the toe point coincides with the origin (active 200 m/s after stance begins until toe-off)

$$h_3(x_t) = p_{OT}(x_t, \theta_k, \theta_a) \quad (7.14)$$

$$z_3 = [0 \ 0 \ 0]^T \quad (7.15)$$

where  $p_{OT}$  is the location of the toe in the inertial frame, and  $\theta_k$  and  $\theta_a$  are the measured knee and ankle angles.

The measurement noise for these observations is given by

$$R = \begin{bmatrix} \sigma_a^2 I_{3 \times 3} & 0 \\ 0 & \sigma_\ell^2 \end{bmatrix} \quad (7.16)$$

during swing and

$$R = \begin{bmatrix} \sigma_a^2 I_{3 \times 3} & 0 & 0 \\ 0 & \sigma_\ell^2 & 0 \\ 0 & 0 & \sigma_f^2 I_{3 \times 3} \end{bmatrix} \quad (7.17)$$

during stance. In these equations,  $\sigma_a^2$  is the accelerometer variance,  $\sigma_\ell^2$  is the LIDAR measurement variance, and  $\sigma_f^2$  is the foot position variance.

To further improve the EKF's state estimate, we enforce a number of constraints using the methods provided by Gupta and Hauser [2007]. Specifically, we enforce three equality constraints:

1. First, we require that the quaternion has unit norm

$$1 = q_1^2 + q_2^2 + q_3^2 + q_4^2. \quad (7.18)$$

2. Second, we prevent the yaw component of the orientation  $q$  from drifting. To do this, we convert the  $q$  to ZYX Euler angles and enforce  $\phi_z = 0$ ,

$$0 = \text{atan2} \left( 2(q_1 q_4 + q_2 q_3), 1 - 2(q_3^2 + q_4^2) \right). \quad (7.19)$$

3. Finally, during stance we further constrain the toe's  $x$  and  $y$ -coordinates to 0,

$$\begin{bmatrix} 0 \\ 0 \end{bmatrix} = \{p_{OT}(x_t, \theta_k, \theta_a)\}_{\text{rows 1 and 2}}. \quad (7.20)$$

In addition, we use inequality constraints to ensure the toe and heel do not penetrate the ground,

$$0 \leq \{p_{OT}(x_t, \theta_k, \theta_a)\}_{\text{row 3}}, \quad (7.21)$$

$$0 \leq \{p_{OL}(x_t, \theta_k, \theta_a)\}_{\text{row 3}}. \quad (7.22)$$

We enforce these constraints by solving the following quadratic program after each update step,

$$\hat{x}_{t|t}^{\text{proj}} = \underset{x}{\text{argmin}} \left( x - \hat{x}_{t|t} \right)^T \Sigma_{t|t}^{-1} \left( x - \hat{x}_{t|t} \right), \quad (7.23)$$

such that

$$A_{\text{eq}} x = b_{\text{eq}}, \quad (7.24)$$

$$A_{\text{ineq}} x = b_{\text{ineq}}, \quad (7.25)$$

where  $A_{\text{eq}}$ ,  $b_{\text{eq}}$ ,  $A_{\text{ineq}}$ , and  $b_{\text{ineq}}$  are derived from linearizing the equality and inequality constraints.

To identify the appropriate parameters of the Kalman filter, we collected ground truth training and testing kinematic data using a Vicon motion capture system and optimized the parameters of the EKF to minimize the error of the kinematic estimate. The parameters we optimized were the rotation of the LIDAR with respect to the hip, the translation between the LIDAR and the IMU, and  $\sigma_\omega$ ,  $\sigma_a$ ,  $\sigma_\ell$ , and  $\sigma_f$ .

Figure 7.8 shows an example of the resulting EKF estimates of the hip, knee, ankle, heel, and toe positions during swing (blue stick figure and traces) compared to the ground truth obtained from the motion capture system (yellow) and an EKF estimate without the LIDAR sensor information integrated (red). Over the entire test

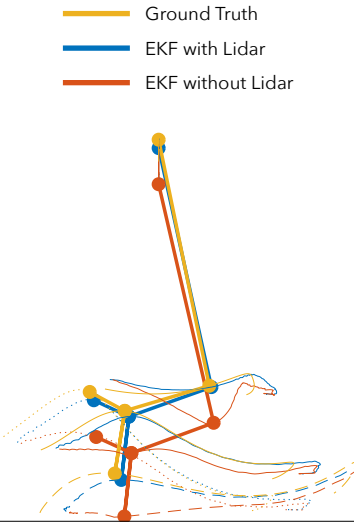


Figure 7.8: Trajectories of extended Kalman Filter (EKF) estimate of the position of the leg during swing (blue). Ground truth positions given by motion capture (yellow). EKF estimate without LIDAR information shown in red. Thick lines show the leg configuration at peak toe height during swing. Dotted lines indicate heel trajectories while dashed lines show the toe trajectories. Knee and ankle trajectories given by solid lines.

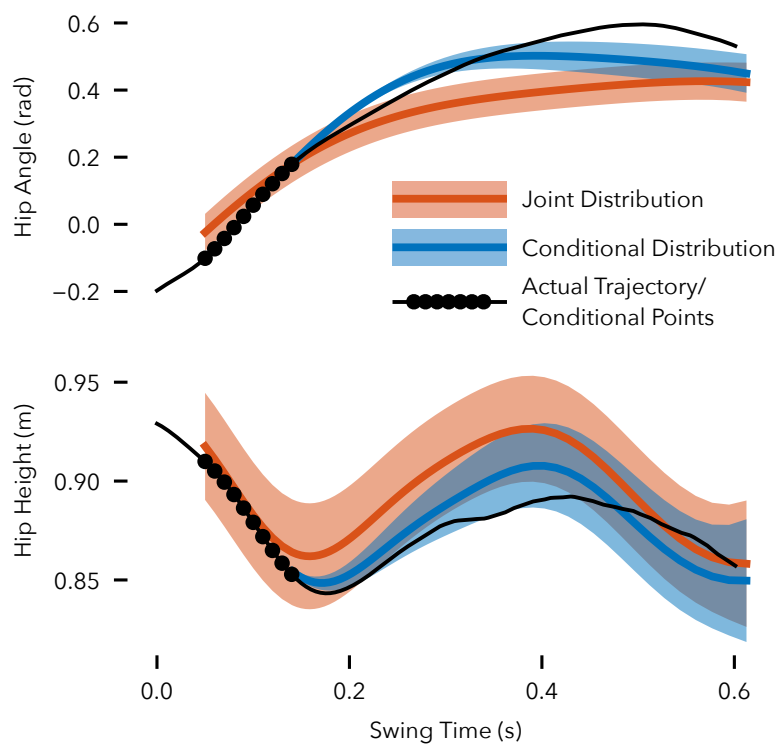


Figure 7.9: Example of hip angle and height trajectory predictions 0.15 s into swing. The prediction algorithm uses the previous 10 measured hip angles and heights (sampled at 100 Hz, black dots) along with the learned joint distributions of hip angles/heights versus time (red) to obtain the conditional distributions of future hip angles/heights (blue). The planning algorithm uses the means of the conditional distributions to generate knee and ankle trajectories. The actual hip height and angle trajectories are shown in black.

data set, the root mean squared error of the estimated heel and toe positions during swing is 18.6 mm for the EKF with LIDAR information. In contrast, the EKF without LIDAR information has an error of 46.7 mm. Thus, including the LIDAR sensor data reduces the error by 60%.

### 7.6.2 Gaussian Process Hip Trajectory Prediction

To predict the future hip angle and height trajectories, we train sparse Gaussian process models using the FITC approximation [Snelson and Ghahramani, 2007]. The sparse approximation ensures the computational complexity at test time is independent of the training data set size, providing consistent real time performance. Throughout the swing phase, the learned hip angle and height distributions are conditioned on the swing trajectories completed so far to predict the distribution of the future trajectories for the rest of the swing (example shown in fig. 7.9). Our algorithm then uses the means of these conditional distributions in the motion planning phase (compare section 7.6.3).

For example, to calculate the conditional mean of future hip

angles, we first compute the joint distribution of completed ( $\theta_h^c$ ) and future ( $\theta_h^f$ ) hip angles,

$$P(\theta_h^c, \theta_h^f) = \mathcal{N}(\mu_{\text{fitc}}, \Sigma_{\text{fitc}} + K(t_{\text{joint}}, t_{\text{joint}})) \quad (7.26)$$

$$= \mathcal{N}\left(\begin{bmatrix} \mu_c \\ \mu_f \end{bmatrix}, \begin{bmatrix} \Sigma_{c,c} & \Sigma_{c,f} \\ \Sigma_{f,c} & \Sigma_{f,f} \end{bmatrix}\right), \quad (7.27)$$

where  $\mu_{\text{fitc}}$  and  $\Sigma_{\text{fitc}}$  are obtained from equation 11 in [Snelson and Ghahramani, 2007] and  $K(t_{\text{joint}}, t_{\text{joint}})$  is an additional noise term given by a rational quadratic kernel [Rasmussen, 2004] that correlates the predicted angles across time, which results in smooth predicted trajectories. The mean of the conditional distribution  $P(\theta_h^f | \theta_h^c)$  is then given by

$$\mu_f^{\text{cond}} = \mu_f + \Sigma_{f,c} \Sigma_{c,c}^{-1} (\mu_c - \theta_h^c). \quad (7.28)$$

As the inversion of  $\Sigma_{c,c}$  is the most computationally expensive component of eq. (7.28), we use at most the last 10 hip angles and heights (sampled at 100 Hz) when calculating the conditional mean (compare fig. 7.9).

### 7.6.3 Trajectory Planning Quadratic Program Formulation

To obtain reactive control of the prosthesis swing leg motion, we plan future swing trajectories with a fast quadratic program (QP) operating at 100 Hz. The QP includes equality constraints, which ensure the trajectories progress smoothly from the current position to the desired end position, and inequality constraints, which avoid premature ground contact of toe and heel of the prosthesis. Because in our formulation the QP can only solve for one joint at a time, we first solve for the ankle trajectory assuming the knee trajectory found in the previous time step, and then use this updated ankle trajectory to solve for the new knee trajectory.

Figure 7.10 provides more details of the actions of the trajectory planner algorithm. For example, at a time of about 150 ms into the swing phase, the algorithm solves

$$\theta_k^{\text{toe bnd}} = \left\{ \theta_k : \{p_{\text{OT}}(\theta_h, z_h, \theta_k, \theta_a)\}_{\text{row } 3} = 0 \right\} \quad (7.29)$$

$$\theta_k^{\text{heel bnd}} = \left\{ \theta_k : \{p_{\text{OL}}(\theta_h, z_h, \theta_k, \theta_a)\}_{\text{row } 3} = 0 \right\} \quad (7.30)$$

at a set of sample times spanning the remaining swing trajectory to obtain a planned knee trajectory (red trace in fig. 7.10B). Figures fig. 7.10C and E show the predicted inverse kinematics (IK) solutions at characteristic points into the swing for the knee and ankle respectively, with solutions leading to toe contact shown in purple and solutions leading to heel contact shown in yellow. For each

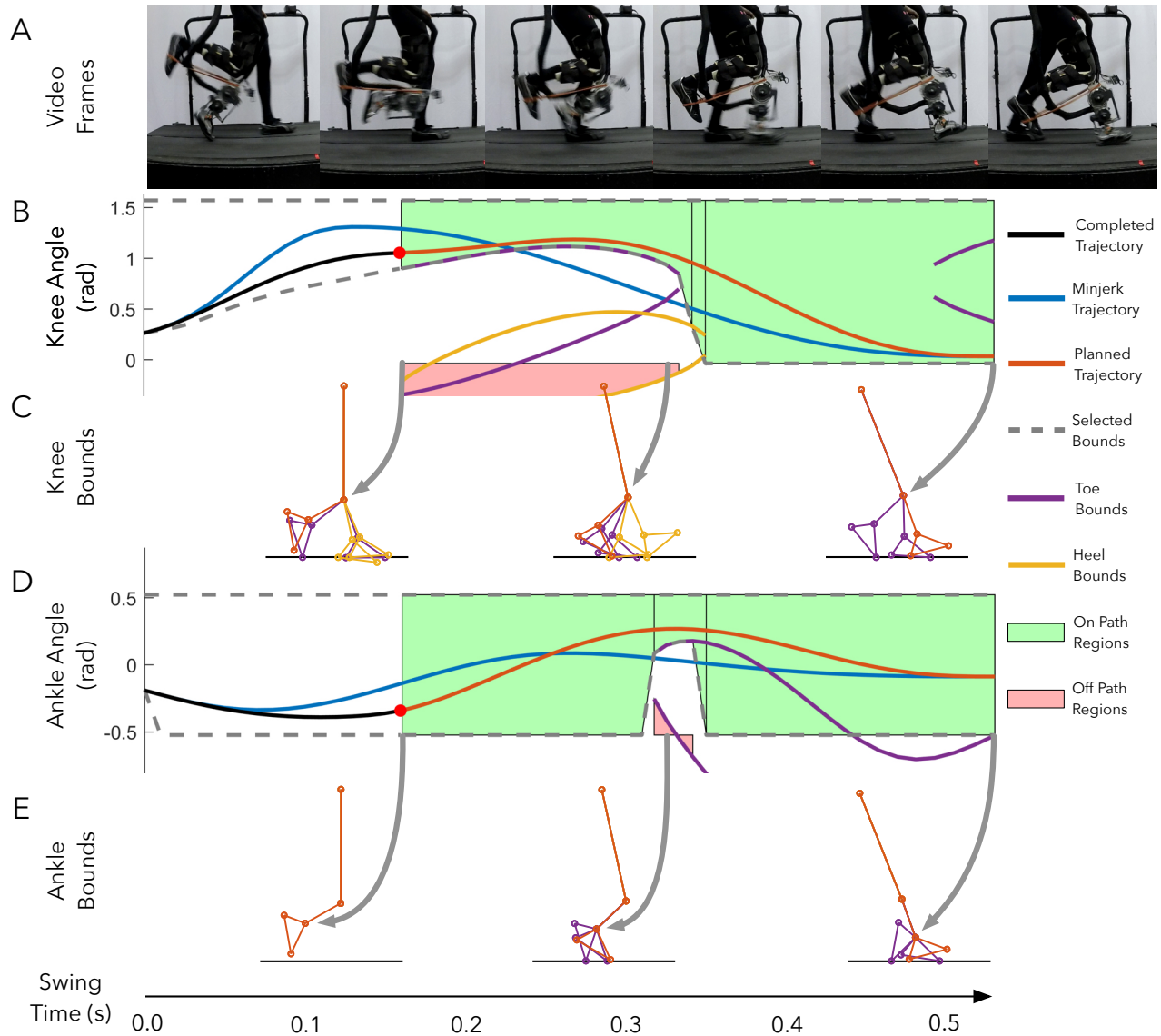


Figure 7.10: Planning Algorithm Steps: Panels B and D show the generated knee and ankle trajectories respectively. The planned trajectory (red) lies within the computed bounds (dashed gray). In contrast, standard minimum jerk trajectories (blue) do not respect the bounds, thereby increasing the tripping hazard. Panels C and E show examples of inverse kinematics (IK) solutions for toe (purple) and heel (yellow) contact for the knee and ankle joints respectively. We use the IK solutions to generate bounded regions that the planned trajectory can safely traverse. We consider ground contact constraints for only the first half of the remaining swing duration after which we only consider joint angle constraints. We use Dijkstra's algorithm to select regions (green) that allow a path from the start point to the desired final point. Bounded regions that do not lie on the path are shown in red. Panel A shows the corresponding prosthesis motion.

contact point, there are typically two solutions, one lower bound, for which the joint angle cannot cross from above, and one upper bound, for which the joint angle cannot cross from below.

Often, the valid leg configurations span disjointed regions in the configuration space (green and red regions in fig. 7.10B and D). Therefore, the planner next identifies a valid sequence of regions for the trajectory to traverse in a four step procedure. First, the planner identifies critical points along the predicted trajectory at which any bound activates or deactivates. Second, at each critical point, the planner sorts the bound angles from largest to smallest and iterates through them to define regions between successive upper and lower bounds. Third, the planner defines a graph over the regions with edge weights equal to the average squared angle minus the volume of the child region. This cost favors a sequence of regions that are large and thus safe to travel trough and avoids regions that require excessive joint flexion or extension. Dijkstra's algorithm is then used to find a valid sequence of regions that minimizes this cost [Dijkstra, 1959]. Finally, so that the generated trajectories do not get too close to the identified bounds, a buffer is added to the bounds. This buffer takes the form

$$\theta_{\text{buf}} = \theta_{\text{buf}}^0 \sin \left( \pi \frac{t - t_0}{t_f - t_0} \right), \quad (7.31)$$

where  $\theta_{\text{buf}}^0$  is either  $5^\circ$  or  $-5^\circ$  for lower and upper bounds respectively,  $t$  is the future swing time, and  $t_0$  and  $t_f$  are the current and final swing times.

After identifying the bounded regions, the planner generates the trajectory for a specific joint by solving a quadratic program. The trajectory of each joint is represented by three, fifth-order polynomial splines,

$$\theta_1(t) = a_{01} + a_{11}t + \dots + a_{51}t^5 = [1 \ t \ \dots \ t^5]a_1 \quad (7.32)$$

$$T_0 \leq t < T_1 \quad (7.33)$$

⋮

$$\theta_3(t) = a_{03} + a_{13}t + \dots + a_{53}t^5 = [1 \ t \ \dots \ t^5]a_3 \quad (7.34)$$

$$T_2 \leq t < T_F, \quad (7.35)$$

and solved for by the following QP,

$$a^* = \underset{a}{\operatorname{argmin}} \frac{1}{2} a^T (H_\theta + w H_{\ddot{\theta}}) a, \quad (7.36)$$

where  $a = [a_1^T \ a_2^T \ a_3^T]^T$ ,  $H_\theta$  and  $H_{\ddot{\theta}}$  encode quadratic costs on angle and jerk respectively, and  $w$  is a weight parameter. The solution is

subject to the inequality constraints

$$\theta(t) \leq \theta_{\max}(t), \forall t \quad (7.37)$$

$$\theta(t) \geq \theta_{\min}(t), \forall t \quad (7.38)$$

$$\dot{\theta}(t) \leq \dot{\theta}_{\max}, \forall t \quad (7.39)$$

$$\dot{\theta}(t) \geq \dot{\theta}_{\min}, \forall t, \quad (7.40)$$

which ensure the trajectory lies within the identified bounds and respects velocity limits, and to the equality constraints

$$\theta(T_0) = \theta_0 \quad (7.41)$$

$$\dot{\theta}(T_0) = \dot{\theta}_0 \quad (7.42)$$

$$\ddot{\theta}(T_0) = \ddot{\theta}_0 \quad (7.43)$$

$$\theta(T_F) = \theta_F \quad (7.44)$$

$$\dot{\theta}(T_F) = 0 \quad (7.45)$$

$$\ddot{\theta}(T_F) = 0 \quad (7.46)$$

$$\theta_1(T_1) = \theta_2(T_1) \quad (7.47)$$

$$\dot{\theta}_1(T_1) = \dot{\theta}_2(T_1) \quad (7.48)$$

$$\ddot{\theta}_1(T_1) = \ddot{\theta}_2(T_1) \quad (7.49)$$

⋮

which ensure the trajectory starts at the current and terminates at the desired positions, velocities, and accelerations and that the splines join together smoothly. If the QP fails to find a trajectory that can satisfy the constraints, the last found valid trajectory is reused for the next time step. In addition, at the first iteration, the ankle trajectory planner uses the output of the minimum jerk trajectory planner to solve the inverse kinematics for the bounds.

#### 7.6.4 Experimental Procedure

We tested the ability of the proposed trip avoidance control to reduce the incidence and severity of trips while walking with the powered transfemoral prosthesis shown in fig. 7.7 To evaluate the performance of the system, an able-bodied user walked with the prosthesis while attempting to elicit trips by lowering the hip in swing. During the stance phase, the prosthesis randomly decided to either use the proposed swing control or to use standard minimum jerk trajectories that do not consider the tripping hazard. The user was not aware of which controller would be used in the upcoming swing. The user completed a total of ten one minute walking trials.

We examined several outcomes for evaluating the control performance. First, we examined the distribution of knee angles at the

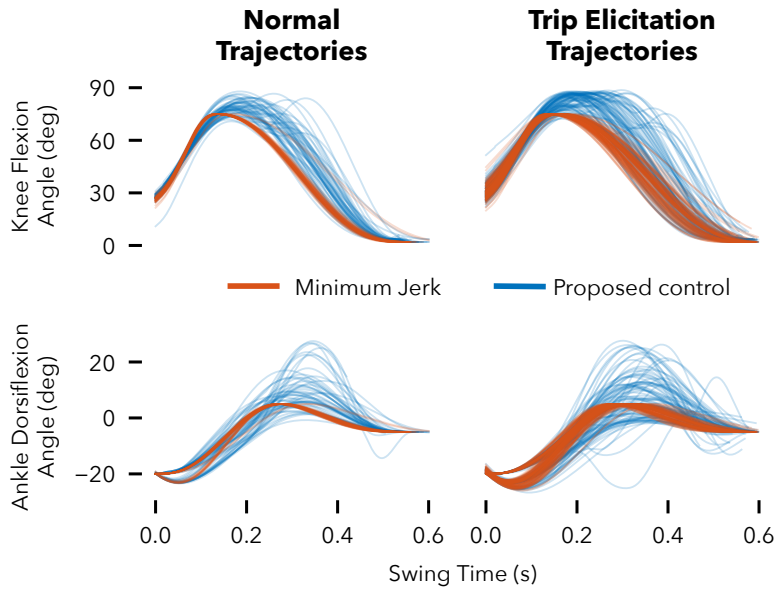


Figure 7.11: Knee and ankle trajectories produced during normal walking and while eliciting trips. To avoid tripping during trip elicitation trials, trajectories generated by the proposed approach often flex the knee to a greater degree and for longer before quickly extending at the end of swing. At the ankle joint we see overall greater variability in the generated trajectories during the trip elicitation condition versus normal walking.

beginning of stance. Large knee angles at the beginning of stance indicate premature landing due to toe-strike instead of heel strike. Ideally, the landing angle is close to the desired final angle of 2 degrees. Second, we checked the integral of the ground reaction force during swing. If this quantity is large, it indicates scuffing of the toe on the ground. Finally, we examined the relationship between the hip and toe heights during swing. If our controller is working as intended, the toe height during swing should have a decreased sensitivity to the hip height.

### 7.7 Planning Approach Results

Figure 7.11 shows the knee and ankle swing trajectories generated by the proposed control (blue) and by a standard jerk minimization control (red) during normal walking and trip elicitation. During undisturbed walking, the trajectories produced by both control strategies are similar. However, the proposed control strategy has a tendency to keep the knee flexed for longer and then extends it faster towards the end of swing. In addition, in a few steps, the proposed controller flexed the ankle significantly more than did the standard minimum jerk control. These trends are exaggerated during trip elicitation. There are more knee trajectories in which the knee stays flexed for longer, thereby creating more ground clearance. In addition, the ankle flexes earlier, which will help to create more foot

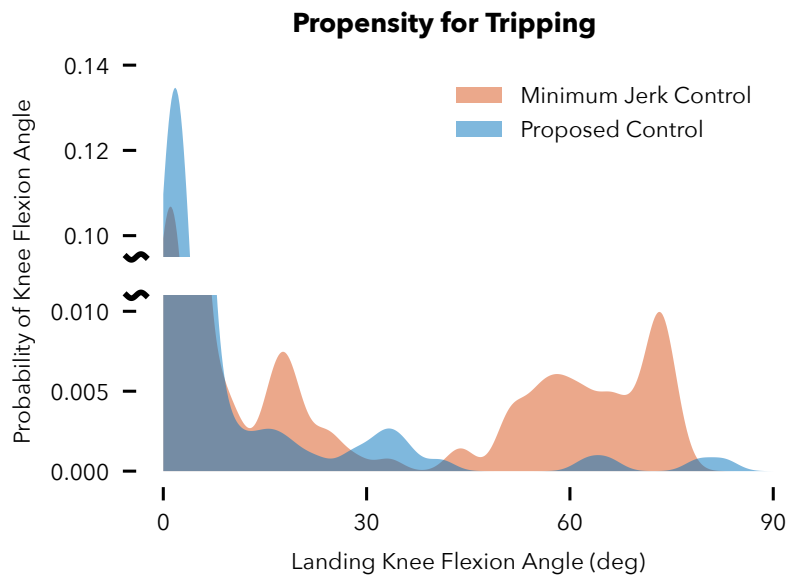


Figure 7.12: Kernel density estimate of the probability of various landing knee flexion angles with the proposed swing control (blue) and standard min-jerk swing control (red). Large landing knee angles indicate premature toe contact during swing.

clearance when the hip is suddenly lowered in early swing.

We used video and audio recordings of the trials, as well as data from the prosthesis, to manually classify trips as those swing trajectories that end with toe strike or during which the foot scuffed on the ground. We find that over the ten minutes of walking, the minimum jerk control produced 109 trips while the proposed approach produced 35 trips, reducing the trip rate by 68%.

To further examine the performance of the two control strategies, we used kernel density estimates of the landing knee flexion angle, a measure of the propensity for tripping, and integrated ground reaction force (GRF) during swing, a measure of the propensity for foot scuffing. Figure 7.12 shows the distributions of the landing angle of the prosthesis at the end of swing for the proposed swing control (blue) and for the standard minimum jerk swing control (red) during the trip elicitation condition. We observe the minimum jerk control is much more likely to generate a swing trajectory that ends prematurely with a large knee flexion angle, which is indicative of toe contact instead of heel contact at the end of swing. The distributions of the integrated GRFs suggests the minimum jerk control produced a larger percentage of swings with high ground reaction forces than the proposed control, indicating an increased frequency and severity of toe scuffing during swing (fig. 7.13).

We can also ask the question, “For steps during which the prosthesis used trajectories generated by the proposed control, would

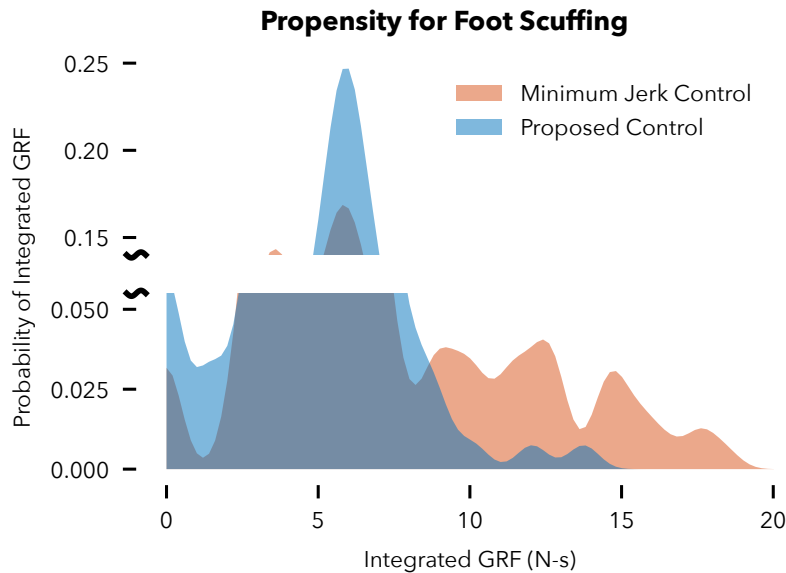


Figure 7.13: Kernel density estimate of the probability of various integrated ground reaction force values for the proposed swing control (blue) and standard min-jerk swing control (red). Large integrated GRF during the swing phase is indicative of the toe scuffing on the ground.

the user have tripped had the prosthesis used a minimum jerk trajectory?" To answer this question, we can use the kinematics model shown in fig. 7.7 along with ground truth hip height and hip angle data captured via a motion capture system, to estimate the location of the toe had the knee and ankle perfectly followed the desired trajectories produced by each control scheme. This analysis predicts that the prosthesis would have tripped or scuffed the toe on the ground during 22% of the steps if we had used the minimum jerk trajectory. In contrast, it predicts a trip or scuff rate of 5% had we perfectly followed the trajectories generated by the proposed control.

Finally, fig. 7.14 shows the relationship between the average toe and hip heights during swing for both control schemes. The toe height of the prosthesis when controlled by the proposed control is less sensitive to decreases in the hip height than it is when using the standard minimum jerk control.

## 7.8 Planning Approach Discussion

We presented initial work toward a real-time reactive control of powered prostheses to help amputees avoid tripping in the swing phase of gait. At any time during swing, the proposed control uses a laser range finder and an inertial measurement unit to estimate the current pose of the prosthesis, predicts the future hip angle and height based on trained Gaussian process models, and then plans

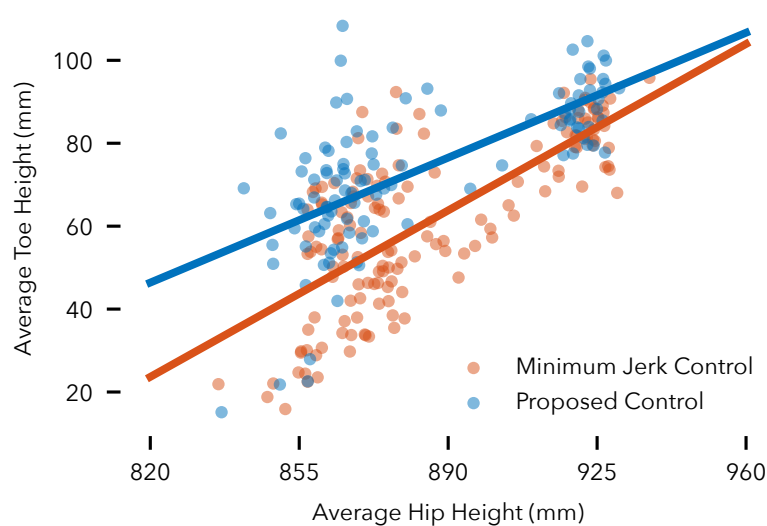


Figure 7.14: Average toe height vs average hip height for the proposed swing control (blue) and standard min-jerk swing control (red). The toe height during swing is less sensitive to the hip height when using the proposed swing control than when using the min-jerk swing control.

new knee and ankle joint trajectories that ensure neither the toe nor heel contacts the ground prematurely. Our results indicate the proposed control approach can substantially reduce the incidence of trips and reduce the severity and frequency of toe scuffing.

To the best of our knowledge, this work is the first demonstration of lower limb prosthetic control that integrates perception feedback in real-time and that proactively ameliorates the falling hazard amputees face. Previous research in this area has largely focused on detecting stumbles *after* they have occurred. For example, Lawson et al. [2010] and Shirota et al. [2014] have proposed classifiers that can detect trips during swing and predict whether a lower or raising strategy should be used in response. Similarly, Zhang et al. [2011a] have proposed a method that can detect stumbles and classify them as trips during swing or slips during stance. However, these previous studies have not proposed concrete control actions to preempt stumbles or to properly react in the event that a stumble is detected. Our results motivate further research into such proactive and reactive approaches, closing the perception-action loop for improving gait robustness with robotic prostheses.

Several avenues for future work exist. First, in our current study only one able-bodied user tested the proposed control. Further experiments with amputee subjects are needed to verify the system provides benefits to this population. For instance, amputees accustomed to walking with passive prostheses show significantly altered hip kinematics [Jaegers et al., 1995], which could affect the control

behavior. However, the proposed control should be able to properly adapt to these behavior differences, as the Gaussian process models are trained for specific users. Second, although trips during swing are one of the most common failure modes we encounter with our powered prostheses, these events are still rare and many hours of normal walking are required to observe a sufficient number of trips and compare controllers. As a result, we actively induced trips by sudden drops in hip height during swing, which does not exactly reflect the situations in which trips occur. Specifically, trips can happen due to subtle changes in leg kinematics, and it remains to be seen in experiments if our approach can avoid trips in these more subtle situations.

At the implementation level, there is also room for further exploration. To keep the computational costs low, we used quadratic programs that iterate between finding solutions for the ankle and knee joints. While this iterative approach is fast when compared to trajectory optimization methods that deal with multiple joints simultaneously, the iterations occasionally get stuck when the planner for one joint trajectory cannot find a solution based on the assumed fixed trajectory of the other joint. Moreover, if a solution cannot be found, the current approach simply reuses the last identified trajectory, rather than moving the trajectory to be more safe, even if it cannot fully satisfy the bounds. It seems worthwhile to investigate whether non-convex trajectory optimization methods such as CHOMP [Ratliff et al., 2009], in which the bounds are represented as soft rather than hard constraints, can help solve for the knee and ankle trajectories simultaneously without sacrificing computational speed.

In addition, several technical simplifications can be considered to bring this technology closer to commercialization. We used an accurate and expensive laser distance sensor, eyeing future research in obstacle scanning and avoidance capabilities. However, for simple ground plane avoidance, inexpensive infrared distance sensors such as those used by Scandaroli et al. [2009] are likely sufficient. It may also be possible to simplify the trajectory planning phase by, for example, forgoing formal guarantees on satisfying bounds and instead relying on heuristics to increase knee and ankle flexion and adjust timing in response to decreased hip height during swing.

Our immediate goal, however, is to generalize the presented approach to incorporating perception in control beyond the avoidance of flat ground. We are currently investigating the approach's ability to plan trajectories around obstacles that are scanned by the laser range finder. Previous studies such as Mohagheghi et al. [2004] with able-bodied subjects have shown that vision plays a crucial role in both planning and control of the lower limb motion over obstacles.

We also envision using the approach to target objects instead of avoiding them. For example, a prosthetic leg could scan, recognize, and target secure foot holds and stair treads, or provide enhanced sports capabilities by targeting and kicking a ball.

# *Robust and Adaptive Stance Control via Extended Kalman Filter-based Phase Estimation*

## *8.1 Introduction*

The number of lower limb amputees in the United States is projected to increase from 1.6 million in 2005 to 3.6 million in 2050 [Ziegler-Graham et al., 2008]. Expected causes include increases in the rates of vascular disease, diabetes, and the size of the elderly population. Prosthetic legs currently prescribed to these lower limb amputees are mostly passive or semi-passive devices; unlike human limbs, they cannot produce positive net work over a gait cycle. Consequently, amputees often suffer from slow walking speeds, high energy consumption [Waters et al., 1976], and an increased risk of falling [Miller et al., 2001]. Development of active powered prostheses may help address these gait deficiencies and improve the quality of life for amputees.

A variety of strategies have been proposed to control active-powered prostheses. Currently, the most widely used control method for powered transfemoral prostheses is finite state impedance control. This strategy divides the gait cycle into several discrete phases, each with a different function mapping from joint angle and speed to torque [Lawson et al., 2014]. This control method relies on the detection of gait events, such as joint angles crossing thresholds, to trigger phase transitions that may cause abrupt changes in torque output as well as unreliable responses to gait disturbances.

To achieve a more smooth and robust control of lower limb prostheses, researchers have investigated alternative approaches. One such alternative uses models of the human neuromuscular system. In this approach, the phase of gait is implicitly captured in the muscle states that emerge from the interplay between multi-segment limb dynamics, muscle dynamics, and reflexes [Eilenberg et al., 2010, Thatte and Geyer, 2016]. A downside to these approaches, however, is that

they often involve many parameters that may be difficult to tune, thus limiting clinical applicability. Another alternative approach is exemplified with the phase variable controller proposed by Quintero et al. [2016]. This controller explicitly derives a continuous phase estimate by comparing the hip angle to its integral. This approach may be sensitive to step-to-step changes in gait due to drift in the hip angle integral term. In later work, Rezazadeh et al. [2018] eliminated the reliance on the hip integral by re-introducing discrete state transitions based on thigh angle and velocity thresholds. However, this approach could face similar robustness issues as the previously described finite-state impedance control.

Here we propose a control strategy for lower limb prostheses that is built on a robust and smooth estimate of the phase of gait and does not require a large number of tuning parameters. In Section 8.2, we present an Extended Kalman Filter (EKF) that estimates the phase and its rate of change during the stance portion of gait based on a multitude of sensor measurements. We then use sparse Gaussian Process (GP) observation models to learn relationships between phase and sensor measurements for specific users and to choose the appropriate control actions for the prosthesis. In Section 8.3, we evaluate the performance of the proposed controller with experiments on able-bodied subjects and a single amputee subject. Finally, in section 8.4 we discuss the results and highlight potential limitations of this study as well as avenues for future research.

## 8.2 Methods

The proposed prosthesis controller consists of two components. The first is an Extended Kalman Filter (EKF) that estimates the gait phase, defined as the percent of stance completed so far (section 8.2.1). Ideally, the phase estimate starts at zero at heel strike and reaches one precisely at toe-off. The second component is a set of control surfaces, which are functions of phase and phase velocity, that provide desired knee and ankle angles, velocities, and feed forward torques for generating the prosthesis stance behavior (section 8.2.2).

### 8.2.1 GP-EKF for estimating phase

In contrast to the previously described phase variable approach for phase estimation in prostheses [Quintero et al., 2016], which uses a single source of information, we take a sensor-fusion approach and combine angle and velocity information from the hip, knee, and ankle joints of the prosthetic limb. An IMU mounted to the thigh portion of CMU’s powered knee-and-ankle prosthesis provides infor-

mation about the user's hip motion, and encoders on the prosthesis provide information about the knee and ankle joints. We use these observations in an Extended Kalman filter (EKF) to estimate the phase and phase velocity during stance. The EKF assumes the linear, discrete time phase dynamics

$$\begin{aligned} x_t = \begin{bmatrix} \phi_t \\ \dot{\phi}_t \end{bmatrix} &= \begin{bmatrix} 1 & \Delta t \\ 0 & 1 \end{bmatrix} \begin{bmatrix} \phi_{t-1} \\ \dot{\phi}_{t-1} \end{bmatrix} + w_t \\ &= Ax_{t-1}, \end{aligned} \quad (8.1)$$

where  $\phi$  is the phase,  $\dot{\phi}$  is the rate of change of phase,  $\Delta t$  is the integration time step and  $w_t \sim \mathcal{N}(0, Q)$ . We set

$$Q = \begin{bmatrix} 0 & 0 \\ 0 & \sigma_\phi^2 \end{bmatrix}, \quad (8.2)$$

with  $\sigma_\phi^2 = 1e-7$ . These dynamics encode the assumption that phase should evolve continuously, at a roughly constant rate.

Observations of the prosthesis-side hip, knee, and ankle angles and velocities inform the evolution of the above dynamics. For the joint angles, the observation models are of the form

$$z_t^{\theta_j} = h^{\theta_j}(x_t) + v_t^{\theta_j} = \text{GP}_\mu^{\theta_j}(\phi_t) + v_t^{\theta_j}, \quad (8.3)$$

where  $\text{GP}_\mu^{\theta_j}$  is the mean of a learned Gaussian Process (GP) model of the angle of joint  $j$  as a function of the phase  $\phi$  and  $v_t^{\theta_j} \sim \mathcal{N}(0, \text{GP}_{\sigma^2}^{\theta_j}(\phi_t))$ .

Here,  $\text{GP}_{\sigma^2}^{\theta_j}$  is the variance of the same learned GP model.

Similarly, for the joint velocities we use an observation model of the form

$$\begin{aligned} z_t^{d\theta_j/d\phi} &= h^{d\theta_j/d\phi}(x_t) + v_t^{d\theta_j/d\phi} \dot{\phi}_t \\ &= \left( \text{GP}_\mu^{d\theta_j/d\phi}(\phi_t) + v_t^{d\theta_j/d\phi} \right) \dot{\phi}_t \end{aligned} \quad (8.4)$$

where  $\text{GP}_\mu^{d\theta_j/d\phi}$  is the mean of a Gaussian Process model of the velocity of joint  $j$  (in units of  $d\theta_j/d\phi$ ) as a function of  $\phi$ . In addition,  $v_t^{d\theta_j/d\phi} \sim \mathcal{N}(0, \text{GP}_{\sigma^2}^{d\theta_j/d\phi}(\phi_t))$ , where  $\text{GP}_{\sigma^2}^{d\theta_j/d\phi}$  is the variance of the same learned GP model for joint velocity.

To train the GP observation models, the algorithm maintains a training data set of stance gait data. The training data set includes the joint angles and velocities (in units of  $d\theta_j/d\phi$ ) sampled at 100 Hz as well as the actual corresponding phases and phase velocities during stance. We assume that, in hindsight, the actual phase increased linearly from zero at heel strike to one at toe off and that the actual phase velocity was constant during stance and equal to  $1/T_n$ , where

$T_n$  is the duration of the completed stance phase. We retrain the GP models using this gait data after every five completed steps. To ensure that the test-time performance of the Gaussian Process models does not degrade as more training data accumulates, we employ the fully independent training conditional (FITC) approximation of the GP [Snelson and Ghahramani, 2007]. This approximation represents the GP using a fixed-size active set of training points. (We use 25 points in our approximation).

With the learned GP observation models, we follow the GP-EKF procedure proposed by Ko and Fox [2009] to obtain an estimate of phase and phase velocity. In this procedure, we first *predict* the next state distribution by propagating the mean  $\hat{x}_{t-1|t-1}$  and covariance  $\Sigma_{t-1|t-1}$  of the state using the dynamics model provided by eq. (8.1),

$$\hat{x}_{t|t-1} = A\hat{x}_{t-1|t-1} \quad (8.5)$$

$$\Sigma_{t|t-1} = A\Sigma_{t-1|t-1}A^T + Q. \quad (8.6)$$

Next, we *update* the state distribution estimate given measurements  $z_t$  of the joint angles and velocities using the following equations and the GP observation models  $h_t(x_t)$ .

$$K_t = \Sigma_{t|t-1}H_t^T \left( H_t \Sigma_{t|t-1} H_t^T + M_t R M_t^T \right)^{-1} \quad (8.7)$$

$$\hat{x}_{t|t} = \hat{x}_{t|t-1} + K_t (z_t - h(\hat{x}_{t|t-1})) \quad (8.8)$$

$$\Sigma_{t|t} = (I - K_t H_t) \Sigma_{t|t-1} \quad (8.9)$$

where,

$$h(x_t) = \begin{bmatrix} \text{GP}_\mu^{\theta_h}(\phi_t) \\ \text{GP}_\mu^{\theta_k}(\phi_t) \\ \text{GP}_\mu^{\theta_a}(\phi_t) \\ \text{GP}_\mu^{d\theta_h/d\phi}(\phi_t)\dot{\phi}_t \\ \text{GP}_\mu^{d\theta_k/d\phi}(\phi_t)\dot{\phi}_t \\ \text{GP}_\mu^{d\theta_a/d\phi}(\phi_t)\dot{\phi}_t \end{bmatrix} \quad (8.10)$$

$$H_t = \frac{\partial h}{\partial x} \Big|_{\hat{x}_{t|t-1}} = \begin{bmatrix} \frac{\partial \text{GP}_\mu^{\theta_h}}{\partial \phi_t} \Big|_{\phi_t} & 0 \\ \frac{\partial \text{GP}_\mu^{\theta_k}}{\partial \phi_t} \Big|_{\phi_t} & 0 \\ \frac{\partial \text{GP}_\mu^{\theta_a}}{\partial \phi_t} \Big|_{\phi_t} & 0 \\ \frac{\partial \text{GP}_\mu^{d\theta_h/d\phi}}{\partial \phi_t} \Big|_{\phi_t} \dot{\phi}_t & \text{GP}_\mu^{d\theta_h/d\phi} \\ \frac{\partial \text{GP}_\mu^{d\theta_k/d\phi}}{\partial \phi_t} \Big|_{\phi_t} \dot{\phi}_t & \text{GP}_\mu^{d\theta_k/d\phi} \\ \frac{\partial \text{GP}_\mu^{d\theta_a/d\phi}}{\partial \phi_t} \Big|_{\phi_t} \dot{\phi}_t & \text{GP}_\mu^{d\theta_a/d\phi} \end{bmatrix} \quad (8.11)$$

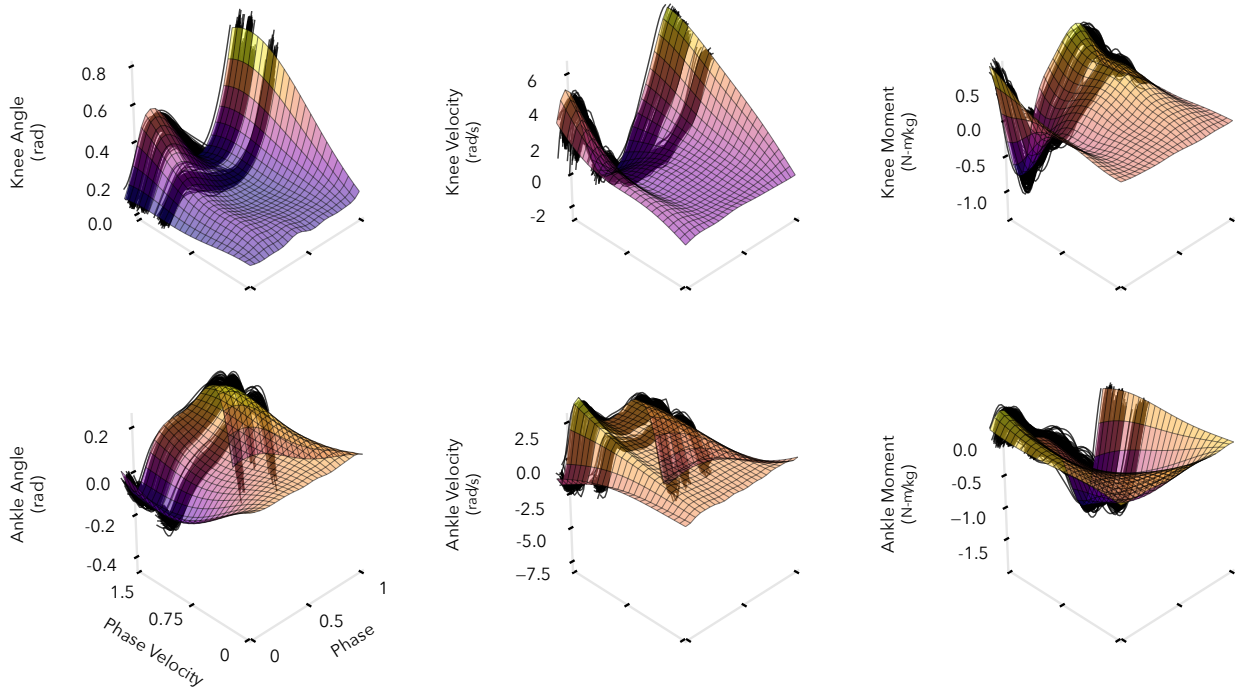


Figure 8.1: Examples of learned control surfaces. We fit the surfaces to gait data from Moore et al. [2015]. This data includes information for three speeds, 0.8, 1.2, and 1.6 m/s, which are shown as the clustered trajectories in the above panels. For an automatic transition to standing, the surfaces are additionally fit to virtual data that causes the joint angles to approach 5 deg, the velocities to approach 0 deg/s, and the joint torques to approach 0 N-m as the phase velocity goes to zero.

$$M_t = \frac{\partial h}{\partial v_t} \Big|_{\hat{x}_{t|t-1}} = \begin{bmatrix} I_{3 \times 3} & 0 \\ 0 & \dot{\phi}_t I_{3 \times 3} \end{bmatrix} \quad (8.12)$$

$$R_t = \text{blkdiag} \left( \text{GP}_{\sigma^2}^{\theta_h}(\phi_t), \text{GP}_{\sigma^2}^{\theta_k}(\phi_t), \text{GP}_{\sigma^2}^{\theta_a}(\phi_t), \text{GP}_{\sigma^2}^{d\theta_h/d\phi}(\phi_t), \text{GP}_{\sigma^2}^{d\theta_k/d\phi}(\phi_t), \text{GP}_{\sigma^2}^{d\theta_a/d\phi}(\phi_t) \right) \quad (8.13)$$

Due to the linearity of Gaussian processes and differentiation, we can analytically obtain derivatives required by eq. (8.11) using the methods provided by Solak et al. [2003].

Finally, we reset the state distribution at heel strike to

$$\hat{x}_0 = \begin{bmatrix} 0 \\ 1/T_{n-1} \end{bmatrix}, \quad \Sigma_0 = 0_{2 \times 2}, \quad (8.14)$$

where  $T_{n-1}$  is the duration of the previous stance.

### 8.2.2 Control Surfaces

We use the mean estimates of the phase  $\phi$  and phase velocity  $\dot{\phi}$  as the inputs into learned control surfaces that provide the desired knee and ankle angles, velocities, and feed-forward torques (Fig. 8.1). The final desired torques applied to the prosthesis are then given by

$$\tau_d = k_p (\theta_d(\phi, \dot{\phi}) - \theta) + k_d (\dot{\theta}_d(\phi, \dot{\phi}) - \dot{\theta}) + \tau_{ff}(\phi, \dot{\phi}), \quad (8.15)$$

where  $\theta_d$ ,  $\dot{\theta}_d$ , and  $\tau_{ff}$  are the learned control surfaces as functions of the estimated phase and phase velocity,  $k_p$  and  $k_d$  are proportional and derivative gains, and  $\theta$  and  $\dot{\theta}$  are the actual joint angle and velocity.

We learned the control surfaces  $\theta_d$ ,  $\dot{\theta}_d$  and  $\tau_{ff}$ , by regressing the gait data provided by Moore et al. [2015] for several subjects walking at three speeds, 0.8, 1.2, and 1.6 m/s. We were able to learn the control surfaces using the data from nine subjects. For each subject, we split the gait data into individual stance phases and extracted the knee and ankle angles, velocities, and joint torques. We also assumed that during each stance, the actual phase increased linearly from zero at heel strike to one at toe off and the phase velocity during stance was constant and equal to  $1/T$ , where  $T$  is the duration of stance. We again used sparse GP regression with the FITC approximation to regress the knee and ankle angles, velocities, and torques versus the phase and phase velocity. In this case, we used 100 active vectors to approximate each GP.

The gait data spans the whole range of phases ([0, 1]) but not the whole range of physiological phase velocities, as the gait speed only varies between 0.8 and 1.6 m/s. To ensure the control surfaces generate smooth behaviors at slower speeds and when standing still ( $\dot{\phi} = 0$ ), we additionally trained the GPs on a grid spanning  $\phi \in [0, 1]$  and  $\dot{\phi} \in [0, \min(\dot{\phi}_{\text{data set}})]$  with *virtual* training values derived from interpolating between the average trajectory at 0.8 m/s and desired values at  $\dot{\phi} = 0$ . When  $\dot{\phi} = 0$ , the desired joint angles, velocities and torques were set to 5 deg, 0 deg/s, and 0 N-m, respectively, thereby creating a smooth transition to a standing mode. Figure 8.1 shows examples of the resulting control surfaces derived from one subject's data.

### 8.2.3 Experimental Protocol

We evaluated the naturalness of gait and the robustness of our proposed controller in experiments conducted with seven able-bodied subjects, and an amputee subject. We additionally present data from an experienced user of the prosthesis (first author of paper), whose gait characteristics induced a different response from the prosthesis. All subjects provided informed consent to IRB-approved protocols. The amputee subject wore the powered prosthesis prototype shown in fig. 8.2, while able-bodied subjects used a shortened version of the prosthesis attached via an L-shaped adapter. (for more information on prosthesis specifications see [Thatte et al., 2018]). All subjects had at least six hours of prior practice walking on the prosthesis. The able-bodied subjects walked without assistance from handrails, while

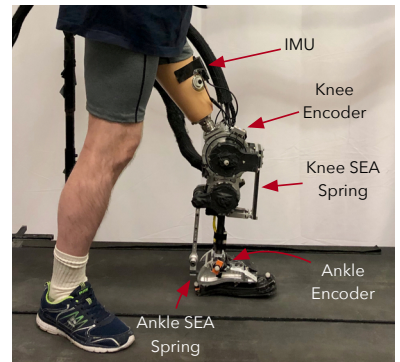


Figure 8.2: CMU powered prosthesis used in experiments. The prosthesis has brushless motors at the knee and ankle joints, series elastic actuators for torque control, and an IMU mounted to the thigh portion to measure residual limb angle.

the amputee subject used the handrails for balance.

We compared our proposed control method to a stance control based on a neuromuscular model of human neurophysiology [Thatte et al., 2018] and to finite state impedance control [Lawson et al., 2014]. For these controllers, we generated parameter sets by fitting control parameters to the same nine subjects' gait data used to generate the control surfaces described in section 8.2.2. For neuromuscular control, we used the black-box CMA-ES optimizer [Hansen, 2006] to fit the control parameters as described in [Thatte et al., 2018]. For impedance control, we used robust RANSAC linear regression [Fischler and Bolles, 1981] to fit the stiffness, damping, and angle offset parameters within the three discrete phases of stance. The transition between phases 1 and 2 was based on the knee angle crossing a threshold, while the transition between phases 2 and 3 was based on the ankle angle crossing a threshold. We set these thresholds so that 95% of steps in the gait data transition through all three phases. Prior to beginning the experiments, subjects walked with each of the nine control surfaces (parameter sets) for each controller and indicated their preferred settings. All three stance control strategies were paired with the same swing control strategy, in which minimum jerk trajectories for the knee and ankle are generated at toe-off and tracked with PD-feedback combined with a model-based feed forward term as in [Lenzi et al., 2014]. In total, we conducted four experiments:

(1) A test of the ability of each control strategy to reproduce a normal walking gait pattern. Able-bodied subjects walked without the use of handrails  $0.8 \text{ m/s}$  and the amputee subject used the handrails and walked at  $0.6 \text{ m/s}$ . All subjects walked with their preferred parameters for each controller for one minute. We compared the resulting prosthesis knee and ankle kinematics and kinetics to able-bodied gait data [Bovi et al., 2011] to determine the naturalness of gait.

(2) A comparison of the robustness of the three controllers to ground height disturbances. We simulated a ground disturbance by having subjects step on  $3 \text{ cm}$  blocks placed on the treadmill. We tested the controllers in a random order in an ABCCBA sequence. In each trial, the subjects stepped on blocks 20 times. We recorded the number of falls, defined as instances when subject needed support from either the handrails or a ceiling mounted harness to regain balance.

(3) A test of the adaptability of the phase estimate. To test the adaptability, we had subjects use the proposed GP-EKF control while the treadmill speed varied sinusoidally between  $0.4$  and  $1.2 \text{ m/s}$  with a  $20 \text{ s}$  period. We compared the phase and phase velocity estimates

given by the EKF filter to the true phase, assumed to increase linearly from zero at heel strike to one at toe off, and the true phase velocity, assumed to equal  $1/T_n$ , where  $T_n$  is the duration of the current stance. As a baseline, we compared the EKF to time-based phase and phase velocity estimates, which assume the duration of the current stance will be the same as the previous stance, resulting in the phase and phase velocity estimates

$$\phi_{\text{time based}} = t_n / T_{n-1} \quad (8.16)$$

$$\dot{\phi}_{\text{time based}} = 1 / T_{n-1}, \quad (8.17)$$

where  $t_n$  is the time after heel-strike of the current stance and  $T_{n-1}$  is the duration of the last stance.

(4) Finally, a test of the ability of the GP-EKF control to respond to sudden treadmill stops. If the subject stops his or her gait, then the phase estimate should stabilize and the phase velocity should trend towards zero. The corresponding desired joint angles should approach 5 deg as shown in fig. 8.1.

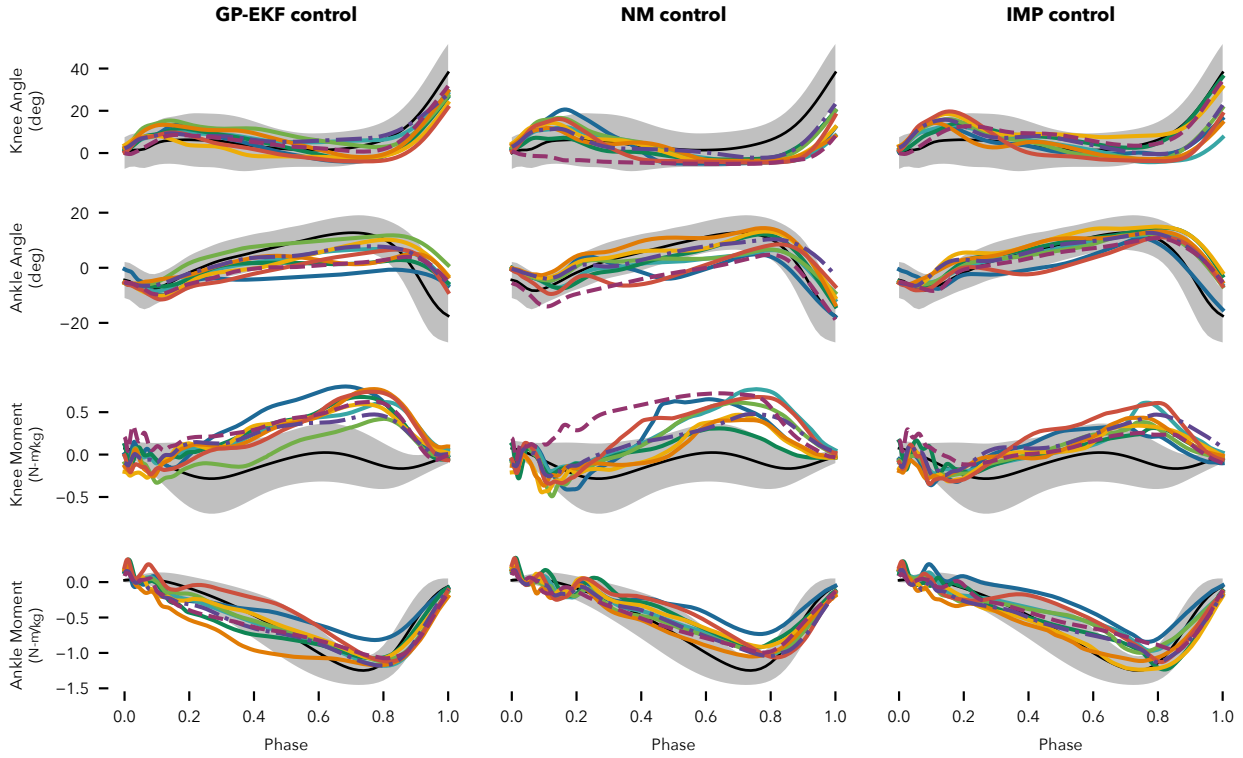
We assess significant differences between conditions via the two-sided paired Wilcoxon signed rank test [Gibbons and Chakraborti, 2011]. Experienced subject data was not considered for significance testing.

### 8.3 Results

#### 8.3.1 Ability to Reproduce Normal Walking

Figure 8.3 shows the average knee and ankle angles as well as the corresponding joint moments generated by the prosthesis controllers during undisturbed walking at 0.8 m/s. All three control strategies produce knee angle trajectories that are similar to the able-bodied data (first row). The neuromuscular (NM) control, however, seems to suffer more from knee over extension during mid-stance and less knee flexion at the end of stance. For some able-bodied subjects, and to a substantial degree for the amputee subject, the knee over-extension causes the joint to engage the mechanical hard-stop on the prosthesis. This triggers a sudden rise in knee torque. Figure 8.4a summarizes the root-mean-squared (RMS) error between the mean able-bodied knee kinematics and the median knee kinematics of each subject. The GP-EKF control strategy produces significantly more kinematically natural knee angle trajectories, whereas the NM control produces the least kinematically natural knee trajectories.

The second row of fig. 8.3 shows the average ankle trajectories for each control strategy. In this case, the GP-EKF control produced the least accurate trajectories. As shown in fig. 8.4b, this trend reached



statistical significance compared to impedance (IMP) control, which produced the most natural ankle angle trajectories. The unnaturalness of the GP-EKF control ankle trajectories is largely due to (1) a lack of plantar flexion in the push-off phase and (2) a lack of dorsiflexion during mid-stance for 3 out of 8 subjects, who all chose the same controller set.

Finally, the third and fourth row of fig. 8.3 show the knee and ankle moments for the three controllers. IMP control produced the most natural knee moments by a significant margin (fig. 8.4c), whereas the GP-EKF and NM controllers performed comparably. Although the GP-EKF control produced the least natural ankle moments, the absolute differences were small (fig. 8.4d).

Figure 8.3: Ability to reproduce normal walking. Average knee angle (row 1), ankle angle (row 2), knee moment (row 3), and ankle moment (row 4) for the GP-EKF controller (column 1), neuromuscular controller (column 2), and impedance controller (column 3). Black traces and gray shaded areas show the mean and two standard deviations for very slow human walking data (from [Bovi et al., 2011]). Colored lines show individual subject data. Amputee gait data indicated by dashed lines and experienced user data indicated by dash-dot lines.

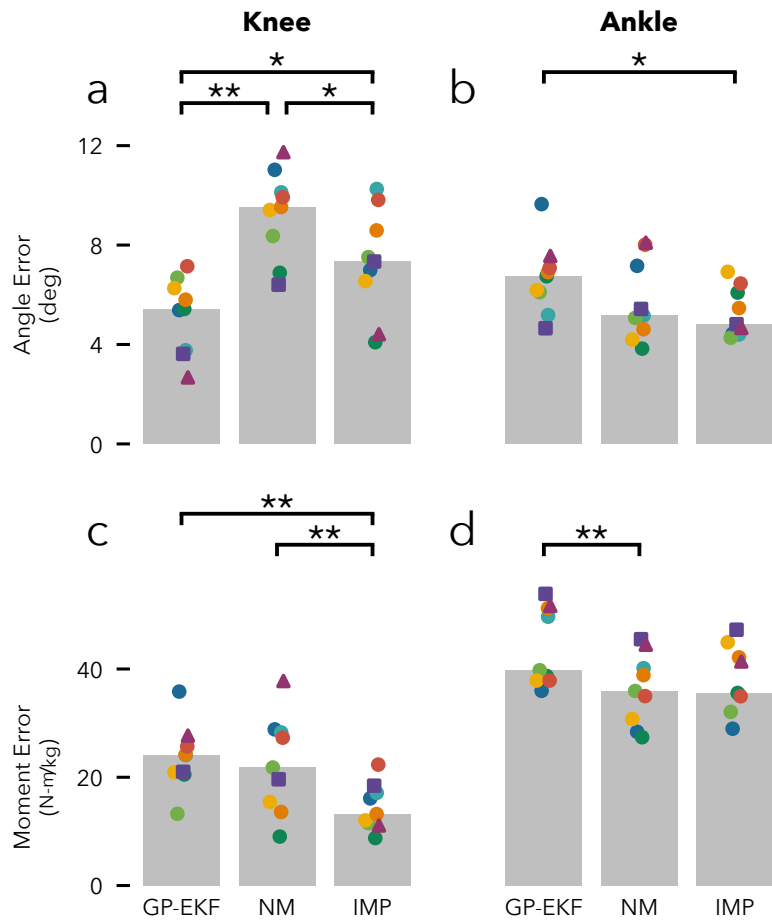


Figure 8.4: Average kinematic (a,b) and kinetic (c,d) errors produced by the three different controllers compared to able-bodied data. GP-EKF produces significantly more natural knee angles than NM or IMP control, but slightly less natural ankle angles and joint torques. Grey bars show median of subject data, circle markers indicate able-bodied subject data, triangle markers indicate amputee data, and square markers indicate experienced able-bodied user data.  
\* :  $p < 0.05$ , \*\* :  $p < 0.01$ .

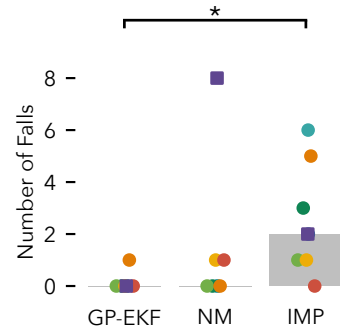


Figure 8.5: Robustness to ground height disturbances. Number of falls accrued for each controller during ground height disturbance trials. GP-EKF control significantly reduced the number of falls compared to IMP control.

### 8.3.2 Robustness to Ground Height Disturbances

Figure 8.5 shows the number of times able-bodied subjects fell with each control strategy when stepping on blocks. Subjects fell significantly more often with the IMP control compared to either the GP-EKF or NM controllers. However, when using the neuromuscular control the experienced user fell 8 times, more than any other subject in any condition.

### 8.3.3 Adaptability of Phase Estimate

The adaptability of the phase estimate was tested by sinusoidally varying the treadmill speed during walking. Figure 8.6 shows the average RMS errors of the EKF-based phase estimate and time-based phase estimate compared to the ground-truth phase obtained in hindsight. For all subjects, the EKF tracked the true phase significantly

more accurately than did the time-based phase estimate.

For a more specific example, fig. 8.7 shows the phase estimates during the treadmill speed variation experiment for a single subject. Because the initial conditions of the EKF and the time-based phase estimates are identical (compare eq. (8.14) and eq. (8.17)), the phase estimates are similar in early stance. As the treadmill speed changes from one step to the next, the time-based phase estimate diverges significantly from the true phase. The EKF, on the other hand, is able to recover to the true phase towards the end of stance and more accurately predicts the toeoff event.

### 8.3.4 Response to Sudden Treadmill Stops

Finally, fig. 8.8 shows the phase (a), and phase velocity (b) estimates when the treadmill is suddenly stopped halfway through the stance phase. The EKF phase estimates (solid lines) reflect the fact that the gait cycle has halted, as they do not continue to progress to one. Moreover, when the treadmill stops, the knee (c) and ankle angles (d) approach 5 deg as desired for standing (compare fig. 8.1). In contrast, the time-based phase estimates (dashed lines in panels (a) and (b)) continue at their initial rate, with the phase reaching one.

## 8.4 Discussion

We proposed a new approach for the control of powered transfemoral prostheses. The approach uses a robust estimate of the gait phase derived from an EKF that integrates multiple sensor measurements to determine the desired knee and ankle angles, velocities and torques from trained control surfaces. The proposed approach improved knee kinematics over NM and IMP control, matched NM control and improves upon IMP control in terms of gait robustness to ground height disturbances, and adapted the phase estimate to both gradual and abrupt changes in speed more quickly than a time-based phase estimate.

We believe the robustness improvements of the proposed GP-EKF control scheme and the NM control over IMP control stem from the smoothness of the phase estimation in these two controllers. In NM control, the phase estimation is implicit and encoded in the internal states of virtual muscles, which are modulated by musculoskeletal dynamics and reflexes. In the proposed control presented here, the EKF directly infers a robust estimate of phase from multiple measurements. In either case, the resulting control commands are smooth and do not normally change abruptly from one moment to the next. In contrast, IMP control splits the stance phase into three discrete

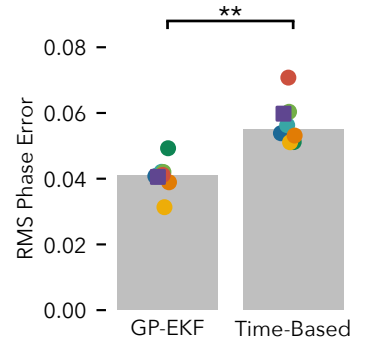


Figure 8.6: Adaptability of phase estimate. Mean phase error of EKF versus time-based phase estimation when walking with sinusoidally varying treadmill speed. The EKF significantly improves phase tracking compared to the time-based estimate.

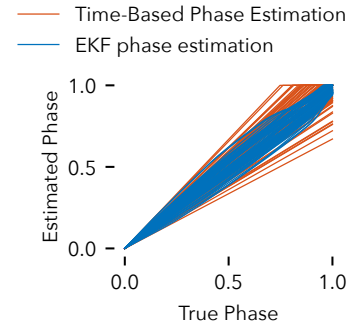


Figure 8.7: Example of EKF-based phase estimation (red) versus time-based phase estimation (blue) for one subject. Due to step-to-step speed variations caused by the sinusoidally varying treadmill speed, the time based phase estimation accrues significant errors. In contrast, the EKF-based phase estimate is able to respond to changes in gait within the gait cycle, thus reducing phase estimation errors.

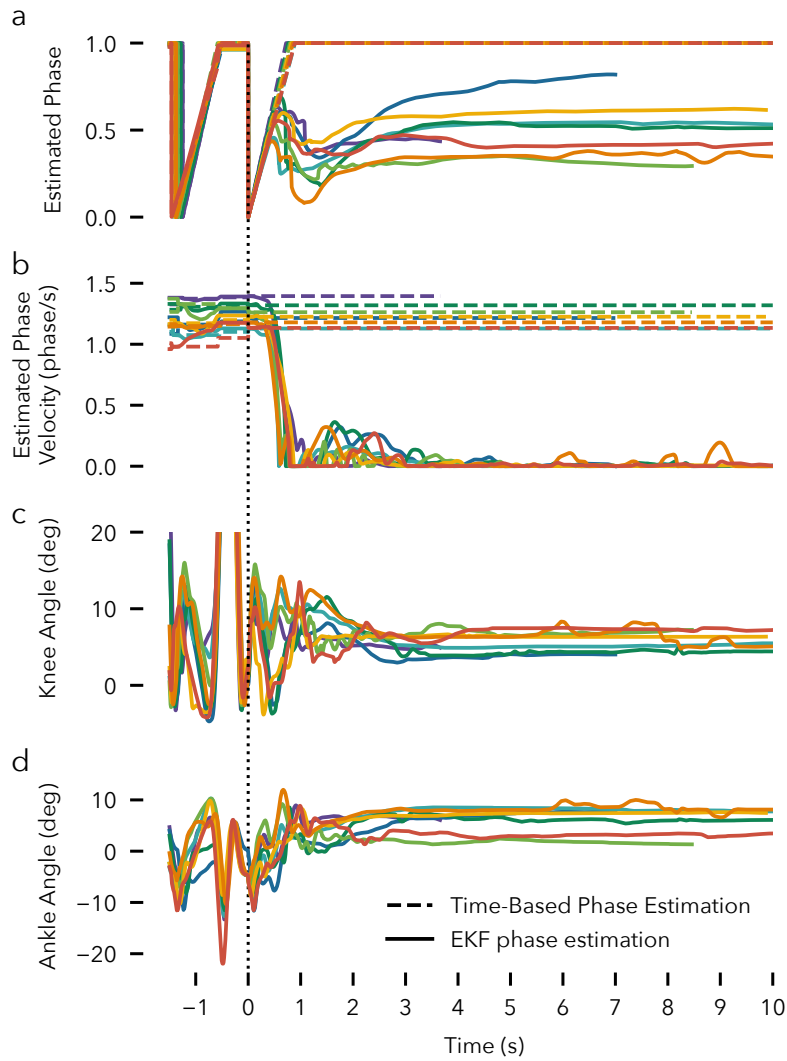


Figure 8.8: Response to sudden treadmill stops. Estimated phase (a) and phase velocity (b), and the measured knee (c) and ankle (d) angles when the treadmill is suddenly stopped half way through stance. When gait stops, the EKF-estimated phase stabilizes to a constant value (solid traces), phase velocity falls to zero, and the joint angles approach 5 deg as desired by the control surfaces (compare fig. 8.1). The time-based phase estimate fails to respond (dashed lines). Vertical black dotted line indicates heel strike of final stance phase.

phases that are triggered by joint angle thresholds. Consequently, in the ground height disturbance experiments, subjects were occasionally caught off-guard by unexpected transitions, triggered by abnormal kinematics when stepping on a block, which then caused large, sudden changes in torque. Unexpected phase transitions between the mid-stance and late-stance phases were especially consequential, as in the late-stance phase, knee torque trends towards zero to allow for passive knee flexion, while the ankle plantarflexes. If a user's center of mass is positioned incorrectly, this combination of joint torques can cause a sudden collapse of the knee, which was the cause for many of the observed falls with IMP control.

NM control too can result in unexpected falls due to incorrect phase estimation. The experienced user fell a total of eight times when stepping on blocks with the NM control (see square marker fig. 8.5). These falls were the result of a modelled reflex that reduces knee extensor muscle stimulation in late stance in proportion to ankle plantarflexion, thereby allowing for passive knee flexion leading into swing. In contrast to less experienced subjects, the experienced user was able to control the knee over-extension during stance and achieve more normal knee flexion in late-stance during normal walking (see fig. 8.3 row 1, column 2). However, this increased knee flexion during normal walking may have increased the prosthesis' susceptibility to premature knee collapse when disturbed. While the modeled neuromuscular reflexes seem to work well during steady-state walking and during disturbed walking for inexperienced users, the large increase in falls for the experienced user, exposes the difficulty of relying on heuristic reflexes to obtain robust control across a range of gait characteristics. In contrast, the proposed EKF approach takes a principled approach to phase estimation and thus resulted in the fewest falls.

Some improvements can be made in the implementation of the proposed control. First, the normal walking experiments reveal that the ankle trajectories produced by the GP-EKF control are less natural than those produced by NM or IMP control (see fig. 8.4b). The GP-EKF ankle trajectories in fig. 8.3 show that peak ankle flexion is achieved later in stance and that the ankle insufficiently plantarflexes at toeoff. These kinematic issues are also present in the desired angles commanded by the GP control surfaces. Therefore, this issue likely stems from a premature cutoff between stance and swing in the gait dataset used to generate the control surfaces. Extending the training data stance duration slightly should increase the desired ankle plantarflexion at the end of stance and engage the peak ankle dorsiflexion earlier.

Second, in the current study, we held constant the impedance about the desired trajectory, represented by  $k_p$  and  $k_d$  in eq. (8.15). However, recent research has investigated how impedance varies continuously throughout gait [Lee et al., 2016]. These results could be used to parameterize impedance as a function of phase. Taking this step could help improve the naturalness of the knee and ankle torques produced by the GP-EKF controller, which currently trail those produced by the NM and IMP controllers (see figs. 8.4c and d).

Our work bears some resemblance to the complementary limb motion estimation (CLME) approach proposed by Vallery et al. [2011]. This approach uses linear regression to learn a direct mapping between the angles and velocities of the user's limbs to the prosthesis'

joint angles and velocities. There are two key differences between our and the CLME approach. First, our approach only uses signals from sensors mounted to the prosthesis itself, whereas the CLME approach used many IMUs mounted to the torso and sound side leg. Donning these sensors may be impractical for everyday use by an amputee in the real world. Second, the CLME approach directly maps from human to prosthetic joint angles and velocities via linear regression. In contrast, our approach goes through the latent phase and phase velocity states first, which decouples the observation models from the prosthesis control models. This allows us to separately learn the observation models and tune the control models to optimize user preference and performance.

There are several avenues for future research to expand the proposed control approach. First, we only used prosthesis joint angles and velocities for the observation models. It is worth investigating if additional measurements such as ground reaction forces, accelerations, and EMG signals improve the state estimate. Second, we used a simple, two-state model to represent the entirety of the coupled human-prosthesis state during stance. Adding additional state variables may help capture important behaviors such as balance recovery actions taken by the upper body. To this end, dimensionality reduction techniques could help identify better state representations from gait data. New state representations need to satisfy two constraints that our current model satisfies: (1) The evolution of the state needs to approximately abide by some Markov dynamics model so we can perform the predict step of the EKF (eqs. (8.5) and (8.6)). (2) The evolution of state throughout stance should be knowable in hindsight after a step is completed so that the observation model can be learned online. Finally, with more advanced state and observation models, more advanced forms of state estimation may be necessary, including unscented Kalman filters or particle filters such as the one proposed by Dhir et al. [2018], which allows for continuous gait phase estimation using discrete heel and toe contact sensors.

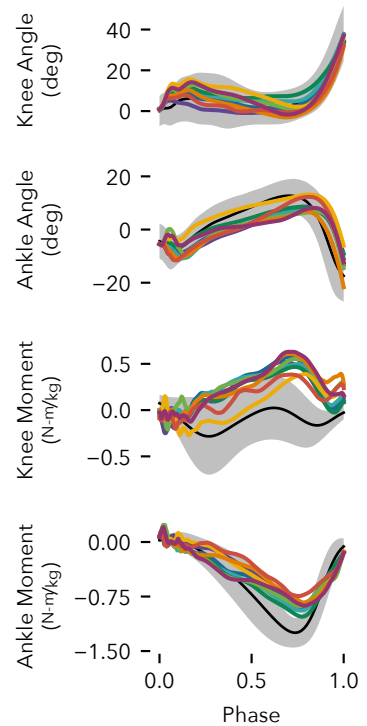


Figure 8.9: GP-EKF phase-based control with fixed control surfaces and increased ankle impedance.

9

## *Future Work*

Get reflex control model to reproduce disturbed walking data results.



## Bibliography

Navid Aghasadeghi, Huihua Zhao, Levi J Hargrove, Aaron D Ames, Eric J Perreault, and Timothy Bretl. Learning impedance controller parameters for lower-limb prostheses. In *Intelligent robots and systems (IROS), 2013 IEEE/RSJ international conference on*, pages 4268–4274. IEEE, 2013.

Brian DO Anderson and John B Moore. Optimal filtering. *Englewood Cliffs*, 21:22–95, 1979.

Samuel K Au and Hugh M Herr. Powered ankle-foot prosthesis. *IEEE Robotics & Automation Magazine*, 15(3):52–59, 2008.

Samuel K Au, Jeff Weber, and Hugh Herr. Biomechanical design of a powered ankle-foot prosthesis. In *2007 IEEE 10th International conference on rehabilitation robotics*, pages 298–303. IEEE, 2007.

Gabriele Bovi, Marco Rabuffetti, Paolo Mazzoleni, and Maurizio Ferrarin. A multiple-task gait analysis approach: kinematic, kinetic and emg reference data for healthy young and adult subjects. *Gait & posture*, 33(1):6–13, 2011.

Eric Brochu, Nando D Freitas, and Abhijeet Ghosh. Active preference learning with discrete choice data. In *Advances in neural information processing systems*, pages 409–416, 2008.

Benjamin J Brown, Charlie G Crone, and Christopher E Attinger. Amputation in the diabetic to maximize function. In *Seminars in Vascular Surgery*, volume 25, pages 115–121. Elsevier, 2012.

Frank L Buczek and PETER R Cavanagh. Stance phase knee and ankle kinematics and kinetics during level and downhill running. *Med Sci Sports Exerc*, 22(5):669–677, 1990.

Joshua M Caputo and Steven H Collins. An experimental robotic testbed for accelerated development of ankle prostheses. In *Robotics and automation (ICRA), 2013 IEEE international conference on*, pages 2645–2650. IEEE, 2013.

Joshua M Caputo, Peter G Adamczyk, and Steven H Collins. Informing ankle-foot prosthesis prescription through haptic emulation of candidate devices. In *2015 IEEE International Conference on Robotics and Automation (ICRA)*, pages 6445–6450. IEEE, 2015.

Wei Chu and Zoubin Ghahramani. Preference learning with gaussian processes. In *Proceedings of the 22nd international conference on Machine learning*, pages 137–144. ACM, 2005.

Ruta Desai and Hartmut Geyer. Robust swing leg placement under large disturbances. In *Robotics and Biomimetics (ROBIO), 2012 IEEE International Conference on*, pages 265–270. IEEE, 2012.

Neil Dhir, Houman Dallali, Evandro Maicon Ficanha, Guilherme Aramizo Ribeiro, and Mo Rastgaar. Locomotion envelopes for adaptive control of powered ankle prostheses. In *2018 IEEE International Conference on Robotics and Automation (ICRA)*, pages 1488–1495. IEEE, 2018.

Edsger W Dijkstra. A note on two problems in connexion with graphs. *Numerische mathematik*, 1(1):269–271, 1959.

Lin Du, Fan Zhang, Ming Liu, and He Huang. Toward design of an environment-aware adaptive locomotion-mode-recognition system. *IEEE Transactions on Biomedical Engineering*, 59(10):2716–2725, 2012.

Ran Duan, Shuangyue Yu, Guang Yue, Richard Foulds, Chen Feng, Yingli Tian, and Hao Su. Real-time robust 3d plane extraction for wearable robot perception and control. In *2018 Design of Medical Devices Conference*, pages Voo1To6A003–Voo1To6A003. American Society of Mechanical Engineers, 2018.

Michael F Eilenberg, Hartmut Geyer, and Hugh Herr. Control of a powered ankle–foot prosthesis based on a neuromuscular model. *Neural Systems and Rehabilitation Engineering, IEEE Transactions on*, 18(2):164–173, 2010.

Janice J Eng, David A Winter, and Aftab E Patla. Strategies for recovery from a trip in early and late swing during human walking. *Experimental Brain Research*, 102(2):339–349, 1994.

Martin A Fischler and Robert C Bolles. Random sample consensus: a paradigm for model fitting with applications to image analysis and automated cartography. *Communications of the ACM*, 24(6):381–395, 1981.

Aurélien Garivier and Eric Moulines. On upper-confidence bound policies for non-stationary bandit problems. *arXiv preprint arXiv:0805.3415*, 2008.

- Christiane Gauthier-Gagnon, Marie-Claude Grisé, and Diane Potvin. Enabling factors related to prosthetic use by people with transtibial and transfemoral amputation. *Archives of physical medicine and rehabilitation*, 80(6):706–713, 1999.
- Hartmut Geyer and Hugh Herr. A muscle-reflex model that encodes principles of legged mechanics produces human walking dynamics and muscle activities. *IEEE Transactions on neural systems and rehabilitation engineering*, 18(3):263–273, 2010.
- Hartmut Geyer, Andre Seyfarth, and Reinhard Blickhan. Positive force feedback in bouncing gaits? *Proceedings of the Royal Society of London B: Biological Sciences*, 270(1529):2173–2183, 2003.
- Jean Dickinson Gibbons and Subhabrata Chakraborti. Nonparametric statistical inference. In *International encyclopedia of statistical science*, pages 977–979. Springer, 2011.
- Claire C Gordon, Thomas Churchill, Charles E Clauser, Bruce Bradtmiller, and John T McConville. Anthropometric survey of us army personnel: methods and summary statistics 1988. Technical report, Anthropology Research Project Inc Yellow Springs OH, 1989.
- Mark D Grabiner, Timothy J Koh, Thomas M Lundin, and Dennis W Jahnigen. Kinematics of recovery from a stumble. *Journal of gerontology*, 48(3):M97–M102, 1993.
- Jesse A Grimes. *ATRIAS 1.0 & 2.1: enabling agile biped locomotion with a template-driven approach to robot design*. PhD thesis, Oregon State University, 2013.
- Michael Günther and Hanns Ruder. Synthesis of two-dimensional human walking: a test of the  $\lambda$ -model. *Biological cybernetics*, 89(2):89–106, 2003.
- Nachi Gupta and Raphael Hauser. Kalman filtering with equality and inequality state constraints. *arXiv preprint arXiv:0709.2791*, 2007.
- Nikolaus Hansen. The cma evolution strategy: a comparing review. In *Towards a new evolutionary computation*, pages 75–102. Springer, 2006.
- Philipp Hennig and Christian J Schuler. Entropy search for information-efficient global optimization. *The Journal of Machine Learning Research*, 13(1):1809–1837, 2012.
- José Miguel Hernández-Lobato, Matthew W Hoffman, and Zoubin Ghahramani. Predictive entropy search for efficient global optimization of black-box functions. In *Advances in Neural Information Processing Systems*, pages 918–926, 2014.

Hugh M. Herr and Alena M. Grabowski. Bionic ankle-foot prosthesis normalizes walking gait for persons with leg amputation. *Proceedings of the Royal Society of London B: Biological Sciences*, 279(1728):457–464, 2011. ISSN 0962-8452. DOI: 10.1098/rspb.2011.1194. URL <http://rspb.royalsocietypublishing.org/content/279/1728/457>.

A Vo Hill. The heat of shortening and the dynamic constants of muscle. *Proceedings of the Royal Society of London B: Biological Sciences*, 126(843):136–195, 1938.

Neil Houlsby, Ferenc Huszar, Zoubin Ghahramani, and Jose M Hernández-lobato. Collaborative gaussian processes for preference learning. In *Advances in Neural Information Processing Systems*, pages 2096–2104, 2012.

He Huang, Dustin L Crouch, Ming Liu, Gregory S Sawicki, and Ding Wang. A cyber expert system for auto-tuning powered prosthesis impedance control parameters. *Annals of Biomedical Engineering*, 44(5):1613–1624, 2016.

CL Hubley and RP Wells. A work-energy approach to determine individual joint contributions to vertical jump performance. *European Journal of Applied Physiology and Occupational Physiology*, 50(2):247–254, 1983.

Amanda M Huff, Brian E Lawson, and Michael Goldfarb. A running controller for a powered transfemoral prosthesis. In *2012 Annual International Conference of the IEEE Engineering in Medicine and Biology Society*, pages 4168–4171. IEEE, 2012.

Sonja MHJ Jaegers, J Hans Arendzen, and Henry J de Jongh. Prosthetic gait of unilateral transfemoral amputees: a kinematic study. *Archives of physical medicine and rehabilitation*, 76(8):736–743, 1995.

Ashesh Jain, Brian Wojcik, Thorsten Joachims, and Ashutosh Saxena. Learning trajectory preferences for manipulators via iterative improvement. In *Advances in neural information processing systems*, pages 575–583, 2013.

Jennifer L Johansson, Delsey M Sherrill, Patrick O Riley, Paolo Bonato, and Hugh Herr. A clinical comparison of variable-damping and mechanically passive prosthetic knee devices. *American journal of physical medicine & rehabilitation*, 84(8):563–575, 2005.

Donald R Jones, Matthias Schonlau, and William J Welch. Efficient global optimization of expensive black-box functions. *Journal of Global optimization*, 13(4):455–492, 1998.

- Shuuji Kajita, Fumio Kanehiro, Kenji Kaneko, Kazuhito Yokoi, and Hirohisa Hirukawa. The 3d linear inverted pendulum mode: A simple modeling for a biped walking pattern generation. In *Intelligent Robots and Systems, 2001. Proceedings. 2001 IEEE/RSJ International Conference on*, volume 1, pages 239–246. IEEE, 2001.
- Jonathan Ko and Dieter Fox. Gp-bayesfilters: Bayesian filtering using gaussian process prediction and observation models. *Autonomous Robots*, 27(1):75–90, 2009.
- Nili Eliana Krausz, Tommaso Lenzi, and Levi J Hargrove. Depth sensing for improved control of lower limb prostheses. *IEEE Transactions on Biomedical Engineering*, 62(11):2576–2587, 2015.
- J Kulkarni, S Wright, C Toole, J Morris, and R Hiron. Falls in patients with lower limb amputations: prevalence and contributing factors. *Physiotherapy*, 2(82):130–136, 1996.
- Brian E Lawson, H Atakan Varol, Frank Sup, and Michael Goldfarb. Stumble detection and classification for an intelligent transfemoral prosthesis. In *Engineering in medicine and biology society (EMBC), 2010 annual international conference of the IEEE*, pages 511–514. IEEE, 2010.
- Brian E Lawson, Jason Mitchell, Don Truex, Amanda Shultz, Elissa Ledoux, and Michael Goldfarb. A robotic leg prosthesis: Design, control, and implementation. *IEEE Robotics & Automation Magazine*, 21(4):70–81, 2014.
- Brian Edward Lawson, Huseyin Atakan Varol, Amanda Huff, Erdem Erdemir, and Michael Goldfarb. Control of stair ascent and descent with a powered transfemoral prosthesis. *IEEE Transactions on Neural Systems and Rehabilitation Engineering*, 21(3):466–473, 2013.
- Hyunglae Lee, Elliott J Rouse, and Hermano Igo Krebs. Summary of human ankle mechanical impedance during walking. *IEEE journal of translational engineering in health and medicine*, 4:1–7, 2016.
- Tommaso Lenzi, Levi Hargrove, and Jonathon Sensinger. Speed-adaptation mechanism: Robotic prostheses can actively regulate joint torque. *IEEE Robotics & Automation Magazine*, 21(4):94–107, 2014.
- Ming Liu, Ding Wang, and He Helen Huang. Development of an environment-aware locomotion mode recognition system for powered lower limb prostheses. *IEEE Transactions on Neural Systems and Rehabilitation Engineering*, 24(4):434–443, 2016.
- Jared Markowitz, Pavitra Krishnaswamy, Michael F Eilenberg, Ken Endo, Chris Barnhart, and Hugh Herr. Speed adaptation in a

powered transtibial prosthesis controlled with a neuromuscular model. *Philosophical Transactions of the Royal Society of London B: Biological Sciences*, 366(1570):1621–1631, 2011.

Ernesto C Martinez-Villalpando, Luke Mooney, Grant Elliott, and Hugh Herr. Antagonistic active knee prosthesis. a metabolic cost of walking comparison with a variable-damping prosthetic knee. In *2011 Annual International Conference of the IEEE Engineering in Medicine and Biology Society*, pages 8519–8522. IEEE, 2011.

Yerzhan Massalin, Madina Abdurakhmanova, and Huseyin Atakan Varol. User-independent intent recognition for lower-limb prostheses using depth sensing. *IEEE Transactions on Biomedical Engineering*, 2017.

Michael D McKay, Richard J Beckman, and William J Conover. A comparison of three methods for selecting values of input variables in the analysis of output from a computer code. *Technometrics*, 42(1): 55–61, 2000.

R McNeill Alexander. Energetics and optimization of human walking and running: the 2000 raymond pearl memorial lecture. *American journal of human biology*, 14(5):641–648, 2002.

William C Miller, Mark Speechley, and Barry Deathe. The prevalence and risk factors of falling and fear of falling among lower extremity amputees. *Archives of physical medicine and rehabilitation*, 82(8): 1031–1037, 2001.

Amir A Mohagheghi, Renato Moraes, and Aftab E Patla. The effects of distant and on-line visual information on the control of approach phase and step over an obstacle during locomotion. *Experimental Brain Research*, 155(4):459–468, 2004.

Jason K Moore, Sandra K Hnat, and Antonie J van den Bogert. An elaborate data set on human gait and the effect of mechanical perturbations. *PeerJ*, 3:e918, 2015.

Sylvie Nadeau, Bradford J McFadyen, and Francine Malouin. Frontal and sagittal plane analyses of the stair climbing task in healthy adults aged over 40 years: what are the challenges compared to level walking? *Clinical Biomechanics*, 18(10):950–959, 2003.

Tom F Novacheck. The biomechanics of running. *Gait & posture*, 7(1): 77–95, 1998.

Aftab E Patla and Stephen D Prentice. The role of active forces and intersegmental dynamics in the control of limb trajectory over

- obstacles during locomotion in humans. *Experimental Brain Research*, 106(3):499–504, 1995.
- Jacquelin Perry and Judith M Burnfield. *Gait analysis: normal and pathological function*. Slack Thorofare, NJ, 2 edition, 2010.
- Mirjam Pijnappels, Maarten F Bobbert, and Jaap H van Dieën. How early reactions in the support limb contribute to balance recovery after tripping. *Journal of biomechanics*, 38(3):627–634, 2005.
- Gill A Pratt and Matthew M Williamson. Series elastic actuators. In *Intelligent Robots and Systems 95.'Human Robot Interaction and Cooperative Robots', Proceedings. 1995 IEEE/RSJ International Conference on*, volume 1, pages 399–406. IEEE, 1995.
- Jerry Pratt, John Carff, Sergey Drakunov, and Ambarish Goswami. Capture point: A step toward humanoid push recovery. In *2006 6th IEEE-RAS international conference on humanoid robots*, pages 200–207. IEEE, 2006.
- David Quintero, Dario J Villarreal, and Robert D Gregg. Preliminary experiments with a unified controller for a powered knee-ankle prosthetic leg across walking speeds. In *Intelligent Robots and Systems (IROS), 2016 IEEE/RSJ International Conference on*, pages 5427–5433. IEEE, 2016.
- Marc H Raibert. *Legged robots that balance*. MIT press, 1986.
- Carl Edward Rasmussen. Gaussian processes in machine learning. In *Advanced lectures on machine learning*, pages 63–71. Springer, 2004.
- Nathan Ratliff, Matt Zucker, J Andrew Bagnell, and Siddhartha Srinivasa. Chomp: Gradient optimization techniques for efficient motion planning. In *Robotics and Automation, 2009. ICRA'09. IEEE International Conference on*, pages 489–494. IEEE, 2009.
- Nathan D Ratliff, J Andrew Bagnell, and Martin A Zinkevich. (online) subgradient methods for structured prediction. *Robotics Institute*, page 55, 2007.
- Siavash Rezazadeh, David Quintero, Nikhil Divekar, and Robert D Gregg. A phase variable approach to volitional control of powered knee-ankle prostheses. In *2018 IEEE/RSJ International Conference on Intelligent Robots and Systems (IROS)*, pages 2292–2298. IEEE, 2018.
- Stephen N Robinovitch, Fabio Feldman, Yijian Yang, Rebecca Schonnop, Pet Ming Leung, Thiago Sarraf, Joanie Sims-Gould, and Marie Loughin. Video capture of the circumstances of falls in elderly people residing in long-term care: an observational study. *The Lancet*, 381(9860):47–54, 2013.

Stéphane Ross, Geoffrey J Gordon, and Drew Bagnell. A reduction of imitation learning and structured prediction to no-regret online learning. In *AISTATS*, page 6, 2011.

Elliott J Rouse, Nathan C Villagray-Carski, Robert W Emerson, and Hugh M Herr. Design and testing of a bionic dancing prosthesis. *PloS one*, 10(8):e0135148, 2015.

Glauco Garcia Scandaroli, Geovany Araújo Borges, João Yoshiyuki Ishihara, Marco Henrique Terra, Adson Ferreira da Rocha, and Francisco Assis de Oliveira Nascimento. Estimation of foot orientation with respect to ground for an above knee robotic prosthesis. In *Intelligent robots and systems, 2009. IROS 2009. IEEE/RSJ international conference on*, pages 1112–1117. IEEE, 2009.

Alexander Schepelmann, Michael D Taylor, and Hartmut Geyer. Development of a testbed for robotic neuromuscular controllers. *Robotics: Science and Systems VIII*, 4, 2012.

Stephen H Scott and David A Winter. Biomechanical model of the human foot: kinematics and kinetics during the stance phase of walking. *Journal of biomechanics*, 26(9):1091–1104, 1993.

Fabrizio Sergi, Dino Accoto, Giorgio Carpino, Nevio Luigi Tagliamonte, and Eugenio Guglielmelli. Design and characterization of a compact rotary series elastic actuator for knee assistance during overground walking. In *Biomedical Robotics and Biomechatronics (BioRob), 2012 4th IEEE RAS & EMBS International Conference on*, pages 1931–1936. IEEE, 2012.

Andre Seyfarth, Hartmut Geyer, Michael Günther, and Reinhard Blickhan. A movement criterion for running. *Journal of biomechanics*, 35(5):649–655, 2002.

Camila Shirota, Ann M Simon, and Todd A Kuiken. Recovery strategy identification throughout swing phase using kinematic data from the tripped leg. In *Engineering in Medicine and Biology Society (EMBC), 2014 36th Annual International Conference of the IEEE*, pages 6199–6202. IEEE, 2014.

Camila Shirota, Ann M Simon, and Todd A Kuiken. Transfemoral amputee recovery strategies following trips to their sound and prosthesis sides throughout swing phase. *Journal of neuroengineering and rehabilitation*, 12(1):79, 2015.

Amanda H Shultz, Brian E Lawson, and Michael Goldfarb. Running with a powered knee and ankle prosthesis. *IEEE Transactions on Neural Systems and Rehabilitation Engineering*, 23(3):403–412, 2015.

- Ann M Simon, Kimberly A Ingraham, Nicholas P Fey, Suzanne B Finucane, Robert D Lipschutz, Aaron J Young, and Levi J Hargrove. Configuring a powered knee and ankle prosthesis for transfemoral amputees within five specific ambulation modes. *PloS one*, 9(6):e99387, 2014.
- Edward Snelson and Zoubin Ghahramani. Local and global sparse gaussian process approximations. In *Artificial Intelligence and Statistics*, pages 524–531, 2007.
- E Solak, R Murray Smith, WE Leithead, D Leith, and CE Rasmussen. Derivative observations in gaussian process models of dynamic systems. *Advances in Neural Information Processing Systems*, pages 1057–1064, 2003.
- Seungmoon Song and Hartmut Geyer. Generalization of a muscle-reflex control model to 3d walking. In *2013 35th Annual International Conference of the IEEE Engineering in Medicine and Biology Society (EMBC)*, pages 7463–7466. IEEE, 2013.
- Seungmoon Song and Hartmut Geyer. A neural circuitry that emphasizes spinal feedback generates diverse behaviours of human locomotion. *The Journal of physiology*, 593(16):3493–3511, 2015.
- Seungmoon Song, Ruta Desai, and Hartmut Geyer. Integration of an adaptive swing control into a neuromuscular human walking model. In *2013 35th Annual International Conference of the IEEE Engineering in Medicine and Biology Society (EMBC)*, pages 4915–4918. IEEE, 2013.
- JA Spanias, AM Simon, SB Finucane, EJ Perreault, and LJ Hargrove. Online adaptive neural control of a robotic lower limb prosthesis. *Journal of neural engineering*, 15(1):016015, 2018.
- Frank Sup, Amit Bohara, and Michael Goldfarb. Design and control of a powered knee and ankle prosthesis. In *Robotics and Automation, 2007 IEEE International Conference on*, pages 4134–4139. IEEE, 2007.
- Frank Sup, Amit Bohara, and Michael Goldfarb. Design and control of a powered transfemoral prosthesis. *The International journal of robotics research*, 27(2):263–273, 2008.
- Frank Sup, Huseyin Atakan Varol, Jason Mitchell, Thomas J Withrow, and Michael Goldfarb. Preliminary evaluations of a self-contained anthropomorphic transfemoral prosthesis. *IEEE/ASME Transactions on mechatronics*, 14(6):667–676, 2009.
- Frank Sup, Huseyin Atakan Varol, and Michael Goldfarb. Upslope walking with a powered knee and ankle prosthesis: initial results

with an amputee subject. *IEEE Transactions on Neural Systems and Rehabilitation Engineering*, 19(1):71–78, 2011.

Nitish Thatte and Hartmut Geyer. Towards local reflexive control of a powered transfemoral prosthesis for robust amputee push and trip recovery. In *2014 IEEE/RSJ International Conference on Intelligent Robots and Systems*, pages 2069–2074. IEEE, 2014.

Nitish Thatte and Hartmut Geyer. Toward balance recovery with leg prostheses using neuromuscular model control. *IEEE Transactions on Biomedical Engineering*, 63(5):904–913, 2016.

Nitish Thatte, Helei Duan, and Hartmut Geyer. A sample-efficient black-box optimizer to train policies for human-in-the-loop systems with user preferences. *IEEE Robotics and Automation Letters*, 2017.

Nitish Thatte, Helei Duan, and Hartmut Geyer. A method for online optimization of lower limb assistive devices with high dimensional parameter spaces. In *Robotics and Automation (ICRA), 2018 IEEE International Conference on*. IEEE, 2018.

Miles A Townsend. Biped gait stabilization via foot placement. *Journal of biomechanics*, 18(1):21–38, 1985.

Brian R Umberger, Karin GM Gerritsen, and Philip E Martin. A model of human muscle energy expenditure. *Computer methods in biomechanics and biomedical engineering*, 6(2):99–111, 2003.

Heike Vallery, Rainer Burgkart, Cornelia Hartmann, Jürgen Mitternacht, Robert Riener, and Martin Buss. Complementary limb motion estimation for the control of active knee prostheses. *Biomedizinische Technik/Biomedical Engineering*, 56(1):45–51, 2011.

Vassilios G Vardaxis, Paul Allard, Régis Lachance, and Morris Duhaime. Classification of able-bodied gait using 3-d muscle powers. *Human Movement Science*, 17(1):121–136, 1998.

Huseyin Atakan Varol, Frank Sup, and Michael Goldfarb. Powered sit-to-stand and assistive stand-to-sit framework for a powered transfemoral prosthesis. In *2009 IEEE International Conference on Rehabilitation Robotics*, pages 645–651. IEEE, 2009.

RL Waters, Jacqueline Perry, DANIEL Antonelli, and Helen Hislop. Energy cost of walking of amputees: the influence of level of amputation. *J Bone Joint Surg Am*, 58(1):42–46, 1976.

Yue Wen, Ming Liu, Jennie Si, and He Helen Huang. Adaptive control of powered transfemoral prostheses based on adaptive dynamic programming. In *Engineering in Medicine and Biology Society (EMBC)*,

- 2016 IEEE 38th Annual International Conference of the, pages 5071–5074. IEEE, 2016.
- Michael James Whitley. *Maximum Absolute and Relative Joint Torques during Recovery from a Simulated Trip*. PhD thesis, Virginia Polytechnic Institute and State University, 2008.
- Christopher KI Williams and Carl Edward Rasmussen. *Gaussian processes for machine learning*, volume 2. MIT Press Cambridge, MA, 2006.
- Aaron Wilson, Alan Fern, and Prasad Tadepalli. A bayesian approach for policy learning from trajectory preference queries. In *Advances in neural information processing systems*, pages 1133–1141, 2012.
- David A Winter. *Biomechanics and motor control of human movement*. John Wiley & Sons, 2009.
- Albert Wu and Hartmut Geyer. The 3-d spring–mass model reveals a time-based deadbeat control for highly robust running and steering in uncertain environments. *IEEE Transactions on Robotics*, 29(5):1114–1124, 2013.
- Huasen Wu and Xin Liu. Double thompson sampling for dueling bandits. In *Advances in Neural Information Processing Systems*, pages 649–657, 2016.
- Linfeng Xu and X Rong Li. Estimation and filtering of gaussian variables with linear inequality constraints. In *Information Fusion (FUSION), 2010 13th Conference on*, pages 1–6. IEEE, 2010.
- KangKang Yin, Kevin Loken, and Michiel Van de Panne. Simbicon: Simple biped locomotion control. In *ACM Transactions on Graphics (TOG)*, volume 26, page 105. ACM, 2007.
- Yisong Yue, Josef Broder, Robert Kleinberg, and Thorsten Joachims. The k-armed dueling bandits problem. *Journal of Computer and System Sciences*, 78(5):1538–1556, 2012.
- Fan Zhang, Susan E D’Andrea, Michael J Nunnery, Steven M Kay, and He Huang. Towards design of a stumble detection system for artificial legs. *IEEE Transactions on Neural Systems and Rehabilitation Engineering*, 19(5):567–577, 2011a.
- Fan Zhang, Zheng Fang, Ming Liu, and He Huang. Preliminary design of a terrain recognition system. In *Engineering in medicine and biology society, EMBC, 2011 annual international conference of the IEEE*, pages 5452–5455. IEEE, 2011b.

Juanjuan Zhang, Pieter Fiers, Kirby A Witte, Rachel W Jackson, Katherine L Poggensee, Christopher G Atkeson, and Steven H Collins. Human-in-the-loop optimization of exoskeleton assistance during walking. *Science*, 356(6344):1280–1284, 2017.

Kathryn Ziegler-Graham, Ellen J MacKenzie, Patti L Ephraim, Thomas G Travison, and Ron Brookmeyer. Estimating the prevalence of limb loss in the united states: 2005 to 2050. *Archives of physical medicine and rehabilitation*, 89(3):422–429, 2008.